

An ALMA Survey of Chemistry in Disks around M4-M5 Stars

JAMILA PEGUES,¹ KARIN I. ÖBERG,¹ JENNIFER B. BERGNER,^{2,1,*} JANE HUANG,^{3,1,*} ILARIA PASCUCCI,^{4,5} RICHARD TEAGUE,¹ SEAN M. ANDREWS,¹ EDWIN A. BERGIN,⁶ L. ILSEDORE CLEEVE,⁷ VIVIANA V. GUZMÁN,⁸ FENG LONG,¹ CHUNHUA QI,¹ AND DAVID J. WILNER¹

¹ Center for Astrophysics | Harvard & Smithsonian, Cambridge, MA 02138, USA

² Department of Geophysical Sciences, University of Chicago, Chicago, IL 60637, USA

³ Department of Astronomy, University of Michigan, 323 West Hall, 1085 S. University Avenue, Ann Arbor, MI 48109, USA

⁴ Lunar and Planetary Laboratory, The University of Arizona, Tucson, AZ 85721, USA

⁵ Earths in Other Solar Systems Team, NASA Nexus for Exoplanet System Science

⁶ Department of Astronomy, University of Michigan, 1085 S. University Ave, Ann Arbor, MI 48109

⁷ Astronomy Department, University of Virginia, Charlottesville, VA 22904, USA

⁸ Instituto de Astrofísica, Pontificia Universidad Católica de Chile, Av. Vicuña Mackenna 4860, 7820436 Macul, Santiago, Chile

ABSTRACT

M-stars are the most common hosts of planetary systems in the Galaxy. Protoplanetary disks around M-stars thus offer a prime opportunity to study the chemistry of planet-forming environments. We present an ALMA survey of molecular line emission toward a sample of five protoplanetary disks around M4-M5 stars (FP Tau, J0432+1827, J1100-7619, J1545-3417, and Sz 69). These observations can resolve chemical structures down to tens of AU. Molecular lines of ¹²CO, ¹³CO, C¹⁸O, C₂H, and HCN are detected toward all five disks. Lines of H₂CO and DCN are detected toward 2/5 and 1/5 disks, respectively. For disks with resolved C¹⁸O, C₂H, HCN, and H₂CO emission, we observe substructures similar to those previously found in disks around solar-type stars (e.g., rings, holes, and plateaus). C₂H and HCN excitation conditions estimated interior to the pebble disk edge for the bright disk J1100-7619 are consistent with previous measurements around solar-type stars. The correlation previously found between C₂H and HCN fluxes for solar-type disks extends to our M4-M5 disk sample, but the typical C₂H/HCN ratio is higher for the M4-M5 disk sample. This latter finding is reminiscent of the hydrocarbon enhancements found by previous observational infrared surveys in the innermost (<10AU) regions of M-star disks, which is intriguing since our disk-averaged fluxes are heavily influenced by flux levels in the outermost disk, exterior to the pebble disk edge. Overall, most of the observable chemistry at 10-100AU appears similar for solar-type and M4-M5 disks, but hydrocarbons may be more abundant around the cooler stars.

Keywords: astrochemistry, protoplanetary disks, ISM: molecules, radio lines: ISM

1. INTRODUCTION

The exoplanetary family within the local Galaxy is dominated by M-stars. M-stars are not only the most common stars in the local Galaxy, but are also the most common hosts of planetary systems (e.g., Henry et al. 2006; Dressing & Charbonneau 2015; Mulders et al. 2015; Henry et al. 2016). The study of protoplanetary disk chemistry is crucial for modeling and predicting the chemistry of comets, planetesimals, and planets around these common cool stars.

To date, disk chemistry around low-mass M-stars (stellar masses <0.5M_⊙, spectral types typically from ~M4-M9) has barely been explored beyond the inner ~10 AU. The majority of observational chemistry surveys of low-mass M-star

disks have been of infrared molecular lines, which probe disk scales of <10 AU (e.g., Pascucci et al. 2009; Pontoppidan et al. 2010; Harvey et al. 2012; Pascucci et al. 2013; Bulger et al. 2014; Hendler et al. 2017). At millimeter wavelengths, CO and dust observations exist toward samples of low-mass M-star disks (e.g., Ricci et al. 2014; Cieza et al. 2015; Pascucci et al. 2016; van der Plas et al. 2016; Ansdell et al. 2017; Long et al. 2017; Andrews et al. 2018). However, reported emission from other millimeter wavelength molecular lines is scarce: CN, SO, H₂CO, and CO fluxes have been observed toward one low-mass M-star disk in ρ Ophiuchi (Reboussin et al. 2015); CN fluxes have been observed toward low-mass M-star disks in Lupus (van Terwisga et al. 2019); and bright C₂H emission has been resolved toward three disks with stellar masses <0.5M_⊙ in Lupus (Miotello et al. 2019).

* NASA Hubble Fellowship Program Sagan Fellow

The existing molecular line observations provide important insights into the chemistry of low-mass M-star disks. Detection rates for infrared lines of small molecular species (including H_2O , C_2H_2 , HCN , and CO_2) in the inner disk regions generally increase with decreasing spectral type (from A-stars down to M-stars; e.g., Pontoppidan et al. 2010). Disks around low-mass M-stars and brown dwarfs (spectral types $\leq \text{M6}$) also have higher infrared $\text{C}_2\text{H}_2/\text{HCN}$ flux and column density ratios and higher $\text{HNC}/\text{H}_2\text{O}$ flux ratios relative to disks around solar-type stars (Pascucci et al. 2009, 2013). These infrared studies have attributed these enhancements to higher C/O ratios in the inner disks around low-mass stars.

Theoretically, models have predicted that the differences in stellar properties between low-mass and solar-type stars affect some aspects of disk chemistry, while others appear insensitive to the details of the stellar radiation field. Models comparing disk chemistry within $\leq 10\text{AU}$ around an M-dwarf and T Tauri star have predicted that M-dwarf disks host more carbon-rich atmospheres, with relatively high abundances of small organic molecules like C_2H_2 and HCN (Walsh et al. 2015). A study comparing a grid of thermochemical brown dwarf disk models and a T Tauri disk model predicted that brown dwarf disks and T Tauri disks host similar physical and chemical processes overall, but found model evidence in support of the enhanced hydrocarbon content suggested by previous infrared surveys (Greenwood et al. 2017). While these theoretical efforts provide some guidance, we emphasize the lack of predictions for molecular column densities and abundances beyond 10AU in disks around low-mass M-stars.

In this study, we present an Atacama Large Millimeter/submillimeter Array (ALMA) exploratory survey of molecules toward a sample of five disks around M4-M5 stars, and we draw preliminary conclusions on chemistry across the disks. In Section 2, we describe the disks and molecular lines in the survey sample, the ALMA observations, and the data reduction process. In Section 3, we discuss the tools used to analyze the image products, to characterize the emission, and to measure molecular column densities, excitation temperatures, and optical depths. In Section 4, we present the detections, emission morphologies, relative fluxes and flux correlations, and estimates of molecular column densities, excitation temperatures, and optical depths. In Section 5, we discuss the results, and we compare M4-M5 disk chemistry from our sample with solar-type counterparts from previous molecular surveys (Huang et al. 2017; Bergner et al. 2019, 2020; Pegues et al. 2020). In Section 6, we summarize the key findings of our survey.

2. OBSERVATIONS

2.1. Disk Sample

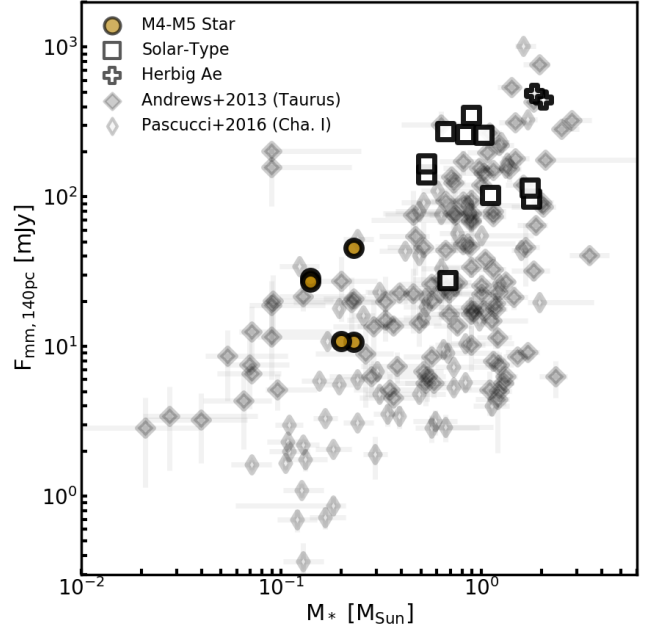


Figure 1. The dust continuum fluxes for the M4-M5 disk sample as a function of stellar mass, compared to disks compiled from the literature. The dark gold circles are 1.1mm continuum fluxes for M4-M5 disk detections from this work. The white points are ALMA-observed 1.1mm or 1.3mm continuum flux detections (whichever is available) for solar-type disks (marked with squares) and Herbig Ae disks (marked with crosses). These disks were compiled from Huang et al. (2017), Bergner et al. (2019), Bergner et al. (2020), and Pegues et al. (2020). This is the same compilation used later in Section 4.3. The thick and thin diamonds are disks detected in 0.89mm continuum fluxes from Andrews et al. (2013) and Pascucci et al. (2016), which surveyed the Taurus and Chamaeleon I star-forming regions, respectively. All fluxes were scaled from their original wavelengths to 1.1mm using $c = \lambda\nu$ and $F_\nu \propto \nu^\alpha$, where c is the speed of light, λ is the wavelength, ν is the frequency, and F_ν is the dust continuum flux. We assume empirically that $\alpha = 2.2$ (review by Andrews 2020). All fluxes have also been scaled to 140pc.

Table 1 presents the stellar characteristics of the survey sample, which consists of five disks around M4-M5 stars. The disks were chosen from multiple star-forming regions, avoiding bias toward any one molecular cloud. Two of the disks are from the Taurus region, two from the Lupus region, and one from the Chamaeleon I region. All disks are within 128-192pc (Gaia Collaboration et al. 2016, 2018). Millimeter dust disk sizes are $\sim 30\text{-}63\text{AU}$ (where the size denotes the radius that contains $\sim 90\%$ of the emission, similar to the methods of Ansdell et al. 2018). We refer to the millimeter dust disk as the “pebble disk” throughout the remainder of the paper. The host stars of the disks are $\sim 1\text{-}3\text{Myr}$ in age and range in spectral type, stellar luminosity, estimated stellar mass, and stellar effective temperature from M4-M5.5, $\sim 0.05\text{-}0.32L_\odot$, $\sim 0.14\text{-}0.23M_\odot$, and $\sim 3000\text{-}3300\text{K}$, respectively. All stellar characteristics were derived in the litera-

Table 1. Stellar and Disk Characteristics of the Sample.

| Disk | Spectral Type | R.A. ^[0] (J2000) | Decl. ^[0] (J2000) | Region | Distance ^[0] (pc) | t_* (Myr) | L_* (L_\odot) | M_* (M_\odot) | T_{eff} (K) |
|--------------------|----------------------|--------------------------------|---------------------------------|--------------|---------------------------------|----------------------------|------------------------|------------------------|-------------------------|
| (1) | (2) | (3) | (4) | (5) | (6) | (7) | (8) | (9) | (10) |
| FP Tau | M4 ^[1] | 04:14:47.31 | 26:46:26.06 | Taurus | 128.5 (140 ^[2]) | 1.1 ^[2] | 0.32 ^[2] | 0.23 ^[2] | 3270 ^[2] |
| J04322210+1827426* | M4.75 ^[3] | 04:32:22.12 | 18:27:42.36 | Taurus | 141.9 (140 ^[3]) | ~ 1 ^[3] | 0.11 ^[3] | 0.14 ^[3] | 3027 ^[3] |
| J11004022-7619280* | M4 ^[4] | 11:00:40.14 | -76:19:28.00 | Chamaeleon I | 191.5 (160 ^[4]) | ~ 2 -3 ^[4] | 0.10 ^[4] | 0.23 ^[4] | 3270 ^[4] |
| J15450887-3417333* | M5.5 ^[5] | 15:45:08.86 | -34:17:33.80 | Lupus | 155.0 (150 ^[5]) | ~ 3 ^[5] | 0.058 ^[5] | 0.14 ^[5] | 3060 ^[5] |
| Sz 69 | M4.5 ^[5] | 15:45:17.39 | -34:18:28.64 | Lupus | 154.5 (150 ^[5]) | ~ 3 ^[5] | 0.088 ^[5] | 0.20 ^[5] | 3197 ^[5] |

NOTE—Right ascension (R.A.) and declination (decl.) coordinates and distances are from *Gaia* (e.g., [Gaia Collaboration et al. 2016, 2018](#)). The stellar ages (t_*), stellar luminosities (L_*), stellar masses (M_*), and stellar effective temperatures (T_{eff}) were taken from the literature, where they were derived from continuum photometry, spectral energy distribution (SED) fits, scaling relations, and/or stellar evolutionary models. The distances in parentheses are the distances assumed in the literature for these disks. We use the values in parentheses throughout this paper to be consistent with the derived stellar characteristics. *: J04322210+1827426, J11004022-7619280, and J15450887-3417333 are referred to as J0432+1827, J1100-7619, and J1545-3417 in subsequent figures, tables, and text. *References:* [0] [Gaia Collaboration et al. \(2016, 2018\)](#), [1] [Luhman et al. \(2010\)](#), [2] [Andrews et al. \(2013\)](#), [3] [Ward-Duong et al. \(2018\)](#), [4] [Manara et al. \(2017\)](#), [5] [Alcalá et al. \(2017\)](#).

Table 2. Molecular Lines in the Sample.

| Molecule | Transition | Frequency (GHz) | E_u (K) | $S\mu^2$ (Debye ²) | $S\mu^2/S_{\text{m}}\mu^2$ | R_i |
|-------------------|---------------------------------|--------------------|--------------|-----------------------------------|----------------------------|---------|
| (1) | (2) | (3) | (4) | (5) | (6) | (7) |
| ¹² CO | J=2-1 | 230.53800 | 16.596 | 0.024227 | — | — |
| ¹³ CO | J=2-1 | 220.39868 | 15.866 | 0.048753 | — | — |
| C ¹⁸ O | J=2-1 | 219.56035 | 15.806 | 0.024401 | — | — |
| C ₂ H | N=3-2, J=7/2-5/2, F=4-3 | 262.00426 | 25.149 | 2.2809 | 1.0 | 0.572 |
| | N=3-2, J=7/2-5/2, F=3-2 | 262.00648 | 25.148 | 1.7065 | 0.74817 | 0.428 |
| | N=3-2, J=5/2-3/2, F=3-2 | 262.06499 | 25.159 | 1.6290 | 0.71419 | 0.605 |
| | N=3-2, J=5/2-3/2, F=2-1 | 262.06747 | 25.160 | 1.0644 | 0.46666 | 0.395 |
| DCN | J=3-2 | 217.23854 | 20.852 | 80.507 | — | — |
| HCN | J=3-2, F=4-3 | 265.88650 | 25.521 | 34.369 | 1.0 | 0.429 |
| | J=3-2, F=3-3 | 265.88489 | 25.521 | 2.9702 | 0.086418 | 0.0370 |
| | J=3-2, F=3-2 | 265.88643 | 25.521 | 23.761 | 0.69135 | 0.296 |
| | J=3-2, F=2-3 | 265.88698 | 25.521 | 0.084870 | 0.0024693 | 0.00111 |
| | J=3-2, F=2-2 | 265.88852 | 25.521 | 2.9708 | 0.086436 | 0.0370 |
| | J=3-2, F=2-1 | 265.88619 | 25.521 | 16.039 | 0.46666 | 0.200 |
| H ₂ CO | ₃₀₃ - ₂₀₂ | 218.22219 | 20.956 | 16.308 | — | — |

NOTE—All frequencies, upper energy levels (E_u), and line intensities ($S\mu^2$) were obtained directly from the Cologne Database for Molecular Spectroscopy (CDMS; [Endres et al. 2016](#)), with the exception of the HCN lines, for which these values were obtained from CDMS via Splatalogue ([Remijan et al. 2016](#)). The line intensities of each hyperfine transition relative to the main hyperfine transition ($S\mu^2/S_{\text{m}}\mu^2$) are given in column 6. The line intensities of each hyperfine transition relative to all same-level J transitions, denoted as R_i , are given in column 7.

Table 3. ALMA Project Code 2017.1.01107.S.

| Observed Disks | Target Freq. (GHz) | Date | Total Time per Source (min) | # of Ant.* | Baseline Range (m) | Ang. Res.* (") | Max Ang. Scale* (") | Bandpass Calibrator | Flux Calibrator | Phase Calibrator |
|--------------------|--------------------|------------|-----------------------------|------------|--------------------|----------------|---------------------|---------------------|-----------------|------------------|
| (1) | (2) | (3) | (4) | (5) | (6) | (7) | (8) | (9) | (10) | (11) |
| FP Tau, J0432+1827 | 230.5 | 12/31/2017 | 25.2, 22.7 | 46 | 15-2517 | 0.13 | 2.49 | J0510+1800 | J0510+1800 | J0426+2327 |
| | | 1/22/2018 | 25.2, 22.7 | 44 | 15-1398 | 0.25 | 3.74 | J0510+1800 | J0510+1800 | J0426+2327 |
| | | 1/23/2018 | 25.2, 22.7 | 43 | 15-1398 | 0.25 | 3.68 | J0510+1800 | J0510+1800 | J0426+2327 |
| | 262.1 | 9/14/2018 | 18.7, 16.6 | 44 | 15-1261 | 0.24 | 3.74 | J0510+1800 | J0510+1800 | J0426+2327 |
| | | 9/15/2018 | 18.7, 16.6 | 44 | 15-1261 | 0.24 | 3.46 | J0510+1800 | J0510+1800 | J0426+2327 |
| J1100-7619 | 230.5 | 1/24/2018 | 36.3 | 44 | 15-1398 | 0.25 | 3.79 | J1427-4206 | J1427-4206 | J1058-8003 |
| | | 9/15/2018 | 36.3 | 42 | 15-1261 | 0.27 | 3.94 | J1037-2934 | J1037-2934 | J1058-8003 |
| | | 9/16/2018 | 36.3 | 43 | 15-1261 | 0.26 | 3.77 | J0635-7516 | J0635-7516 | J1058-8003 |
| | | 9/18/2018 | 36.3 | 44 | 15-1398 | 0.25 | 3.56 | J0635-7516 | J0635-7516 | J1058-8003 |
| | 262.1 | 12/26/2017 | 39.8 | 46 | 15-2517 | 0.12 | 2.35 | J1427-4206 | J1427-4206 | J1058-8003 |
| J1545-3417, Sz 69 | 230.5 | 1/17/2018 | 19.7, 19.7 | 44 | 15-1398 | 0.25 | 3.77 | J1517-2422 | J1517-2422 | J1610-3958 |
| | | 1/18/2018 | 19.7, 19.7 | 45 | 15-1398 | 0.25 | 3.77 | J1517-2422 | J1517-2422 | J1610-3958 |
| | | 1/18/2018 | 19.7, 19.7 | 45 | 15-1398 | 0.25 | 3.77 | J1517-2422 | J1517-2422 | J1610-3958 |
| | 262.1 | 1/22/2018 | 17.1, 17.1 | 45 | 15-1398 | 0.22 | 3.29 | J1517-2422 | J1517-2422 | J1534-3526 |
| | | 3/10/2018 | 17.1, 17.1 | 41 | 15-1241 | 0.29 | 4.23 | J1517-2422 | J1517-2422 | J1610-3958 |

NOTE—Columns 5, 7, and 8 are abbreviations of *Number of Antennas*, *Angular Resolution*, and *Maximum Angular Scale*, respectively.

Table 4. Dust Continuum Emission.

| Disk | λ (mm) | 90% Em. Radius (AU) | Total Em. (mJy) | Peak Em. (mJy beam ⁻¹) | rms (mJy beam ⁻¹) | Beam Size (P.A.) |
|------------|----------------|---------------------|-----------------|------------------------------------|-------------------------------|-------------------------|
| (1) | (2) | (3) | (4) | (5) | (6) | (7) |
| FP Tau | 1.1 | 44 | 11 ± 0.019 | 8.7 | 0.04 | 0.40" x 0.26" (-173.8°) |
| | 1.3 | 36 | 8.4 ± 0.015 | 6.4 | 0.03 | 0.29" x 0.23" (-8.4°) |
| J0432+1827 | 1.1 | 51 | 29 ± 0.077 | 12 | 0.09 | 0.35" x 0.25" (14.6°) |
| | 1.3 | 42 | 25 ± 0.051 | 8.6 | 0.05 | 0.24" x 0.20" (-16.1°) |
| J1100-7619 | 1.1 | 46 | 35 ± 0.077 | 5.8 | 0.04 | 0.19" x 0.14" (-11.4°) |
| | 1.3 | 63 | 25 ± 0.056 | 8.6 | 0.07 | 0.39" x 0.25" (-3.2°) |
| J1545-3417 | 1.1 | 42 | 24 ± 0.28 | 18 | 0.04 | 0.29" x 0.24" (90.0°) |
| | 1.3 | 41 | 20 ± 0.16 | 15 | 0.04 | 0.27" x 0.24" (76.4°) |
| Sz 69 | 1.1 | 30 | 9.4 ± 0.023 | 9.0 | 0.04 | 0.29" x 0.24" (-89.8°) |
| | 1.3 | 30 | 8.0 ± 0.015 | 7.2 | 0.03 | 0.27" x 0.24" (77.7°) |

NOTE—*Em.* in columns 3, 4, and 5 is an abbreviation of *Emission*. The pebble disk size (column 3) is represented as the radius containing 90% of the dust continuum emission. Total and peak emission for the 1.1mm (262GHz) and 1.3mm (231GHz) dust continuum were measured within the bounds of the ¹²CO and HCN Keplerian masks, respectively (Appendix A). Note the difference in unit between the two quantities. The error in the total emission was estimated across 1000 Keplerian-masked random samples extracted away from the source center. The rms was also estimated across 1000 random samples, extracted in 2" × 2" regions away from the source center. Uncertainties do not include ~15% systematic flux calibration uncertainties.

ture from continuum photometry, spectral energy distribution (SED) fits, scaling relations, and/or stellar evolutionary models¹ (Luhman et al. 2010; Andrews et al. 2013; Ward-Duong et al. 2018; Manara et al. 2017; Alcalá et al. 2017).

Figure 1 compares the dust continuum fluxes of our M4-M5 disk sample to dust continuum fluxes of solar-type and Herbig Ae disks (compiled from the chemistry surveys of Huang et al. 2017; Bergner et al. 2019, 2020; Pegues et al. 2020, discussed further in Section 4.3). Figure 1 also compares our sample to the dust continuum flux detections from Andrews et al. (2013) and from Pascucci et al. (2016), which were extracted from the Taurus and Chamaeleon I star-forming regions, respectively. The M4-M5 disks in our sample allow us to probe a lower stellar mass regime than the previous chemistry surveys dominated by solar-type disks. The majority of our M4-M5 disks fall within the brighter regime of the dust continuum flux vs. stellar mass relationship. Our sample thus provides an initial rather than representative look into resolved disk chemistry around M4-M5 stars and in the low-mass M-star regime.

We note that the five disks in the M4-M5 disk sample were selected specifically for their bright ^{12}CO ($J=3-2$) and ^{13}CO ($J=3-2$) detections in existing ALMA disk surveys (e.g., Ansdell et al. 2016; Long et al. 2017, van der Plas et al. in prep.). These selection criteria are similar to those used by early exploratory chemistry surveys of solar-type and Herbig Ae disks (e.g., the DISCS survey, Öberg et al. 2010, 2011b), and so our M4-M5 disk sample can reasonably be compared to disks around more massive stars from these previous surveys. The solar-type and Herbig Ae disks form the core of our literature sample, which is overplotted in Figure 1. We compare our M4-M5 disk sample to this literature sample in Section 4.3.

2.2. Molecular Line Sample

We survey the overall chemistry of these disks by targeting 1.1mm and 1.3mm lines of CO isotopologues and precursor organic molecules. Our primary target molecular lines are ^{12}CO ($J=2-1$), ^{13}CO ($J=2-1$), C^{18}O ($J=2-1$), C_2H ($N=3-2$, $J=7/2-5/2$), DCN ($J=3-2$), HCN ($J=3-2$), and H_2CO $3_{03}-2_{02}^2$. Together, these lines provide constraints on the C/N/O chemistry and organic inventories in the emitting layers of the disks (e.g., Bergin et al. 2016; Cleeves et al. 2018; Miotello et al. 2019). These lines have also been previously observed toward disks around solar-type stars, allowing direct comparison of the disk chemistry between these two

types of stars. We additionally use observations of the hyper-fine structure of the C_2H and HCN lines to estimate C_2H and HCN column densities, excitation temperatures, and optical depths. The molecular characteristics of the target lines are summarized in Table 2.

2.3. Data and Data Reduction

Table 3 presents the observational characteristics of the sample. All five disks were observed with ALMA during Project 2017.1.01107.S from December 2017 through September 2018. Each individual observation (i.e., each execution) used a total of 41-46 antennas, providing a minimum baseline of 15m and maximum baselines from 1241-2517m. Individual on-source observation times spanned 16-40min. The angular resolution and maximum angular scales ranged from 0.12-0.29" and 2.35-4.23", respectively.

Initial calibration (including flux, phase, and bandpass calibration) was performed by ALMA/NAASC using standard procedures. We then used the Common Astronomy Software Applications package (CASA) version 4.7.2 to self-calibrate each observation and image each molecular line. We self-calibrated each observation using the line-free continuum combined from all spectral windows. We uniformly used Briggs weighting and a robust value of 0.5. We performed two rounds of phase calibration and one round of amplitude calibration per observation when able. Solution intervals for the disks J1545-3417 and Sz 69 ranged from 10-100 seconds for each observation. These intervals were chosen as the minimum values in this range that still maximized the number of solutions with signal-to-noise ≥ 2 . Due to low continuum fluxes, we used solution intervals from 70-210 seconds for the five observations toward FP Tau. We were unable to self-calibrate on the continuum for J0432+1827 and J1100-7619.

We used CASA's `uvcontsub` and `clean` functions to (1) subtract the continuum from each spectral window and (2) image each molecular line. We created `cleaning` masks by hand to cover the molecular emission and little else in each channel. For fainter lines, we recycled `cleaning` masks from brighter lines and `cleaned` down to 3σ rather than the deeper 2σ , where σ is the average rms across non-emission channels, to avoid creating image artifacts. In order to balance sensitivity and resolution, we imaged each line using Briggs weighting and a robust value of 0.5. The resulting synthesized beams range from 0.18" to 0.47" in size. We imaged the dust continuum and molecular line emission toward the disk observed with the highest resolution (J1100-7619) with a pixel size of 0.02", while we imaged the emission toward the other four disks in the sample (FP Tau, J0432+1827, J1545-3417, and Sz 69) with a pixel size of 0.04".

We imaged the following line+disk combinations at a channel resolution of 0.2km/s: all line emission toward the

¹ See Pegues et al. (2021) for new dynamical measurements of the stellar masses for FP Tau, J0432+1827, and J1100-7619.

² These lines are abbreviated as ^{12}CO 2-1, ^{13}CO 2-1, C^{18}O 2-1, C_2H 3-2, DCN 3-2, HCN 3-2, and H_2CO 3-2, respectively, in subsequent figures, tables, and text.

bright disk J1100-7619; the ^{12}CO 2–1, ^{13}CO 2–1, and HCN 3–2 lines toward FP Tau and J0432+1827; and the ^{12}CO 2–1 and ^{13}CO 2–1 lines toward J1545-3417 and Sz 69. All other line+disk combinations were imaged at a channel resolution of 0.4km/s to increase the signal-to-noise ratio. We analyze velocity channels for each disk+line only within a specific velocity range. We select these ranges based on visual inspection of the Keplerian-masked spectra (Section 3.1) to encompass the visible emission. These ranges also include additional “buffer” channels to ensure that we have incorporated all emission. Note that the velocity ranges for the C_2H 3–2 and HCN 3–2 lines are extended to include all hyperfine components.

3. ANALYSIS

3.1. Image Analysis

We estimated the disk centers using two-dimensional Gaussian fits to the dust continuum emission. We used Keplerian masks (e.g., Rosenfeld et al. 2013; Yen et al. 2016; Salinas et al. 2017) to extract emission for each disk (software: jpegues 2019) across all emission channels for each molecular line. Keplerian masks decrease the amount of noise that is incorporated into the integrated emission. Mask parameters used for this survey are given in Appendix A. We used the Keplerian-masked channels to then generate spectra, velocity-integrated emission maps, radial profiles, and integrated fluxes.

We took the average rms across 1000 $2'' \times 2''$ random samples of non-emission channels to be the channel rms. We estimated the noise for the integrated fluxes via bootstrapping over 1000 Keplerian-masked random samples of non-emission channels. For the velocity-integrated emission maps, we used the median of 1000 random rms maps (σ_{map} ; Bergner et al. 2018) as a representation of the noise. For the radial profiles, we adapted the approach of Bergner et al. (2018) and estimated the noise per ring as ($\sigma_{\text{map}}/\sqrt{N}$). N is the number of independent measurements in the ring, assumed to be $N=(\# \text{ pixels within each ring's width})/(\# \text{ pixels in the beam area})$. Once the count per ring is less than the circumference of the beam, N is fixed to be the value of N using the circumference.

3.2. Pixel-by-Pixel Hyperfine Fits

The C_2H ($N=3-2$, $J=7/2-5/2$), C_2H ($N=3-2$, $J=5/2-3/2$), and HCN 3–2 lines exhibit hyperfine structure, and so the emission spectra can be decomposed into individual hyperfine emission components (e.g., the 262.00426GHz and 262.00648GHz lines given in rows 4 and 5 of Table 2 are hyperfine components for the C_2H ($N=3-2$, $J=7/2-5/2$) line). Since the disk J1100-7619 is bright and well-resolved, we are able to fit models to the resolved hyperfine structure (e.g., Hily-Blant et al. 2013; Estalella 2017; Pety 2018). We

can then extract excitation temperatures, column densities, and optical depths from the parameters of the fitted models, *through* each pixel in the image. By fitting the spectrum per pixel rather than across a larger disk area, we reduce the line width, and therefore line blending, of the hyperfine components in the spectrum. This in turn permits tighter constraints on the model fit. We use a hyperfine pixel-by-pixel procedure based on the work of Bergner et al. (2019), which in turn was adapted from the fitting procedure of Estalella (2017) and the calculations of Mangum & Shirley (2015). See Appendix B for the model equations, the fitting procedure, examples of model fits, and important discussion of intrinsic uncertainties.

3.3. Column Density Estimates

For lines where we cannot use the hyperfine fitting method to measure excitation temperatures, optical depths, and column densities directly, we can still estimate the column densities over a given disk region, using assumptions of the excitation temperature and total optical depth (e.g., from pixel-by-pixel hyperfine fits to the brightest disk), as well as a measurement of the total emission across all hyperfine components within that given disk region. This methodology is described in detail in Appendix C. Uncertainties are discussed in Appendix B.

4. RESULTS

4.1. Detections

We used the following criteria to determine whether or not a molecular line is detected toward a disk:

1. Emission is $\geq 3\sigma$ in the velocity-integrated emission map
2. Peak emission within the Keplerian masks is $\geq 3\sigma$ in at least 3 velocity channels

Lines that satisfy both criteria are *detected*, while lines that satisfy at least one criterion are *tentatively detected*. Lines that fail both criteria are *nondetected*.

Based on these criteria, we detect ^{12}CO ($J=2-1$), ^{13}CO ($J=2-1$), C^{18}O ($J=2-1$), HCN ($J=3-2$), C_2H ($N=3-2$, $F=7/2-5/2$), and C_2H ($N=3-2$, $F=5/2-3/2$) toward all 5/5 M4-M5 disks. We detect DCN ($J=3-2$) toward one disk (J1100-7619), and we detect H_2CO $3_{03}-2_{02}$ toward two disks (J0432+1827 and J1100-7619). For H_2CO 3–2 toward two other disks (FP Tau and Sz 69), and for DCN 3–2 toward four other disks (FP Tau, J0432+1827, J1545-3417, and Sz 69), the emission is tentatively detected and would be worth follow-up observations with deeper integration times.

Channel maps for the detections and tentative detections are presented in Appendix D. Table 4 presents the emission measurements for the dust continuum, and Table 5 presents

Table 5. Fluxes and Detection Upper Limits for Target Molecular Lines.

| Disk | 90% Em. Radius (AU) | Integrated Flux (mJy km s ⁻¹) | Peak Flux (mJy beam ⁻¹ × km s ⁻¹) | Integrated Velocity Range (km s ⁻¹) | Kep. Mask Extent (") | Channel Width (km s ⁻¹) | Channel rms (mJy beam ⁻¹) | Beam Size (P.A.) |
|---|---------------------------|---|--|---|----------------------------|---|---|-------------------------|
| (1) | (2) | (3) | (4) | (5) | (6) | (7) | (8) | (9) |
| ¹² CO (J=2-1) | | | | | | | | |
| FP Tau | 55 | 781 ± 11 | 247 ± 4.3 | 2.0 - 14.6 | 1.24 | 0.20 | 3.4 | 0.30" x 0.23" (-6.3°) |
| J0432+1827 | 126 | 1847 ± 13 | 129 ± 2.9 | 0.6 - 10.6 | 2.16 | 0.20 | 3.3 | 0.24" x 0.20" (-14.8°) |
| J1100-7619 | 186 | 1306 ± 6.1 | 69 ± 1.4 | 2.1 - 7.3 | 2.04 | 0.20 | 2.5 | 0.40" x 0.25" (-1.1°) |
| J1545-3417 | 98 | 738 ± 10 | 141 ± 3.3 | -1.0 - 10.0 | 2.00 | 0.20 | 3.7 | 0.27" x 0.24" (71.0°) |
| Sz 69 | 138 | 2001 ± 15 | 192 ± 3.0 | 1.2 - 9.4 | 2.68 | 0.20 | 3.8 | 0.27" x 0.24" (73.0°) |
| ¹³ CO (J=2-1) | | | | | | | | |
| FP Tau | 46 | 232 ± 8.3 | 100 ± 3.5 | 2.0 - 14.6 | 0.68 | 0.20 | 3.2 | 0.30" x 0.24" (-7.2°) |
| J0432+1827 | 81 | 537 ± 9.4 | 81 ± 2.9 | 0.6 - 10.6 | 1.32 | 0.20 | 3.0 | 0.25" x 0.21" (-13.4°) |
| J1100-7619 | 136 | 417 ± 6.0 | 38 ± 1.4 | 2.2 - 7.4 | 1.92 | 0.20 | 2.7 | 0.41" x 0.26" (-4.8°) |
| J1545-3417 | 80 | 218 ± 7.7 | 57 ± 3.1 | -1.0 - 10.0 | 1.32 | 0.20 | 3.3 | 0.28" x 0.25" (71.4°) |
| Sz 69 | 136 | 345 ± 13 | 60 ± 2.6 | 1.2 - 9.4 | 2.68 | 0.20 | 3.5 | 0.28" x 0.25" (72.7°) |
| C ¹⁸ O (J=2-1) | | | | | | | | |
| FP Tau | 44 | 91 ± 6.7 | 54 ± 3.3 | 1.9 - 14.7 | 0.56 | 0.40 | 2.1 | 0.30" x 0.24" (-7.1°) |
| J0432+1827 | 58 | 148 ± 9.0 | 36 ± 2.4 | 0.4 - 10.8 | 1.32 | 0.40 | 2.0 | 0.25" x 0.21" (-13.5°) |
| J1100-7619 | 116 | 71 ± 3.6 | 12 ± 1.2 | 2.2 - 7.4 | 1.36 | 0.20 | 2.1 | 0.42" x 0.27" (-2.3°) |
| J1545-3417 | 123 | 89 ± 9.5 | 21 ± 2.9 | -1.1 - 10.1 | 1.96 | 0.40 | 2.3 | 0.28" x 0.25" (69.1°) |
| Sz 69 | 37 | 38 ± 6.6 | 22 ± 2.5 | 1.4 - 9.4 | 0.96 | 0.40 | 2.2 | 0.29" x 0.25" (71.0°) |
| C ₂ H (N=3-2, J= $\frac{7}{2}$ - $\frac{5}{2}$) | | | | | | | | |
| FP Tau | 63 | 140 ± 18 | 81 ± 4.7 | 1.1 - 14.7 | 1.44 | 0.40 | 3.2 | 0.44" x 0.34" (-176.5°) |
| J0432+1827 | 104 | 288 ± 19 | 39 ± 4.3 | -1.6 - 10.0 | 1.32 | 0.40 | 3.0 | 0.34" x 0.24" (14.4°) |
| J1100-7619 | 167 | 1180 ± 17 | 22 ± 1.9 | -0.4 - 7.4 | 1.48 | 0.20 | 2.9 | 0.18" x 0.14" (-9.5°) |
| J1545-3417 | 56 | 61 ± 12 | 47 ± 3.0 | -1.9 - 9.7 | 1.16 | 0.40 | 2.6 | 0.37" x 0.33" (72.4°) |
| Sz 69 | 39 | 28 ± 8.1 | 25 ± 3.7 | -2.6 - 9.0 | 0.40 | 0.40 | 2.8 | 0.37" x 0.32" (72.9°) |
| HCN (J=3-2) | | | | | | | | |
| FP Tau | 48 | 272 ± 17 | 164 ± 4.4 | 2.0 - 14.6 | 1.20 | 0.20 | 4.2 | 0.38" x 0.25" (-173.8°) |
| J0432+1827 | 85 | 600 ± 18 | 125 ± 2.9 | -0.2 - 11.4 | 1.36 | 0.20 | 3.8 | 0.34" x 0.24" (14.3°) |
| J1100-7619 | 137 | 1655 ± 24 | 67 ± 1.6 | -0.2 - 9.8 | 1.64 | 0.20 | 2.6 | 0.18" x 0.14" (-9.1°) |
| J1545-3417 | 88 | 120 ± 14 | 51 ± 2.6 | -1.1 - 10.1 | 1.36 | 0.40 | 2.4 | 0.37" x 0.33" (70.1°) |
| Sz 69 | 39 | 42 ± 8.6 | 40 ± 3.4 | -0.2 - 11.0 | 0.44 | 0.40 | 2.6 | 0.37" x 0.33" (71.0°) |
| DCN (J=3-2) | | | | | | | | |
| FP Tau | — | ≲5.7 | ≲12 | 1.9 - 14.7 | 0.12 | 0.40 | 2.0 | 0.31" x 0.24" (-9.7°) |
| J0432+1827 | — | ≲18 | ≲9.1 | 0.4 - 10.8 | 0.48 | 0.40 | 2.0 | 0.26" x 0.21" (-16.5°) |
| J1100-7619 | 62 | 15 ± 2.7 | 8.3 ± 1.0 | 2.1 - 7.3 | 0.72 | 0.20 | 1.6 | 0.47" x 0.34" (-3.3°) |
| J1545-3417 | — | ≲14 | ≲8.7 | -1.1 - 10.1 | 0.36 | 0.40 | 2.2 | 0.29" x 0.26" (73.3°) |
| Sz 69 | — | ≲8.7 | ≲8.7 | 1.4 - 9.4 | 0.16 | 0.40 | 2.1 | 0.29" x 0.26" (75.0°) |
| H ₂ CO 3 ₀₃ -2 ₀₂ | | | | | | | | |
| FP Tau | — | ≲15 | ≲15 | 1.9 - 14.7 | 0.36 | 0.40 | 1.8 | 0.30" x 0.24" (-10.0°) |
| J0432+1827 | 136 | 80 ± 8.0 | 6.5 ± 2.1 | 0.4 - 10.8 | 1.48 | 0.40 | 1.7 | 0.26" x 0.21" (-17.7°) |
| J1100-7619 | 219 | 100 ± 3.7 | 7.7 ± 1.0 | 2.2 - 7.4 | 2.12 | 0.20 | 1.6 | 0.41" x 0.27" (-2.8°) |
| J1545-3417 | — | <14 | <7.2 | -1.1 - 10.1 | 0.40 | 0.40 | 1.9 | 0.29" x 0.26" (73.3°) |
| Sz 69 | — | ≲11 | ≲6.9 | 1.4 - 9.4 | 0.24 | 0.40 | 1.9 | 0.29" x 0.26" (74.7°) |

NOTE—*Em.* and *Kep.* are abbreviations of *Emission* and *Keplerian*, respectively. The emitting radii (column 2) are the radii containing 90% of the molecular line emission and are presented only for detections. The integrated and peak fluxes are measured within the Keplerian masks (column 6; Appendix A). Note the difference in unit between the two quantities. The errors for the integrated and peak fluxes and the channel rms were estimated via bootstrapping of 1000 random samples of non-emission channels. Samples for the integrated and peak fluxes were extracted from within the Keplerian masks, while the channel rms was extracted from within 2" × 2" regions. Uncertainties do not include ~15% systematic flux calibration uncertainties. 3σ upper limits are given for tentative detections and nondetections and are marked with a ≲ and <, respectively.

the flux measurements for the target molecular lines. All detections, tentative detections, and nondetections are marked within Table 5.

4.2. Emission Morphologies

Figure 2 displays the millimeter dust continuum emission and velocity-integrated molecular line emission maps. Figures 3 and 4 display the corresponding radial profiles and spectra, respectively. All dust continua appear smooth at this resolution (i.e., there are no cavities in the millimeter dust continuum emission). We use the 90% emitting radii of the dust continuum to represent the pebble disk edges. In terms of pebble disk size, J0432+1827 and J1100-7619 are the largest disks, while Sz 69 is the smallest disk. The 90% emitting radii for all CO isotopologues, C₂H 3–2, and HCN 3–2 emission is either comparable to or exceeds the pebble disk sizes, indicating that the gas of the disks is typically extended relative to the millimeter dust.

We use simple two-dimensional Gaussian fits to the dust continuum emission to estimate the center of each disk, and we qualitatively characterize peaks of the molecular line emission with respect to that disk center. All five disks in our sample have centrally-peaked CO isotopologue emission distributions. The ¹³CO and C¹⁸O emission distributions extend beyond the pebble disk edge (i.e., beyond ~30–60AU) for 4/5 and 3/5 disks, respectively. The disks FP Tau, J1545-3417, and Sz 69 are significantly affected by cloud contamination, which is evident in the CO spectra and the CO channel maps (Appendix D). The CO emission substructure seen beyond the pebble disk edges may be a byproduct of this contamination, but could also be a contribution from an extended disk structure or disk-envelope interaction. The disk J1100-7619 shows asymmetries in the ¹²CO spectrum. It is not clear what is causing these asymmetries, as the channel maps do not suggest cloud contamination.

2/5 disks have dips or holes in the C₂H 3–2 emission. The inner edge of the hole toward J1100-7619 is aligned with the edge of the pebble disk, between 46–63AU based on the 1.1 and 1.3mm dust continuum. This means that the majority of the C₂H emission is coming from beyond the pebble disk (e.g., [Bergin et al. 2016](#)). The hole in C₂H emission toward the second disk, J0432+1827, is off-center by ~0.1", appearing in Figure 2 but not in Figure 3. J0432+1827 additionally shows an emission plateau beyond the pebble disk. C₂H 3–2 emission toward the remaining three disks in our sample appears centrally peaked but is likely barely resolved. We clearly distinguish each hyperfine emission component (rows 4 and 5 of Table 2) in the C₂H 3–2 spectrum toward J1100-7619, while the C₂H and HCN hyperfine components for all other disks are blended (Figure 4).

All disks have centrally-peaked HCN 3–2 emission morphologies. The two well-resolved disks, J0432+1827 and

J1100-7619, have more compact HCN emission compared to the C₂H emission. Both disks also show plateaus or shelves in the HCN emission beyond the pebble disk edge. The remaining three disks may also show substructure exterior to the pebble disk at higher spatial resolution. DCN 3–2 is only detected toward J1100-7619, where the emission is centrally-peaked and extends just beyond the edge of the pebble disk.

When detected, H₂CO 3–2 emission shows a hole or depression near the disk center. J0432+1827 has a central hole in H₂CO emission and suggestive rings that extend past the dust continuum. J1100-7619 has a hole in H₂CO emission that is off-center by <0.1", which appears in Figure 2 but not Figure 3, with two rings that peak at and beyond the pebble disk edge.

4.3. Relative Line Fluxes toward Disks around M4-M5 Stars and Solar-Type Stars

We now compare relative line fluxes (i.e., the flux for one molecular line with respect to the flux of a different molecular line) for the M4-M5 disks in this work to relative line fluxes measured for solar-type and Herbig Ae disks in the literature. The literature disk sample was compiled from the chemistry surveys of [Huang et al. \(2017\)](#), [Bergner et al. \(2019\)](#), [Bergner et al. \(2020\)](#), and [Pegues et al. \(2020\)](#). We use only the molecular line+disk pairs in these surveys that were detected with ALMA, leading to thirteen unique disks in all with at least two detections of C¹⁸O, C₂H, DCN, HCN, and H₂CO line emission. C¹⁸O 2–1 was detected with ALMA toward 11/13 disks, C₂H 3–2 toward 10/13 disks, DCN 3–2 toward 10/13 disks, HCN 3–2 toward 7/13 disks, and either H₂CO 3₀₃-2₀₂ or 4₀₄-3₀₃ toward 13/13 disks. We consider both H₂CO 3₀₃-2₀₂ and H₂CO 4₀₄-3₀₃ line fluxes from the literature, because both lines have similar flux behaviors ([Pegues et al. 2020](#)). Stellar masses and spectral types for the T Tauri disks in this combined literature sample range from ~0.4–1.8M_☉ and M1–G7, respectively. Two Herbig Ae disks (HD 163296 and MWC 480, A-star disks with stellar masses of ~1.8–2.0M_☉) are included in the literature disk sample. We include the two Herbig Ae disks in relevant figures and tables for completeness, but since there are only two of them, we focus mainly on comparisons with the solar-type disk sample in later discussion.

Figure 5 plots distance-normalized C¹⁸O fluxes as a function of stellar mass across the combined sample of disks. The combined sample appears to follow the same trend in C¹⁸O vs. stellar mass. The addition of the M4-M5 disks suggests a positive dependence of C¹⁸O flux on stellar mass across the sample, which was not distinguishable from the solar-type and Herbig Ae disk samples alone.

Figure 6 compares distance-normalized line fluxes between the M4-M5 and literature disk samples. The Spearman correlation coefficients (r), which show how well the

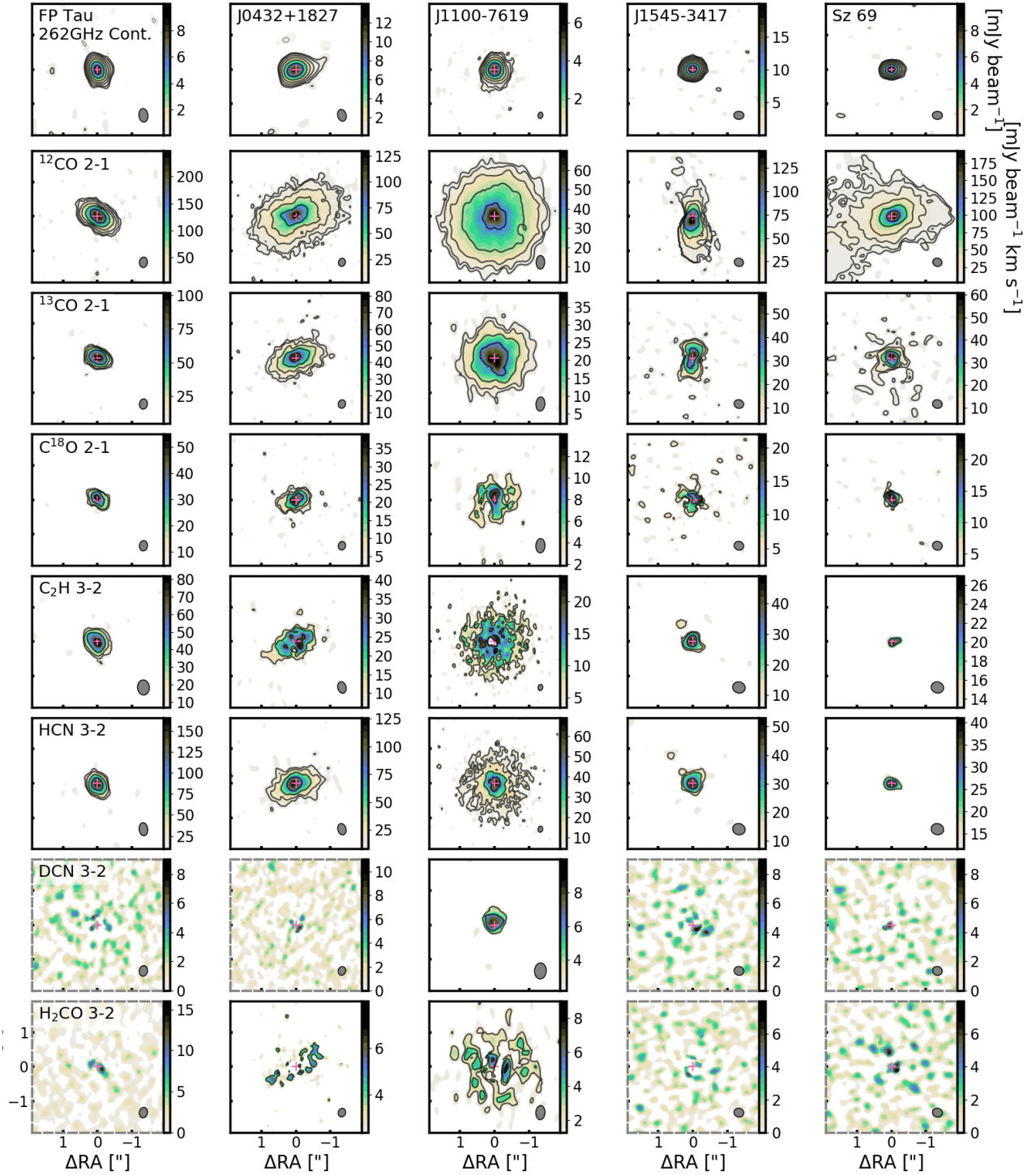


Figure 2. Dust continuum emission and velocity-integrated emission maps for the molecular lines. Each column corresponds to a different disk. The top row shows the 1.1mm (262GHz) dust continuum emission for each disk. All subsequent rows show velocity-integrated molecular line emission. Contours are shown at the $[3\sigma, 5\sigma, 10\sigma, 20\sigma\dots]$ levels. σ is equal to the rms for the dust continuum emission (Table 4) and to σ_{map} for the velocity-integrated emission (Section 3.1). Disk centers are marked with + signs. Beams are drawn in the lower right corners. Subplots for tentative/nondetections are outlined in dashed gray rather than black, and their colorbars start at 0. Colorbars for detections start at $2\sigma_{\text{map}}$.

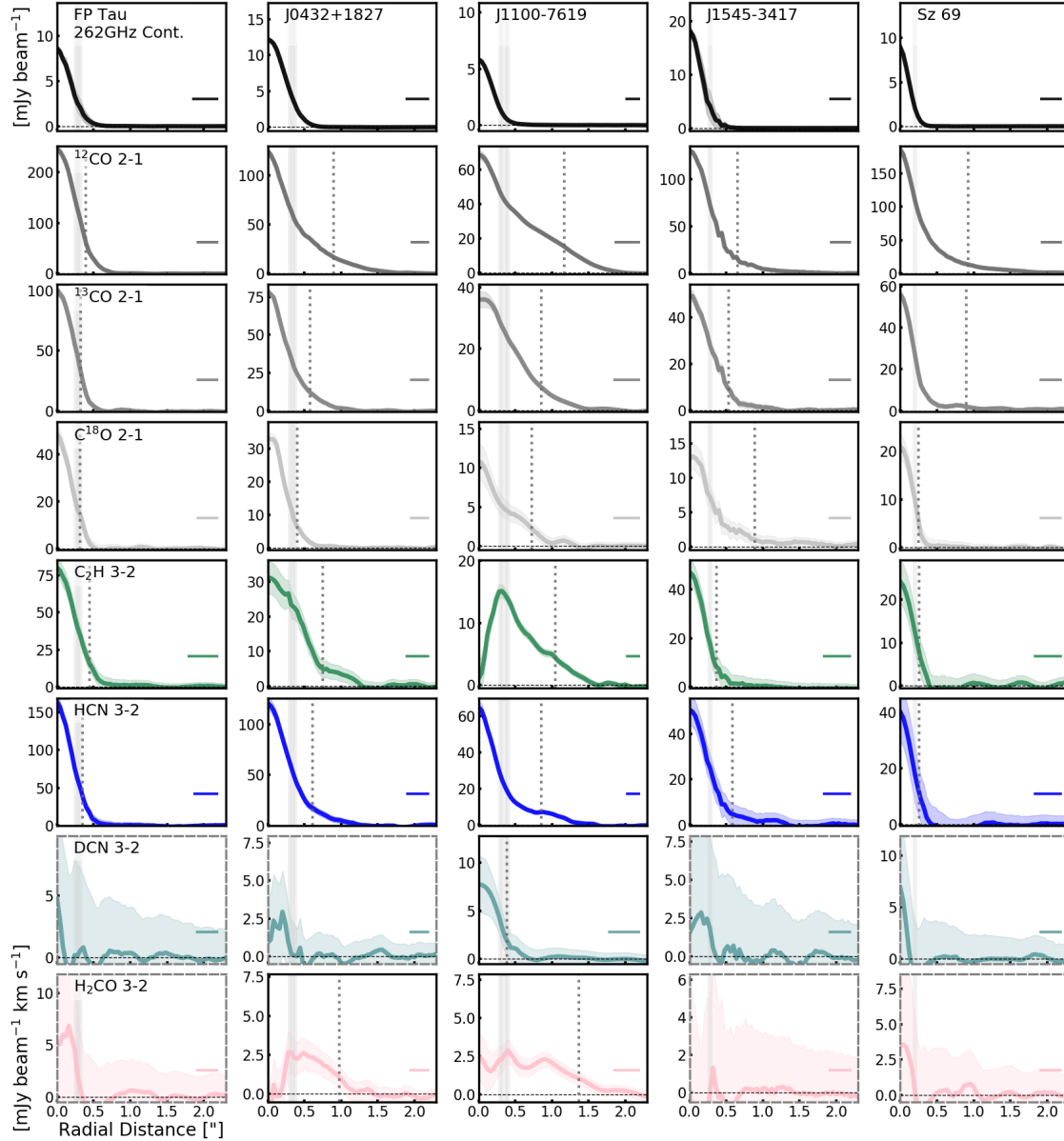


Figure 3. Radial profiles for the 1.1mm (262GHz) dust continuum and the molecular lines in the sample. Each column corresponds to a different disk. The top row displays the dust continuum radial profiles (in black). The subsequent rows display the CO isotopologues (in grays), C₂H (green), HCN and DCN (blues), and H₂CO (pink) lines. For the dust continuum radial profiles, the shaded regions are the standard deviation of the emission within each annulus. For the molecular emission radial profiles, the shaded regions depict the 1σ uncertainties of each annulus as described in Section 3.1. The vertical light gray shaded regions show the 90% emitting radii of the 1.1mm and 1.3mm (231GHz) dust continuum. The vertical dark gray dashed lines mark the 90% emitting radii for each detected molecular line. Beam sizes are represented by the horizontal bars in the lower right corners. Subplots for tentative/nondetections are outlined in dashed gray rather than black.

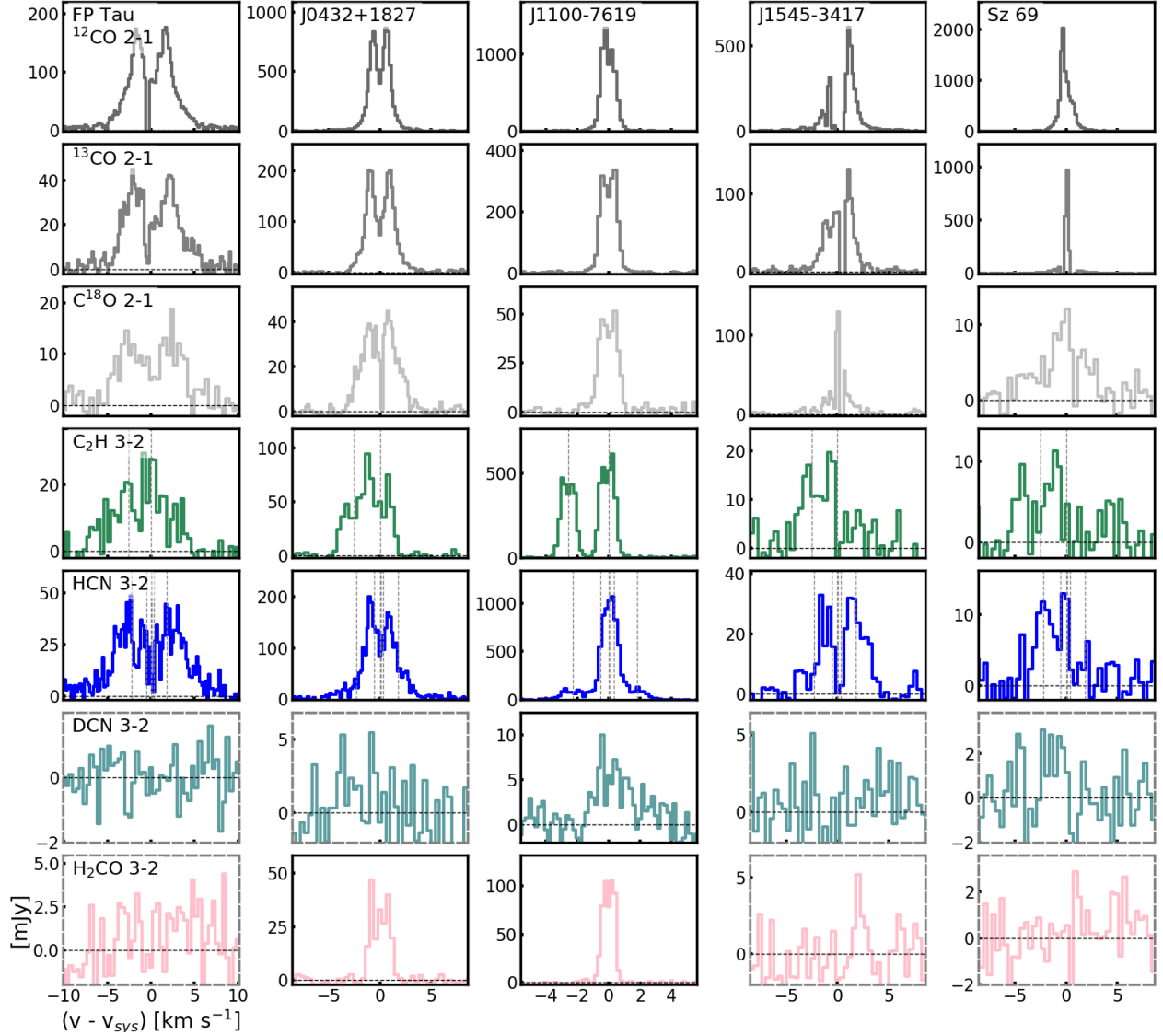


Figure 4. Spectra for the molecular lines in the sample. Each column corresponds to a different disk. The rows display the CO isotopologues (in grays), C₂H (green), HCN and DCN (blues), and H₂CO (pink) lines. Hyperfine components for C₂H 3–2 and HCN 3–2 are marked with vertical dashed gray lines. The assumed systemic velocities (v_{sys}) are given in Appendix A. The two hyperfine components for C₂H 3–2 toward J1100-7619, centered at $(v - v_{\text{sys}})$ of ~ 0 km/s and ~ -2.5 km/s, are clearly separable by eye. The hyperfine components for HCN 3–2 toward J1100-7619, along with all hyperfine components toward all other disks, are blended. Subplots for tentative/nondetections are outlined in dashed gray rather than black.

data can be described by a monotonic function, are shown when the associated p-value is ≤ 0.01 . All correlation coefficients and measures of statistical significance are presented and explained in Appendix E. The line fluxes are often lower for the M4-M5 disks than for the solar-type and Herbig Ae disks. J1100-7619, which is particularly bright in C₂H and HCN emission, is a notable exception. Despite differences in individual fluxes, trends found between fluxes for solar-type and Herbig Ae disks seem to apply to M4-M5 disks. The strongest correlations across the M4-M5, solar-type, and Herbig Ae disk samples are found between C₂H 3–2 and HCN 3–2 ($r=0.92$, p-value <0.001) and

H₂CO and HCN 3–2 ($r=0.92$, p-value <0.001). Notably C₂H 3–2 and HCN 3–2 are perfectly correlated for the M4-M5 disks alone ($r_{\text{M4-M5}}=1.00$, p-value <0.001). For the combined sample, the trends between the C₂H 3–2 vs. C¹⁸O 2–1 line fluxes and the HCN 3–2 vs. C¹⁸O 2–1 line fluxes are similar to each other ($r=0.81$, p-value <0.001 and $r=0.88$, p-value <0.001 , respectively). We also find a weak correlation between H₂CO line fluxes and C¹⁸O 2–1 ($r=0.69$, p-value=0.01). All other pairs of line fluxes do not appear to be significantly correlated.

We note that while we expect H₂CO and DCN line emission to be optically thin, studies have shown that C₂H and

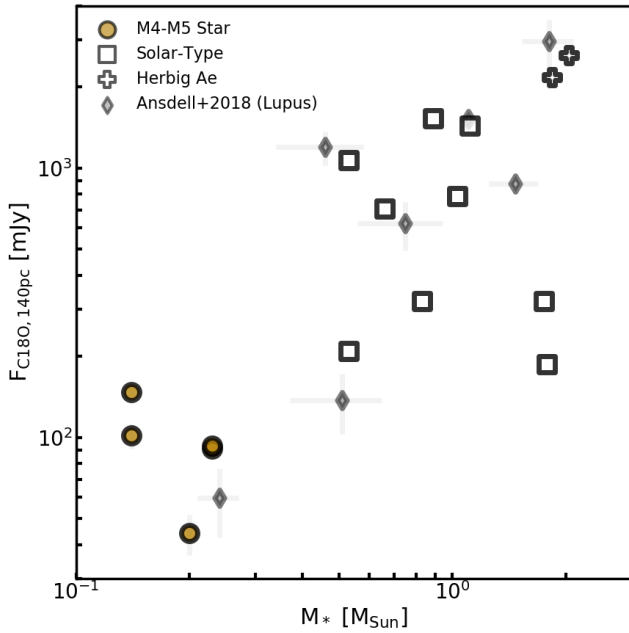


Figure 5. The $C^{18}O$ fluxes for the M4-M5 disk sample as a function of stellar mass, compared to disks compiled from the literature. The dark gold circles are $C^{18}O$ fluxes for M4-M5 disk detections from this work. The white points are ALMA-observed $C^{18}O$ ($J=2-1$) fluxes for solar-type disks (marked with squares) and Herbig Ae disks (marked with crosses). These disks were compiled from Huang et al. (2017), Bergner et al. (2019), Bergner et al. (2020), and Pegues et al. (2020) and are described in Section 4.3. The thin diamonds are disks detected in $C^{18}O$ ($J=2-1$) from Ansdell et al. (2018), which surveyed the Lupus star-forming region. All fluxes have been scaled to 140pc.

HCN line emission is often optically thick (e.g., Bergner et al. 2019). It is thus possible that the C_2H 3–2 and HCN 3–2 molecular line fluxes trace the distribution size rather than the underlying molecular abundance. We investigate this possibility in Appendix F, and we find evidence that the strong correlation between the C_2H 3–2 and HCN 3–2 fluxes likely cannot be explained by optical depth effects alone.

We plot a subset of the disk flux ratios for the M4-M5, solar-type, and Herbig Ae disks against stellar mass in Figure 7. The flux ratio subset includes molecular line emission relative to $C^{18}O$ 2–1 emission, which tells us how the molecular line emission relates to the disk gas. We also include the strongly correlated C_2H 3–2 vs. HCN 3–2 and the deuterated fraction DCN 3–2 vs. HCN 3–2. We note that the C_2H 3–2 / HCN 3–2 flux ratios for the M4-M5 disks are similar in value to each other. The C_2H 3–2 / HCN 3–2 flux ratios for the M4-M5 disks are high relative to the typical C_2H 3–2 / HCN 3–2 flux ratios for the solar-type disks. Otherwise, we find no clear trend for any of the disk molecular line flux ratios in either the individual or combined disk samples. The ratios across all samples appear flat relative to stellar mass and also to stellar luminosity (not shown). The lack of any trends be-

tween molecular line flux ratios and stellar mass, despite the clear trends between the millimeter dust continuum fluxes, $C^{18}O$ fluxes, and stellar masses in Figures 1 and 5, suggests that the underlying disk chemistry is similar for the M4-M5 and solar-type stars in the outer disk regions probed by our disk-integrated fluxes.

4.4. Case Study: J1100-7619

J1100-7619 presents the brightest molecular emission in our sample and was observed with the highest spatial resolution. We therefore use J1100-7619 to explore how the chemistry changes with disk radius around an M4-M5 star.

4.4.1. Radial Fluxes

Figure 8 shows disk-averaged and azimuthally-averaged (radial) molecular flux ratios toward J1100-7619 for the same molecule pairs as in Figure 7. The (C_2H 3–2 / $C^{18}O$ 2–1) and (H_2CO 3–2 / $C^{18}O$ 2–1) ratios both increase across the disk. There is a notable bump in the (H_2CO 3–2 / $C^{18}O$ 2–1) ratio that appears at ~ 80 AU, just beyond the edge of the pebble disk. The (DCN 3–2 / HCN 3–2) and (HCN 3–2 / $C^{18}O$ 2–1) ratios are both roughly constant across the disk where significant signal-to-noise exists, with values of $\sim (1.5-3.0) \times 10^{-2}$ and $\sim 20-30$, respectively. The (C_2H 3–2 / HCN 3–2) ratio increases across the pebble disk, and then flattens out beyond the pebble disk edge. Past ~ 100 AU, the (C_2H 3–2 / HCN 3–2) ratio is notably constant, with values of $\sim 0.8-0.9$.

4.4.2. Excitation Temperatures, Column Densities, and Optical Depths

Where sufficient signal-to-noise exists for J1100-7619, we use the pixel-by-pixel hyperfine fitting procedure described in Section 3.2 and Appendix B. This procedure allows us to estimate excitation temperatures, column densities, and optical depths for C_2H and HCN within each pixel. Although we proceed with this procedure, we note that these hyperfine fits are subject to significant intrinsic uncertainties (see Appendix B).

To increase the velocity resolution of the hyperfine fits, we reimaged the C_2H 3–2, C_2H ($N=3-2$, $J=5/2-3/2$), and HCN 3–2 line emission at channel widths of 0.14 km s^{-1} prior to performing the fits. After the fitting procedure, we performed weighted averages of pixel values within each annulus around the host star. The weighting process is described in Appendix B. We used this procedure to create weighted radial profiles of the excitation temperatures, column densities, and optical depths, which are plotted in Figure 9.

C_2H excitation temperatures are $\sim 10-20 \text{ K}$ and appear roughly constant across the disk. These low temperatures suggest either thermal emission from the disk midplane or subthermal emission from an upper disk layer. C_2H optical depths range from $\sim 1-4$ and are also roughly constant with

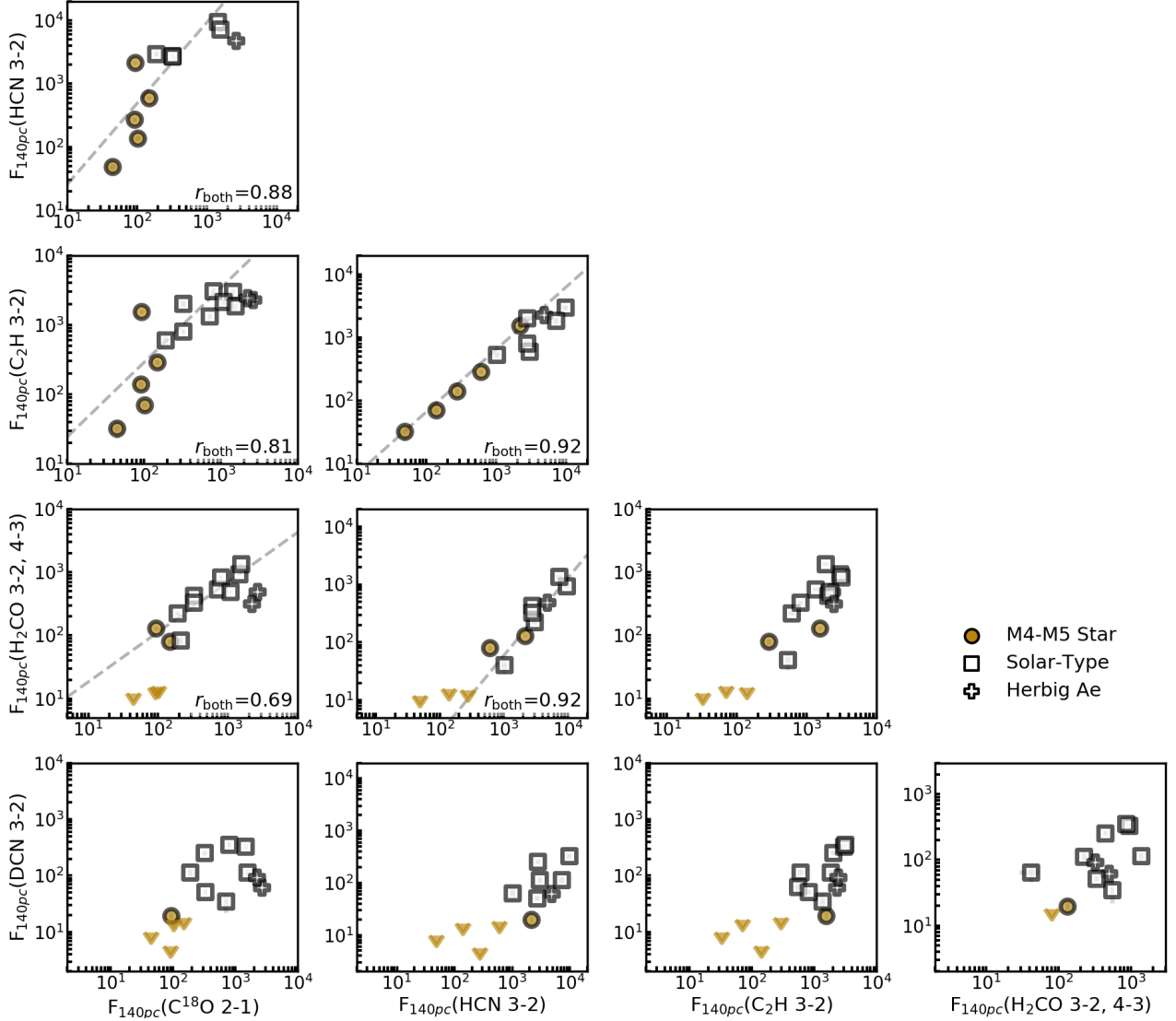


Figure 6. Molecular line fluxes toward the M4-M5 disks (dark gold circles), the solar-type disks (white squares), and the two Herbig Ae disks (white crosses). The x and y-axes show the integrated fluxes (scaled to 140pc) for a particular molecular line, which are listed along the bottom and left sides, respectively, of the entire figure. The dark gold triangles are 3σ upper limits for M4-M5 disk tentative detections/nondetections and point in the direction of the limit. Points where both the x and y-axes are upper limits are not shown. The M4-M5 disks are from this work, while the solar-type and Herbig Ae disks were compiled from ALMA observations of [Huang et al. \(2017\)](#); [Bergner et al. \(2019, 2020\)](#); [Pegues et al. \(2020\)](#). Spearman correlation coefficients across all detections are written in the bottom-right of each plot whenever they are statistically significant. The dashed gray lines are linear fits to the log data with statistically significant Spearman correlations (excluding the upper limits). These lines indicate how well the data would adhere to a power law distribution in linear space.

radius. C_2H column densities are $\sim(10-1)\times 10^{14} \text{ cm}^{-2}$ over $\sim 20-100\text{AU}$ and appear roughly flat with radius.

The signal-to-noise for HCN is sufficient only for probing interior to the pebble disk edge (from $\sim 20-60\text{AU}$). In this region, HCN excitation temperatures are roughly constant. These temperatures are slightly warmer but still consistent with the C_2H excitation temperatures. HCN is optically thick in this region, with optical depths decreasing from $\sim 15-7$. HCN column densities are from $\sim(30-3)\times 10^{13} \text{ cm}^{-2}$. The HCN column density profile decreases steeply in comparison

to the C_2H column density profile over the same portion of the disk.

[Bergner et al. \(2019\)](#) used their pixel-by-pixel hyperfine procedure to derive C_2H and HCN excitation temperature and column density constraints for their sample of solar-type and Herbig Ae disks. When we compare the J1100-7619 results with their solar-type and Herbig Ae disk sample, we find that our estimated excitation temperatures and optical depths across the pebble disk for J1100-7619 are consistent with estimates for the disks around more massive stars.

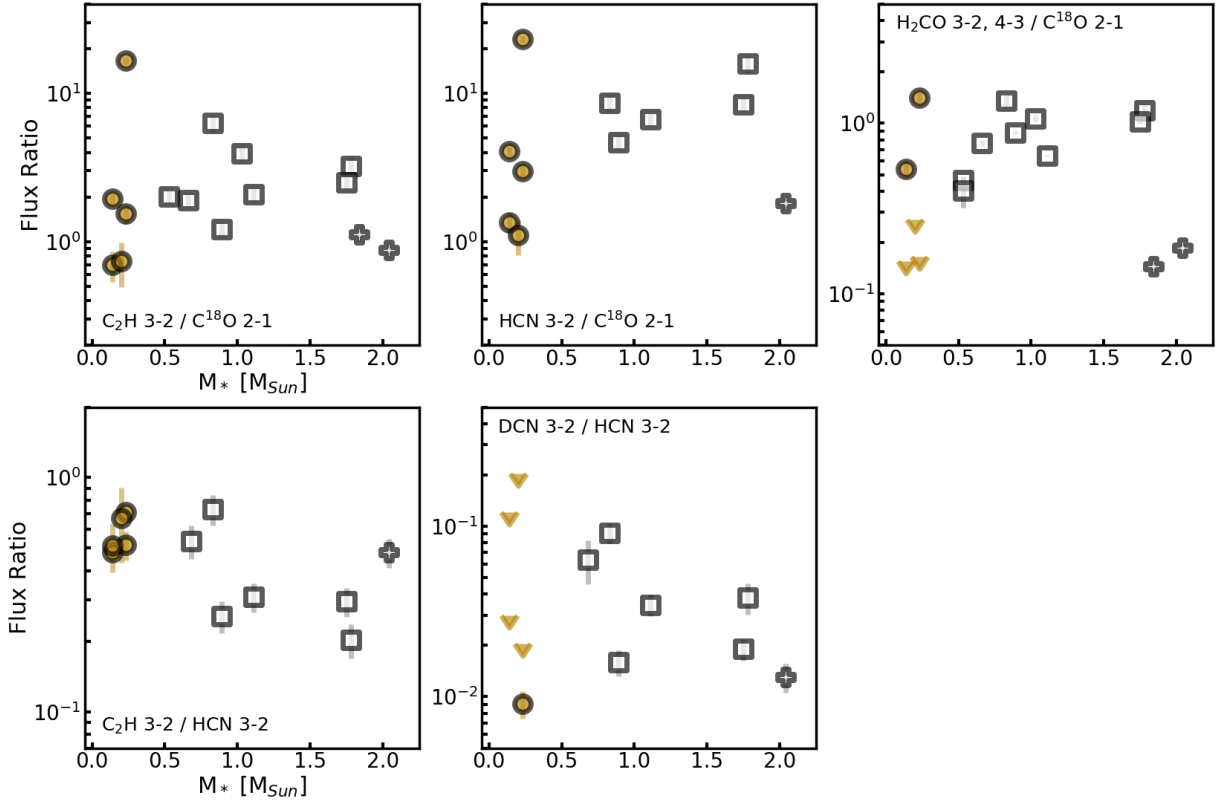


Figure 7. Relative flux ratios for different molecular lines toward the M4-M5 disks (dark gold circles and dark gold triangles for detections and 3σ upper limits, respectively), the solar-type disks (white squares), and the two Herbig Ae disks (white crosses), plotted as a function of stellar mass. The M4-M5 disks are from this work, while the solar-type and Herbig Ae disks were compiled from ALMA observations of [Huang et al. \(2017\)](#); [Bergner et al. \(2019, 2020\)](#); [Pegues et al. \(2020\)](#).

4.5. Disk-Averaged Column Densities

We now use the methodology described in Section 3.3 and Appendix C to estimate disk-averaged C_2H , DCN, and HCN column densities for the entire M4-M5 disk sample. For each molecular line and disk, we take the extent of the emission to be where the emission radial profile decreases to 1σ . We extract emission only within that radius, and we use that radius to define the angular size Ω of the disk (see Appendix C).

We assume that the disk-averaged excitation temperatures range from 10-30K for both molecules, with a median value of 20K. For disk-averaged optical depths, we assume 1-5 with a median of 2 for C_2H and 4-12 with a median of 8 for HCN. We also estimate disk-averaged column densities for DCN, assuming that DCN is optically thin and has the same excitation temperature and conditions as C_2H and HCN.

Figure 10 displays the estimated disk-averaged C_2H and HCN column densities for the M4-M5 disk sample using the disk-averaged median, minimum, and maximum excitation temperature and optical depth constraints. The median C_2H column density estimates are $(5-10)\times 10^{13} \text{ cm}^{-2}$ across the sample. Changing the excitation temperature and opacity result in factors of 2-4 higher or lower estimates of the column density. These values, which were estimated using the

C_2H ($N=3-2$, $J=7/2-5/2$) line, are consistent with those estimated using the C_2H ($N=3-2$, $J=5/2-3/2$) line (not shown). The median HCN column density estimates span a factor of 3, from $(4-12)\times 10^{12} \text{ cm}^{-2}$. Changes in optical depth from 4 to 12 lead to factors $\lesssim 3$ in difference between estimates, while changes in excitation temperature from 10K to 30K lead to factors of $\sim 3-10$ (excluding Sz 69). For the bright and well-resolved disk J1100-7619, DCN is detected, and the estimated column densities (not shown) span $\sim (4-10)\times 10^{11} \text{ cm}^{-2}$ from 10-30K with a median of $\sim 7\times 10^{11} \text{ cm}^{-2}$.

Figure 10 also displays the estimated disk-averaged C_2H/HCN and DCN/HCN column density ratios. These are plotted in comparison to the 16th, median, and 84th percentiles derived from a sample of disk-averaged ratios from the literature for solar-type and Herbig Ae disks ([Huang et al. 2017](#); [Bergner et al. 2020](#)). We used only the disk-averaged ratios from these references that were observed with ALMA and had comparable excitation temperature and optical depth assumptions. Detailed descriptions of the excitation temperatures and optical depths assumed in the literature are given in Appendix C.

For all M4-M5 disks, estimates of the disk-averaged C_2H/HCN ratio do not change significantly with optical

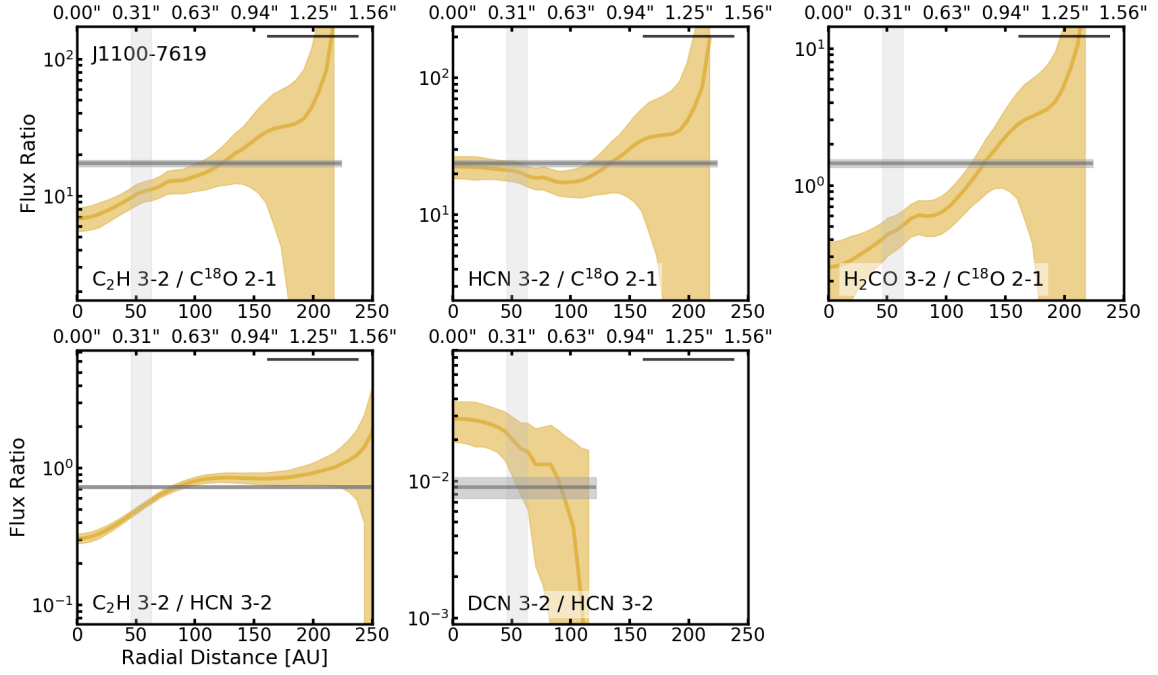


Figure 8. Radially resolved flux ratios for different molecular lines observed toward J1100-7619. The error per annulus is given by $|F_t/F_b| \times \sqrt{(\sigma_t/F_t)^2 + (\sigma_b/F_b)^2}$, where F is the flux in that annulus, σ is the radial profile error (described in Section 3.1), and the subscripts t and b refer to the molecular lines at the top and bottom, respectively, of the ratio. The beam sizes are represented by the horizontal bars at the top right of each plot. The beams of the line images were smoothed and circularized to the same size before the ratios were computed. The horizontal gray lines and shaded regions depict the disk-averaged flux ratios and error, respectively. These regions extend horizontally to the minimum boundary within which the disk-averaged fluxes were measured (i.e., the minimum Keplerian mask extent for the molecular lines; Appendix A). The vertical gray regions are from the edges of the 1.1mm (262GHz) to the 1.3mm (231GHz) dust continuum (Table 4).

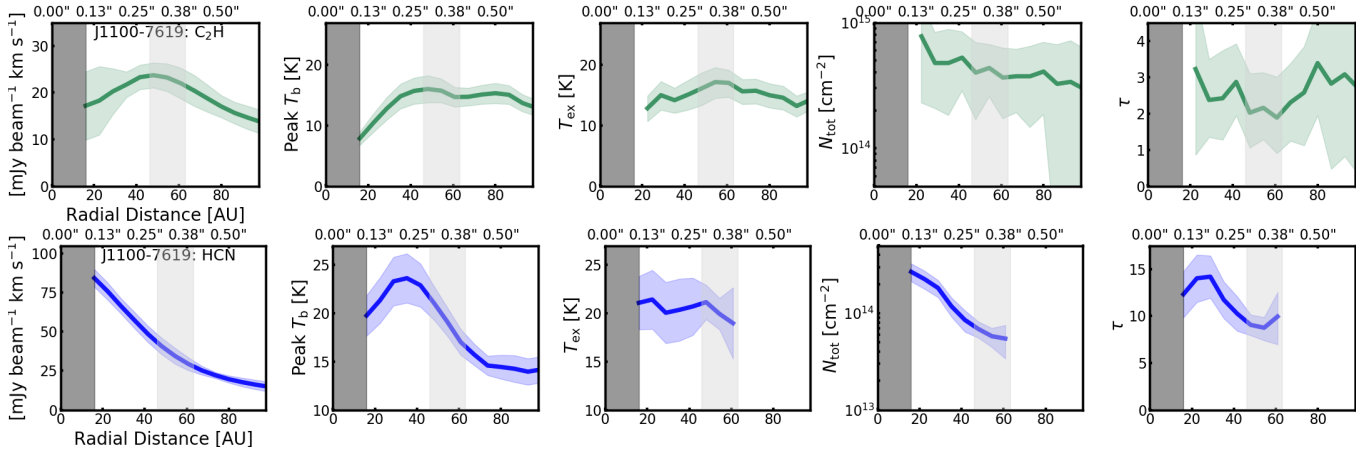


Figure 9. Radial flux profiles (column 1), peak brightness temperatures (column 2), and excitation temperatures, column densities, and optical depths (columns 3, 4, and 5, respectively) estimated from the pixel-by-pixel hyperfine fits toward J1100-7619. The top and bottom rows display the results for C_2H (green) and HCN (blue), respectively. For columns 1 and 2, the shaded uncertainties are the standard deviations of the emission/temperature within each $0.04''$ annulus. The profiles shown in columns 3 through 5 are the weighted azimuthal averages of the values within each $0.04''$ annulus (Appendix B). The vertical dark gray region to the left of each plot represents the beam size. We exclude emission within the beam size to avoid unresolved emission within that region. The vertical pale gray regions are from the edge of the 1.1mm (262GHz) dust continuum to the edge of the 1.3mm (231GHz) dust continuum (Table 4).

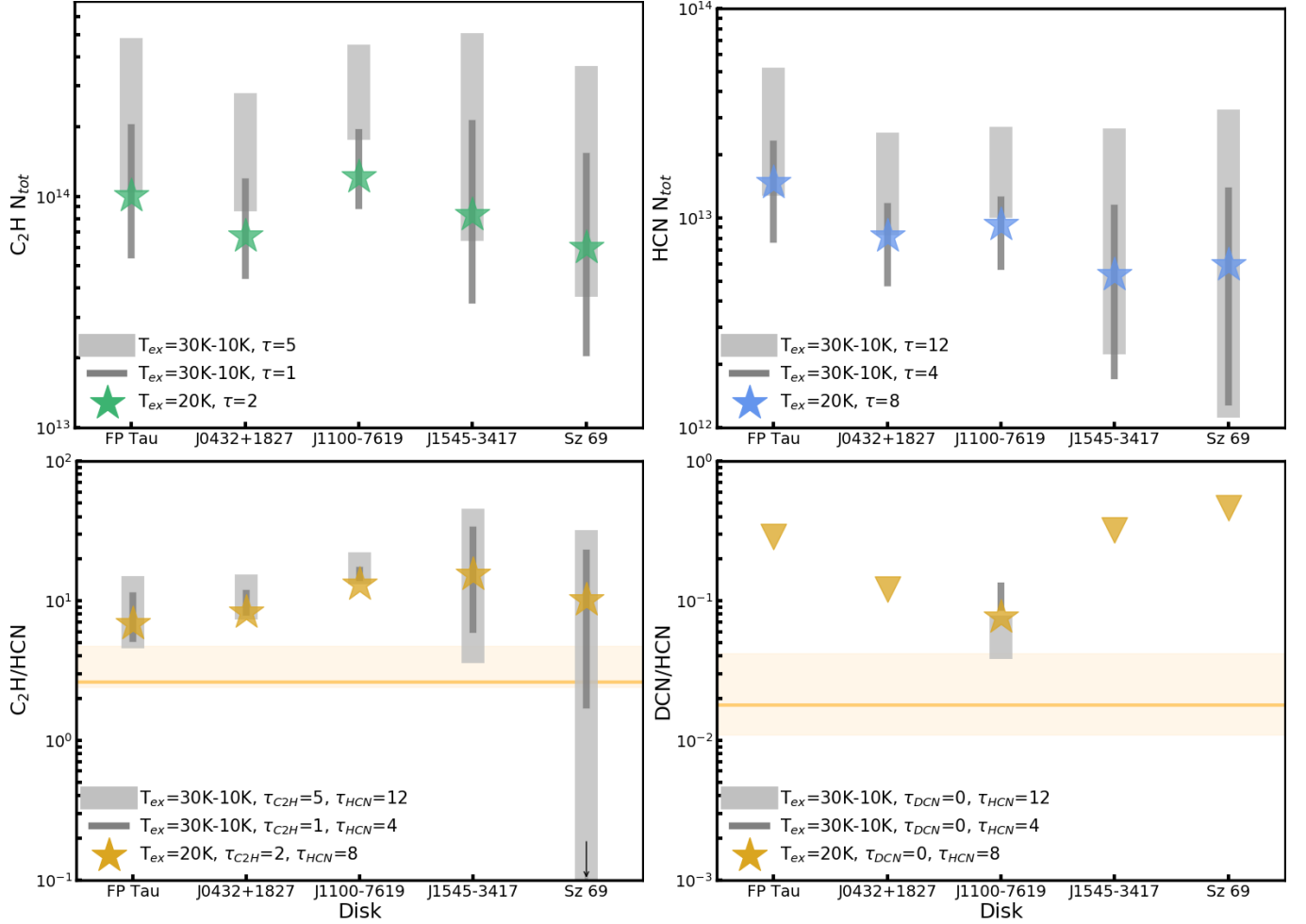


Figure 10. Disk-averaged column density estimates for C_2H (top left) and HCN (top right) for the entire M4-M5 disk sample, as well as estimates of the disk-averaged C_2H/HCN (bottom left) and DCN/HCN (bottom right) ratios. The estimates were computed using the methodology described in Section 3.3 and Appendix C. For detections, the emission and disk areas were measured interior to where the emission radial profile reached 1σ . For upper limits, the 3σ errors and disk areas were measured within the bounds of the Keplerian masks (Appendix A). Each estimate assumes an excitation temperature and optical depth (listed at the bottom left of each panel). The stars and triangles represent median estimates and 3σ upper limits, respectively. Each gray bar gives a range of estimates assuming excitation temperatures from 10-30K and include error. For the ratio plots, the horizontal dark lines and shaded regions correspond to the median and 16th-84th percentile range, respectively, for a subset of ALMA-observed solar-type and Herbig Ae disks from the literature (Huang et al. 2017; Bergner et al. 2020) (Appendix C).

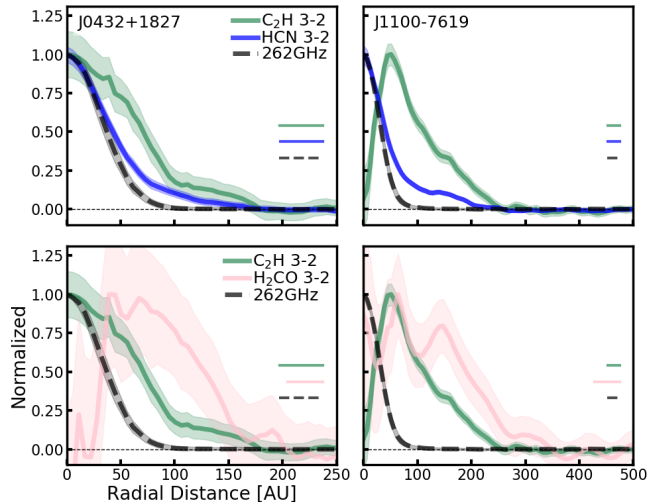


Figure 11. Normalized radial profiles of molecular line emission (adapted from Figure 3) toward J0432+1827 (left column) and J1100-7619 (right column). The profiles depicted are of C₂H 3–2 (green), HCN 3–2 (blue), and H₂CO 3–2 (pink), with the 1.1mm dust continuum emission profiles (dashed black) also shown for comparison. The beam sizes are represented by the horizontal bars in the lower right corners.

depth. Median estimates of the ratio range from ~ 7 for FP Tau to ~ 11 for J1545-3417. Notably all C₂H/HCN estimates for the M4-M5 disks exceed the 84th percentile of the solar-type and Herbig Ae disk C₂H/HCN estimates. The DCN/HCN estimates are relatively well constrained for J1100-7619. This disk has a median DCN/HCN value of ~ 0.072 and ranges from ~ 0.04 -0.1 across the extremes. This single value exceeds the 84th percentile disk-averaged DCN/HCN ratio found for the solar-type and Herbig Ae disks, although we would need more DCN detections toward M4-M5 disks to determine if this finding is representative of a larger sample.

5. DISCUSSION

5.1. Chemical Origins of Observed Emission Patterns

The molecular emission morphologies we observe are products of the local chemistry and environment. Here we discuss the observed emission morphologies across our M4-M5 disk sample in the context of chemical pathways and environmental conditions that may form them. For recent, in-depth discussion of formation pathways and conditions for each molecule, refer to Huang et al. (2017) (HCN and DCN), Bergner et al. (2019) (C₂H and HCN), and Pegues et al. (2020) (H₂CO).

5.1.1. C₂H and HCN

Observational studies have found significant positive correlations between HCN and C₂H line fluxes for solar-type disks (stellar masses of ~ 0.5 -1.8M_⊙; Bergner et al. 2019),

along with significant positive correlations between CN and C₂H line fluxes for both low-mass M-star (stellar masses $< 0.5M_{\odot}$) and solar-type disks (Miotello et al. 2019). These studies concluded that production of these molecules can be traced to the same or similar chemical and/or physical driver(s). Theoretical studies of T Tauri disks (Du et al. 2015; Bergin et al. 2016) have found that depletions of oxygen relative to carbon and heightened UV irradiation are likely major drivers, as they can cause increased production of C₂H, other hydrocarbons, and cyanides in the outer T Tauri disk regions. Simulated observations of C₂H have shown that this increased production can be observed as rings in the hydrocarbon emission (Bergin et al. 2016).

It is difficult to isolate physical/chemical driver(s) and how they are tied to emission morphologies without detailed modeling. That being said, we note two intriguing similarities between C₂H and HCN beyond the pebble disk edges of our sample: morphologies and relative fluxes and column densities, which together point toward a related chemistry beyond the pebble disk. First, the two well-resolved disks in the sample (J0432+1827 and J1100-7619; Figure 11) show slope changes and suggestive plateaus in both C₂H and HCN emission beyond the pebble disk. Second, the disk (C₂H 3–2 / HCN 3–2) flux ratios (Figures 6 and 7) appear perfectly correlated across the M4-M5 disk sample. The radially resolved (C₂H 3–2 / HCN 3–2) flux ratio toward J1100-7619 helps us understand this correlation, because the ratio is virtually constant beyond the pebble disk edge (Figure 8). The estimated disk-averaged C₂H/HCN column density ratios (Figure 10), which are influenced most heavily by contributions from the outer disk, are similar across the M4-M5 disk sample.

It is important to note how the C₂H and HCN column density profiles measured across the pebble disk for J1100-7619 (Figure 9) are different in shape, with the HCN column densities decreasing more steeply across the pebble disk than the C₂H column densities. This difference may indicate that the C₂H and HCN chemistry is decoupled and/or affected by different physical/chemical processes interior to the pebble disk edge. This further suggests that the similarities and correlations between C₂H and HCN morphologies, fluxes, and disk-averaged column densities discussed here are driven by the emission *beyond* the pebble disk.

5.1.2. H₂CO, CO, and C₂H

H₂CO can form efficiently through either gas-phase pathways, which are expected to be most efficient in warm and dense disk regions, or through the grain-surface hydrogenation of CO ice, which is expected to be prominent beyond the CO snowline (e.g., Hiraoka et al. 1994; Fockenberg & Preses 2002; Hiraoka et al. 2002; Watanabe & Kouchi 2002; Hidaka et al. 2004; Watanabe et al. 2004; Atkinson et al. 2006; Fuchs et al. 2009). Toy disk models, detailed chemical mod-

eling, and observations of H₂CO in multiple T Tauri disks have shown that both pathways can contribute significantly to H₂CO emission in disks (e.g., Loomis et al. 2015; Carney et al. 2017; Öberg et al. 2017; Pegues et al. 2020), producing central peaks and/or outer rings in the emission.

H₂CO is clearly detected toward two disks (J0432+1827 and J1100-7619; Figure 11) in the M4-M5 disk sample. For both disks, there are peaks in the H₂CO emission that are at/beyond the edge of the pebble disk. The hole in C₂H emission toward J0432+1827 is off-center relative to the dust continuum estimate by $\sim 0.1''$ and difficult to interpret, but we do note intriguing alignments in the H₂CO and C₂H emission for J1100-7619 (Figure 11). The first ring in H₂CO emission toward this disk is roughly aligned with the peak in the C₂H emission at ~ 60 AU, and both peaks are located near the edge of the pebble disk. The second ring in H₂CO emission is roughly aligned with a small bump in the C₂H emission at ~ 150 AU. The H₂CO emission peaks do not appear to be direct consequences of the CO snowline: assuming a simple radial temperature profile with a power law exponent of 0.55, a temperature of 142 K at 1 AU (the averages for M-star disks from Andrews & Williams 2007), and CO midplane freeze-out temperatures of 18-26 K (e.g., Öberg et al. 2011a), we estimate upper limits on the CO snowline of ~ 22 -43 AU, which are interior to both H₂CO peaks.

These alignments suggest a link in H₂CO and C₂H formation in these disks. It is possible that UV photodesorption of CO ice explains both the H₂CO emission and the apparent link in H₂CO and C₂H formation beyond the pebble disk. On grain surfaces, this non-thermal mechanism may ultimately release emission from H₂CO produced via CO ice hydrogenation (e.g., discussion by Walsh et al. 2014; Loomis et al. 2015; Öberg et al. 2017; Féraud et al. 2019). Simultaneously in the gas phase, this same mechanism is hypothesized to cause increased gas-phase atomic carbon abundances and lead to enhanced hydrocarbon production, including of C₂H (Du et al. 2015). Those enhanced hydrocarbons may produce H₂CO through its gas-phase pathways as well (e.g., through the neutral-neutral reaction of CH₃ and O; Fockenberg & Preses 2002; Atkinson et al. 2006).

5.2. M4-M5 vs. Solar-Type Outer Disk Chemistry

5.2.1. Hydrocarbons and Hydrocyanides

C₂H and HCN are precursor molecules for more complex hydrocarbon and hydrocyanide chemistry. We note two findings that suggest similar connections between C₂H and HCN chemistry for our M4-M5 disks and for solar-type disks from the literature. First, radially resolved C₂H and HCN excitation temperatures and optical depths toward the bright and well-resolved disk J1100-7619, measured interior to the pebble disk edge (Figure 9), are roughly consistent with C₂H and HCN measurements for solar-type disks presented in Bergner

et al. (2019). Second, the C₂H 3–2 and HCN 3–2 fluxes for the M4-M5 disks appear to follow the same trend as the solar-type disks (Figure 6). These fluxes do not show any trends across stellar type with stellar mass (Figure 7). These results imply similar underlying physical/chemical processes for the M4-M5 disks and the solar-type disks, consistent with the predictions for brown dwarf disks relative to T Tauri disks from thermochemical modeling (Greenwood et al. 2017).

At the same time, we find evidence suggesting that C₂H production is enhanced relative to HCN production in the disks around our cooler M4-M5 stars, in comparison to disks around the warmer solar-type stars. Assuming that the C₂H and HCN emission are originating from similar layers beyond the pebble disk, we find that M4-M5 disk-averaged C₂H/HCN column density ratios are higher than the 84th percentile C₂H/HCN ratio for solar-type disks estimated by Bergner et al. (2019) (Figure 10). The C₂H 3–2 / HCN 3–2 flux ratios are also higher for the M4-M5 disks compared to the solar-type disks. These enhancements imply greater hydrocarbon production in the M4-M5 disks relative to the solar-type disks. This finding is consistent with previous infrared chemistry observations and models of the inner regions (< 10 AU) of low-mass M-star disks, brown dwarf disks, and more massive T Tauri disks. These previous studies found relatively high C₂H₂/HCN flux and column density ratios and more carbon-rich atmospheres in the disks around low-mass M-stars and brown dwarfs. They inferred that hydrocarbon chemistry in the innermost regions of disks around these low-mass stars is enhanced relative to the more massive T Tauri stars (Pascucci et al. 2009; Walsh et al. 2015; Pascucci et al. 2013).

We can only draw preliminary conclusions from our work, as our sample size is small and biased toward gas-rich M4-M5 disks. As an initial view into disk chemistry around M4-M5 stars, our results suggest that similar patterns of hydrocarbon and hydrocyanide chemistry may exist beyond the pebble disk edges around M4-M5 and solar-type stars. However, there is some mechanism(s) or process(es), such as the difference in radiation field, that appears to be producing more hydrocarbons in disks around the cooler M4-M5 stars. It is not clear if this mechanism(s) is the same as that driving the hydrocarbon enhancements previously discovered in the inner < 10 AU of disks around low-mass M-stars and brown dwarfs. More observations and models of low-mass M-star disk chemistry, especially those that explore chemistry beyond the pebble disk, will help us investigate these tentative conclusions.

5.2.2. Formaldehyde

H₂CO emission morphologies for the two M4-M5 disks J0432-1827 and J1100-7619 show central/off-center holes in H₂CO emission, as well as substantial rings in H₂CO emis-

sion at/beyond the pebble disk edge (Figure 11). In contrast, Pegues et al. (2020) found mostly centrally peaked H₂CO emission morphologies for their sample dominated by large solar-type disks (observed with a mean resolution of $0.59'' \pm 0.22''$), with H₂CO emission substructure that was significant but of lesser magnitude than the central emission peaks. It is possible that this apparently relatively enhanced production of H₂CO emission beyond the pebble disk edge for the M4-M5 disks is due to (1) a relatively large reservoir of CO ice for the M4-M5 disks, which are much colder than their solar-type disk counterparts, and/or (2) a relatively small region of the M4-M5 disks interior to the CO snowline, where H₂CO would be produced mainly through warm, efficient gas-phase pathways. Notably we only have two disks firmly detected in H₂CO, and so we need a larger sample of low-mass M-star disks to verify this tentative conclusion.

6. SUMMARY

We have conducted an ALMA survey of CO isotopologues and small organic molecules toward a sample of five M4-M5 disks. We summarize our key findings below:

1. We detect ¹²CO 2–1, ¹³CO 2–1, C¹⁸O 2–1, C₂H 3–2, and HCN 3–2 toward 5/5 disks. We detect H₂CO 3–2 toward 2/5 disks and tentatively detect it toward two other disks. We detect DCN 3–2 toward 1/5 disks and tentatively detect it toward all other disks (see Section 4.1).
2. The dust continuum emission toward all five disks in the sample is smooth at this resolution (0.12-0.29"). The ¹²CO 2–1, ¹³CO 2–1, and C¹⁸O 2–1 emission is centrally peaked across the sample, with substructure that may be due to significant cloud contamination, extended disk structure, and/or disk-envelope interactions for 3/5 disks. For the two well-resolved disks, HCN 3–2 emission is centrally peaked with suggestive substructure beyond the pebble disk edge, C₂H 3–2 and H₂CO 3–2 have central/off-center depressions or holes in emission and substructure/rings beyond the pebble disk, and DCN 3–2 is centrally peaked and compact (see Section 4.2).
3. The C₂H and HCN line fluxes are correlated for the M4-M5 disk sample, as has been seen previously for a sample consisting mostly of solar-type disks from the literature. There are no clear relationships between the molecular line flux ratios and stellar masses/luminosities for either the M4-M5 or solar-type disk samples (see Section 4.3).
4. Radially resolved flux ratios of (C₂H 3–2 / C¹⁸O 2–1) and (H₂CO 3–2 / C¹⁸O 2–1) toward the well-resolved disk J1100-7619 increase monotonically with distance.

(DCN 3–2 / HCN 3–2) and (HCN 3–2 / C¹⁸O 2–1) are roughly constant across the disk where sufficient signal-to-noise exists. (C₂H 3–2 / HCN 3–2) increases with radius across the pebble disk, and then is constant beyond the pebble disk edge (see Section 4.4.1).

5. Pixel-by-pixel fits of the C₂H and HCN hyperfine structure toward J1100-7619 reveal that C₂H excitation temperatures, optical depths, and column densities are ~ 10 -20K, ~ 1 -4, and $\sim (1-10) \times 10^{14} \text{ cm}^{-2}$, respectively, across the disk. HCN excitation temperatures and optical depths are from ~ 15 -25K and ~ 7 -15, respectively, interior to the pebble disk edge where sufficient signal-to-noise exists. HCN column densities in the same disk region range from $\sim (3-30) \times 10^{13} \text{ cm}^{-2}$ (see Section 4.4.2).
6. For typical assumptions on excitation and assuming similar disk layers of origin for the C₂H and HCN emission, disk-averaged column density values for the M4-M5 disk sample are $(5-10) \times 10^{13} \text{ cm}^{-2}$ for C₂H and $(4-12) \times 10^{12} \text{ cm}^{-2}$ for HCN. Disk-averaged C₂H/HCN column density ratios for the M4-M5 disk sample all exceed the 84th percentile estimated for a sample of solar-type disks from the literature. This is similar, and perhaps related to, the hydrocarbon enhancements observed in the inner (<10AU) regions of M-star disks by infrared surveys. The single disk-averaged DCN/HCN column density estimate toward J1100-7619 is higher than the solar-type disk estimates from the literature (see Section 4.5).
7. We find evidence that C₂H and HCN share similar physical/chemical driver(s) beyond the pebble disks of our M4-M5 disk sample, as has been theorized for solar-type disks, while their relative chemistry appears more distinct interior to the pebble disk edge. Similar radial substructure of the H₂CO and C₂H emission may point to a linked dependence on the UV photodesorption of CO ice beyond the pebble disk (see Sections 5.1 and 5.2).

We stress that our sample is biased toward bright, gas-rich M4-M5 disks, and that these findings serve as an *initial* window into >10AU disk chemistry for low-mass M-stars. Spatially resolved molecular line observations toward a larger sample of low-mass M-star disks would allow us to explore these patterns of disk chemistry over a more representative population of young, cool stars.

ACKNOWLEDGMENTS

Jamila Pegues gratefully acknowledges the support of the National Science Foundation (NSF) Graduate Research Fellowship through Grant Numbers DGE1144152 and DGE1745303, and Karin Öberg gratefully acknowledges the support of the Simons Foundation through a Simons Collaboration on the Origins of Life (SCOL) PI Grant (Number 321183). L. Ilseore Cleaves gratefully acknowledges support from the Davide and Lucille Packard Foundation and the Virginia Space Grant Consortium. Viviana V. Guzmán gratefully acknowledges support from FONDECYT Iniciación 11180904. Feng Long gratefully acknowledges support from the Smithsonian Institution as an SMA Fellow. Support for this work was also provided by NASA through the NASA Hubble Fellowship grants #HST-HF2-51429.001-A and #HST-HF2-51460.001-A awarded by the Space Telescope Science Institute, which is operated by the Association of Universities for Research in Astronomy, Inc., for NASA, under contract NAS5-26555.

This paper makes use of the following ALMA data: ADS/JAO.ALMA#2017.1.01107.S. ALMA is a partnership of ESO (representing its member states), NSF (USA) and

NINS (Japan), together with NRC (Canada), MOST and ASIAA (Taiwan), and KASI (Republic of Korea), in cooperation with the Republic of Chile. The Joint ALMA Observatory is operated by ESO, AUI/NRAO and NAOJ. The National Radio Astronomy Observatory is a facility of the National Science Foundation operated under cooperative agreement by Associated Universities, Inc.

This work has made use of data from the European Space Agency (ESA) mission *Gaia* (<https://www.cosmos.esa.int/gaia>), processed by the *Gaia* Data Processing and Analysis Consortium (DPAC, <https://www.cosmos.esa.int/web/gaia/dpac/consortium>). Funding for the DPAC has been provided by national institutions, in particular the institutions participating in the *Gaia* Multilateral Agreement.

All data reduction scripts and computer code used for this research were written in Python (version 2.7). All plots were generated using Python’s Matplotlib package (Hunter 2007). This research also made use of Astropy (<http://www.astropy.org>), a community-developed core Python package for Astronomy (Astropy Collaboration et al. 2013, 2018), as well as the NumPy (Oliphant 2006–) and SciPy (Jones et al. 2001–) Python packages.

APPENDIX

A. KEPLERIAN MASK PARAMETERS

Table 6 gives the Keplerian mask parameters used for the M4-M5 disk sample.

B. HYPERFINE CONSTRAINTS

B.1. Pixel-by-Pixel Hyperfine Fits

We estimate excitation temperatures, column densities, and optical depths for C₂H and HCN in the disk J1100-7619 using a pixel-by-pixel hyperfine fitting procedure (Section 3.2, Section 4.4.2). This procedure is based on the work of Bergner et al. (2019), which in turn was adapted from the fitting procedure of Estalella (2017) and the calculations of Mangum & Shirley (2015). By fitting to the spectrum through each pixel, we reduce line blending of the hyperfine components of the spectra, which allows for tighter constraints on the fit. We also avoid systematic errors due to changes in line width, line center, and line peak as a function of disk location.

The model assumes that the molecule is in local thermodynamic equilibrium (LTE), that the line width is the same for each hyperfine component, and that the excitation conditions are homogeneous along the line of sight within the given region. We fit the same model across both C₂H 3–2 and C₂H (N=3–2, J=5/2–3/2), because the additional emission from C₂H (N=3–2, J=5/2–3/2) further improves our model con-

straints for C₂H. Note that more hyperfine components exist for C₂H 3–2 beyond those listed in Table 2; however, those unlisted hyperfine components have very weak line intensities, and likely would not significantly affect our spectrum fits if we included them.

The hyperfine model contains four parameters: an amplitude (\hat{A}^*), a transformed optical depth for the main hyperfine component ($\hat{\tau}_m^*$), a line width ($\hat{\Delta}V_{\text{line}}$), and a central velocity reference point (\hat{V}_{LSR}). Note that we use the $\hat{}$ symbol to differentiate these model parameters from constants and other quantities in the equations. The amplitude and transformed optical depth parameters are directly related to the excitation temperature, column density, and total optical depth of the hyperfine line at that pixel.

We now write down the final equations used for this procedure. First, the spectrum model is in brightness temperature units and is a function of velocity. We denote this model as $\hat{H}\{V_k\}$, where we again use the $\hat{}$ symbol to differentiate between the model spectrum \hat{H} and the actual spectrum H later on.

$$\hat{H}\{V_k\} = \frac{\hat{A}^*}{\hat{\tau}_m^*} \left(1 - \exp(-\tau_k) \right), \quad (\text{B1})$$

where V_k is the central velocity of channel k . \hat{A}^* is the amplitude parameter (in brightness temperature units) and $\hat{\tau}_m^*$ is

Table 6. Keplerian Mask Parameters.

| Disk | $^{12}\text{CO } \theta_\alpha$ | $^{12}\text{CO } \theta_\beta$ | V_{LSR} | V_0 | R_0 | q | Mask Extent (") | | | | | | |
|------------|---------------------------------|--------------------------------|------------------------|------------------------|-------|-----|------------------|------------------|-------------------------|----------------------|--------------|--------------|-----------------------|
| | ($^\circ$) | ($^\circ$) | (km s^{-1}) | (km s^{-1}) | (AU) | | ^{12}CO | ^{13}CO | C^{18}O | C_2H | DCN | HCN | H_2CO |
| (1) | (2) | (3) | (4) | (5) | (6) | (7) | (8) | (9) | (10) | (11) | (12) | (13) | (14) |
| FP Tau | 213.3 | 46.7 | 8.32 | 0.25 | 100 | 0.3 | 1.24 | 0.68 | 0.56 | 1.44 | 0.12 | 1.20 | 0.36 |
| J0432+1827 | 157.5 | 42.9 | 5.60 | 0.25 | 100 | 0.3 | 2.16 | 1.32 | 1.32 | 1.32 | 0.48 | 1.36 | 1.48 |
| J1100-7619 | 108.8 | 20.9 | 4.75 | 0.22 | 100 | 0.3 | 2.04 | 1.92 | 1.36 | 1.48 | 0.72 | 1.64 | 2.12 |
| J1545-3417 | 264.2 | 53.1 | 4.50 ^[1] | 0.25 | 100 | 0.3 | 2.00 | 1.32 | 1.96 | 1.16 | 0.36 | 1.36 | 0.40 |
| Sz 69 | 167.2 | 20.5 | 5.30 ^[1] | 0.25 | 100 | 0.3 | 2.68 | 2.68 | 0.96 | 0.4 | 0.16 | 0.44 | 0.24 |

NOTE—All Keplerian masks were generated using [jpegues \(2019\)](#). The masks assume that the combined thermal and turbulent line width is defined by $\Delta V \sim V_0(R_0/100)^q$ ([Yen et al. 2016](#)). We estimated the geometric angle parameters, denoted here as θ_α and θ_β , using the masks, fixed broadening parameters, fixed systemic velocity (V_{LSR}), and a grid-search algorithm. θ_α and θ_β represent the position and inclination angles, respectively. We stress that these are *parameters*, not measurements, which were chosen purely to maximize the fit of the Keplerian masks. We use the unconventional α and β denotation here to avoid confusion with angles measured in other studies from dust or line emission. For J1545-3417 and Sz 69, systemic velocities are based on values and uncertainties available in the literature ([Yen et al. 2018](#)). For FP Tau, J0432+1827, and J1100-7619, the systemic velocities were selected based on inspection of the CO isotopologue emission. The Keplerian mask radii are the distances at which the radial emission profiles first reached zero. *References:* [1] [Yen et al. \(2018\)](#).

the transformed optical depth parameter (bounded such that $0 < \hat{\tau}_m^* < 1$). τ_k is the optical depth of this k^{th} channel, summed over all L hyperfine components:

$$\tau_k = \sum_i^L \frac{\tau_m (S_i \mu^2 / S_m \mu^2) G_i \{V_k\}}{\Delta V_{\text{chan}}}, \quad (\text{B2})$$

where τ_m is the optical depth of the main hyperfine component, calculated as:

$$\tau_m = \begin{cases} -\ln(1 - \hat{\tau}_m^*) & \text{if } \hat{\tau}_m^* > 0.01 \\ \hat{\tau}_m^* + \frac{(\hat{\tau}_m^*)^2}{2} + \frac{(\hat{\tau}_m^*)^3}{3} & \text{if } \hat{\tau}_m^* \leq 0.01, \end{cases} \quad (\text{B3})$$

and $(S_i \mu^2 / S_m \mu^2)$ is the strength of the i^{th} hyperfine component relative to the main hyperfine component (Table 2). ΔV_{chan} is the width of each velocity channel (identical across all channels). $G_i \{V_k\}$ is the value of the line profile for the i^{th} hyperfine component at velocity channel k , assumed to be:

$$G_i \{V_k\} = \Delta \hat{V}_{\text{line}} \sqrt{\frac{\pi}{16 \ln(2)}} \left(\text{erf}(x_{i,k}^+) - \text{erf}(x_{i,k}^-) \right), \quad (\text{B4})$$

where $\Delta \hat{V}_{\text{line}}$ is the line width parameter of the model, assumed to be the same for each hyperfine component, and $\text{erf}(z)$ represents the error function for input z . If $|x_{i,k}^+ - x_{i,k}^-| < 10^{-4}$, then $G_i \{V_k\}$ is instead approximated as:

$$G_i \{V_k\} \approx \frac{\Delta \hat{V}_{\text{line}}}{2\sqrt{\ln(2)}} \left(x_{i,k}^+ - x_{i,k}^- \right)$$

$$\times \exp \left(- \left(\frac{x_{i,k}^+ + x_{i,k}^-}{2} \right)^2 \right). \quad (\text{B5})$$

$x_{i,k}^+$ and $x_{i,k}^-$ are calculated as:

$$x_{i,k}^\pm = 2\sqrt{\ln(2)} \left(\frac{V_k \pm (\Delta V_{\text{chan}}/2) - \hat{V}_{\text{LSR}} - \Delta V_i}{\Delta \hat{V}_{\text{line}}} \right), \quad (\text{B6})$$

where \hat{V}_{LSR} is the reference point parameter of the model. ΔV_i is the shift in velocity between the i^{th} and main hyperfine components and can be calculated from the frequencies (Table 2).

We estimated the four parameters of the model (the amplitude parameter \hat{A}^* , the transformed optical depth parameter $\hat{\tau}_m^*$, the line width parameter $\Delta \hat{V}_{\text{line}}$, and the velocity reference parameter \hat{V}_{LSR}) per pixel in the image using the `EnsembleSampler` function from the `emcee` package ([Foreman-Mackey et al. 2013](#)). The log-likelihood function used for `emcee` included error in the resolved peaks (i.e., 3 peaks for HCN 3–2 and 4 peaks across C_2H 3–2 and C_2H 3–2) and error across all model values:

$$\ln \mathcal{L} = - \sum_k \left(\frac{H \{V_k\} - \hat{H} \{V_k\}}{\epsilon_{\text{chan}}} \right)^2 - (\epsilon_{\text{peak}} \times 100), \quad (\text{B7})$$

where $H \{V_k\}$ and $\hat{H} \{V_k\}$ are the actual and model spectra, respectively, at velocity channel k . ϵ_{chan} is the channel rms converted to brightness temperature. ϵ_{peak} is the summed relative error in the peaks of the resolved hyperfine components

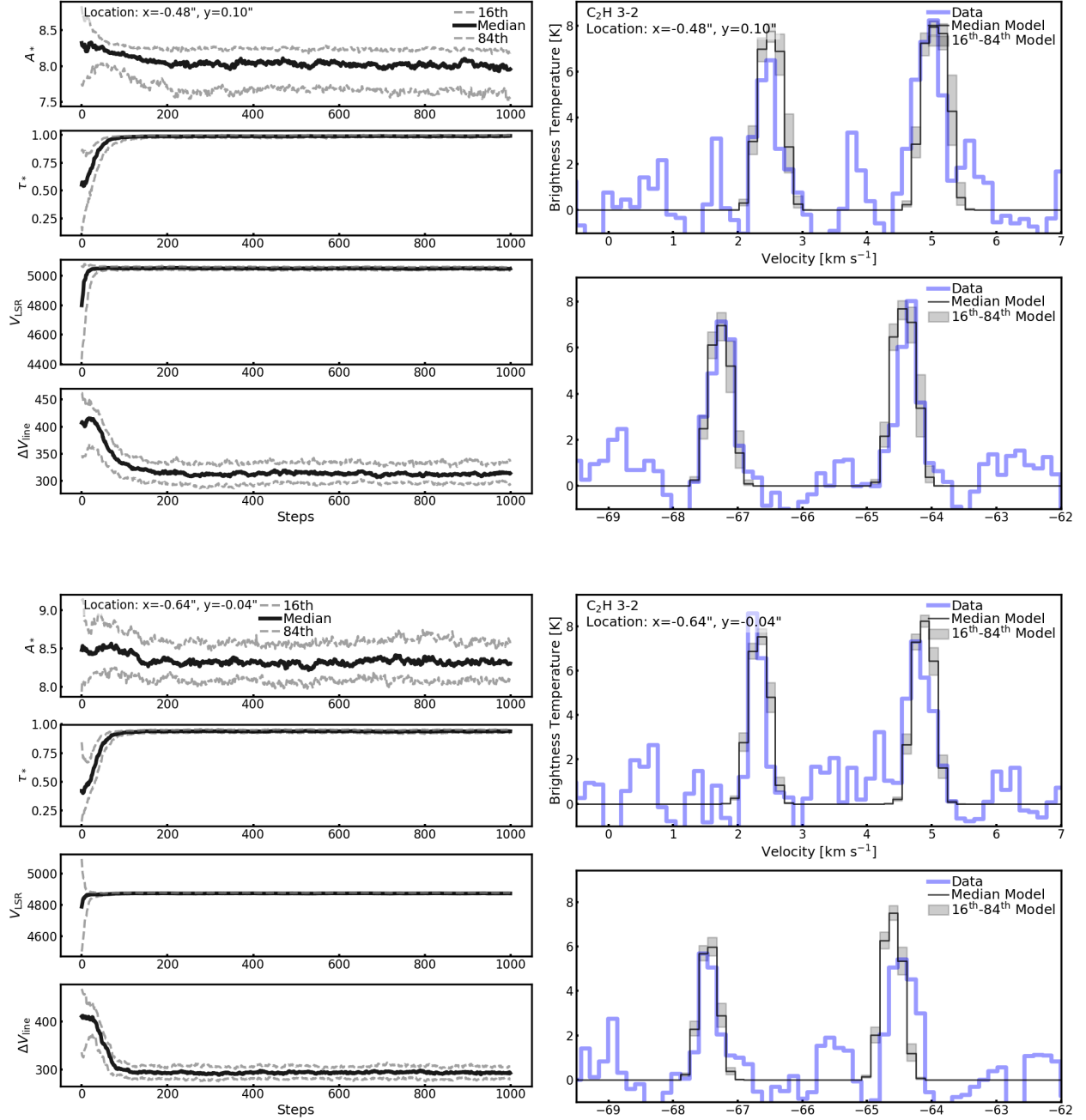


Figure 12. Example C_2H 3–2 and C_2H ($N=3-2$, $J=5/2-3/2$) hyperfine fits toward J1100-7619 within a specific pixel. The location of the pixel is given in arcsec along the top left of each panel. *Left:* The 16th percentile, median, and 84th percentile emcee chains for each of the four model parameters (from top row to bottom row, they are: \hat{A}^* , $\hat{\tau}^*$, \hat{V}_{LSR} , and $\hat{\Delta V}_{\text{line}}$). *Right:* The median and percentile hyperfine spectrum fits for C_2H 3–2 (top of each panel) and C_2H ($N=3-2$, $J=5/2-3/2$) (bottom of each panel).

(where ‘relative error’ is the absolute difference in the actual value and model value, divided by the actual value) and applies an additional penalty when the model and actual spectrum peaks are misaligned. The actual spectrum is converted from flux density units (i.e., units of [power per distance² per frequency]) to brightness temperature units using (e.g., Condon & Ransom 2016):

$$T = \left(\frac{\mathcal{F}c_0^2}{2k_B\nu_0^2\Omega_{\text{area}}} \right), \quad (\text{B8})$$

where \mathcal{F} is the flux density, c_0 is the speed of light, k_B is the Boltzmann constant, and ν_0 is the frequency of the main hyperfine component. Ω_{area} is the solid angle of the emitting area (in this case, the solid angle of the pixel). Note that in

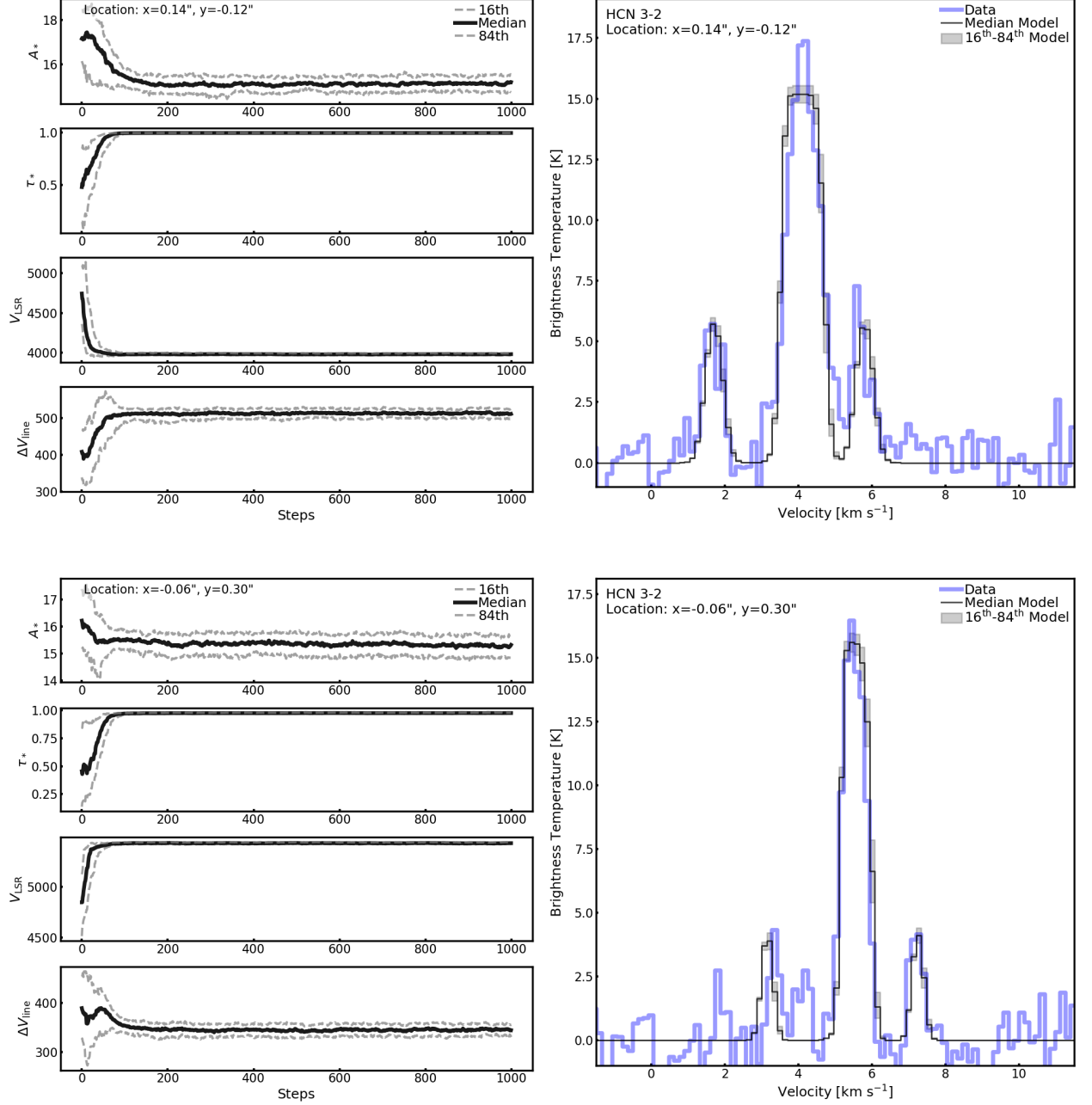


Figure 13. Example HCN 3–2 hyperfine fits toward J1100-7619 within a specific pixel. The location of the pixel is given in arcsec along the top left of each panel. *Left:* The 16th percentile, median, and 84th percentile `emcee` chains for each of the four model parameters (from top row to bottom row, they are: \hat{A}^* , $\hat{\tau}_*$, \hat{V}_{LSR} , and $\hat{\Delta V}_{\text{line}}$). *Right:* The median and percentile hyperfine spectrum fits.

practice, we calculate \mathcal{F} by converting our observed fluxes from units of Jy/beam, to Jy/pixel, and finally to ($\text{W m}^{-2} \text{Hz}^{-1}/\text{pixel}$), before applying Equation B8 in S.I. units.

We used 100 `emcee` walkers per pixel and walked them for 1000 steps. Initial estimates of each walker for \hat{A}^* , $\hat{\tau}_*$, $\hat{\Delta V}_{\text{line}}$, and \hat{V}_{LSR} were selected from Uniform distributions in the ranges of [peak of the emission in brightness temperature units $\pm 10\%$], (0, 1), [the disk’s systemic velocity $\pm 10\%$], and [300m s^{-1} , 500m s^{-1}], respectively. We disre-

garded the first 950 steps for each walker to account for the burn-in phase, creating a sampling distribution of 100×50 for each parameter. We took the median parameter of each sampling distribution, $\hat{A}^{*(50)}$, $\hat{\tau}_*^{(50)}$, $\hat{\Delta V}_{\text{line}}^{(50)}$, and $\hat{V}_{\text{LSR}}^{(50)}$, to be the final estimate of each pixel’s four parameters. We used the difference in the 16th and 84th percentile values relative to the median values as estimates of the lower and upper errors, respectively.

Figures 12 and 13 show example hyperfine emcee chains and fits for the C_2H and HCN molecular lines, respectively. The bottom panel of Figure 13 illustrates the importance of the HCN 3–2 satellite components discussed previously in anchoring the fit. This same panel also illustrates the intrinsic limitations of the underlying model at high optical depths. We discuss these limitations later in this section.

Adapting from Mangum & Shirley (2015), Estalella (2017) and Bergner et al. (2019), we estimate the excitation temperature T_{ex} from the following series of calculations:

$$\mathcal{T}_{\text{ex}} = \frac{\hat{A}^{*(50)}}{\hat{\tau}^{*(50)} f} + \mathcal{B}_{\text{cont}} \quad (\text{B9})$$

$$T_{\text{ex}} = \frac{h\nu_0}{k_{\text{B}} \ln(h\nu_0/(k_{\text{B}}\mathcal{T}_{\text{ex}}) + 1)}, \quad (\text{B10})$$

where Equation B9 determines the Planck-corrected excitation temperature from the model parameters, and Equation B10 calculates the excitation temperature in brightness temperature units from the Planck-corrected excitation temperature. We calculate $\mathcal{B}_{\text{cont}}$ from Equation B8, using the dust continuum flux at that pixel for \mathcal{F} (set to be a very small number if the continuum at that pixel is 0) and the solid angle of the pixel for Ω_{area} . h is the Planck constant, k_{B} is the Boltzmann constant, and f is the filling factor (assumed to be $f = 1$ for J1100-7619). Note that unlike the previous studies, we do not calculate the Planck-corrected temperature of the background continuum prior to Equation B9, as this is an over-correction of the background brightness temperature. The effect of this change is negligible at these wavelengths, continuum fluxes, and level of uncertainty.

We then estimate the total optical depth τ as:

$$\tau = -\frac{\ln(1 - \hat{\tau}^{*(50)})}{R_{\text{m}}}, \quad (\text{B11})$$

where R_{m} here is the strength of the *main* hyperfine transition relative to other same-level J transitions. R_i is generally calculated for any hyperfine transition as $R_i = \frac{(S_i\mu^2)}{\sum_{j_n=j_i}(S_n\mu^2)}$. As an example for a main hyperfine line, $R_{\text{m}} = 0.527$ for C_2H (N=3–2, J=7/2–5/2) is calculated from $\frac{2.2870}{2.2870+1.7110}$, which is the line intensities of the main line (N=3–2, J=7/2–5/2) divided by the sum of the line intensities for all other J=7/2–5/2 lines.

Finally, we calculate N_{tot} as (Mangum & Shirley 2015):

$$\begin{aligned} \bar{N}_{\text{tot}} = & \left(\frac{3hQ\{T_{\text{ex}}\}}{8\pi^3(S_{\text{m}}\mu^2)} \right) \left(\frac{\exp(E_{\text{u}}/T_{\text{ex}})}{\exp(h\nu_0/(k_{\text{B}}T_{\text{ex}})) - 1} \right) \\ & \times \left(\frac{\int_{\text{k}} \hat{H}_{\text{m}} dV}{\mathcal{T}_{\text{ex}} - \mathcal{B}_{\text{cont}}} \right) \left(\frac{\tau R_{\text{m}}}{(1 - \exp(-\tau R_{\text{m}}))} \right), \quad (\text{B12}) \end{aligned}$$

where $Q\{T_{\text{ex}}\}$ is the value of the partition function at temperature T_{ex} (taken from the CDMS database, Endres et al. 2016). $S_{\text{m}}\mu^2$ and E_{u} are the absolute line intensity and upper level energy, respectively, of the main hyperfine component (Table 2). Note that the column density equation in (Mangum & Shirley 2015) explicitly includes the upper degeneracy level g_{u} . For our calculations, that factor of degeneracy is already implicitly included in the CDMS values for $S\mu^2$ (Table 2). Finally, $\int_{\text{k}} \hat{H}_{\text{m}} dV$ is the integral of *only* the main hyperfine component of the model across all velocity channels. \hat{H}_{m} can be calculated by using Equation B2 for only $i = m$, and then plugging that result into Equation B1. Note that any i^{th} hyperfine component can be used in this way to determine N_{tot} ; we use the main hyperfine component here because it has the strongest emission.

B.2. Weighted Radial Profiles

To generate the weighted radial profiles of Figure 9, we first define $\sigma_{\text{pix},Q}^+ = \sqrt{(Q_{84} - Q_{50})^2 + (Q_{50} \times f_{50})^2}$ and $\sigma_{\text{pix},Q}^- = \sqrt{(Q_{16} - Q_{50})^2 + (Q_{50} \times f_{50})^2}$ as the upper and lower errors, respectively, for each pixel and each measurement. Here Q refers to the measured quantity (e.g., the excitation temperature) and the subscripts 16, 50, and 84 refer to the 16th, median, and 84th percentiles, respectively. f_{50} is the difference between the integrated fluxes of the median and actual spectrum, relative to the integrated flux of the actual spectrum.

we next extract all valid pixels within each deprojected annulus around the disk center. ‘‘Valid’’ pixels are those that fulfill all of the following three criteria: (1) The signal-to-noise of the faintest resolved hyperfine component is at least three (there are three total resolved components for HCN and four for C_2H). (2) The relative errors for all four parameters for this pixel ($\hat{A}^{*(50)}$, $\hat{\tau}^{*(50)}$, $\Delta\hat{V}_{\text{line}}^{(50)}$, and $\hat{V}_{\text{LSR}}^{(50)}$) are ≤ 0.20 . Here the relative error is the maximum over $[|P_{16} - P_{50}|/P_{50}, |P_{84} - P_{50}|/P_{50}]$, where P refers to each parameter. (3) $f_{50} \leq 0.20$.

We then perform a weighted average on the valid pixels within each annulus to produce the profiles of Figure 9. The weight per pixel and per measurement is $(1/\sigma^2)$, where $\sigma = \sqrt{(\sigma_{\text{pix},Q}^+)^2 + (\sigma_{\text{pix},Q}^-)^2}$. The upper and lower shaded error ranges for the measurements in Figure 9 are the rms across all $\sigma_{\text{pix},Q}^+$ and $\sigma_{\text{pix},Q}^-$, respectively, for each annulus.

B.3. Intrinsic Sources of Error

We note that the pixel-by-pixel hyperfine fits, and thus the weighted radial profiles, have significant intrinsic uncertainties. First, the C_2H and HCN pixel-by-pixel spectra toward J1100-7619 have relatively small line widths ($\sim 0.2\text{--}0.5\text{km s}^{-1}$) because of the disk’s low inclination angle. This fact, coupled with the relatively coarse velocity resolution of the data (0.14km s^{-1}), means that the hyperfine procedure has a

limited number of data points to fit for each hyperfine component. Second, the pixel-by-pixel fitting procedure does not account for uncertainties due to correlations between neighboring pixels. Third, the error in the fits is intrinsically large. This is particularly true for HCN, where the procedure is dependent on the fainter satellite hyperfine components as an 'anchor' for the overall fit. Finally, the underlying column density equation (Equation B12, Equation C13) makes Gaussian assumptions about the molecular line shape that break down as the optical depth increases. At the optical depths we are encountering for C₂H and HCN, uncertainties intrinsic to the model may become as large as ~40%. We thus stress that Figure 9 should be interpreted as rough constraints, rather than precise measurements, of the values, as should the column density estimates determined in Section 4.5.

C. COLUMN DENSITY ESTIMATES

C.1. Methodology

Assuming an excitation temperature T_{ex} and total optical depth τ for a hyperfine line, we can estimate the column density \bar{N}_{tot} , which is averaged over the disk region, using the total emission across all hyperfine components within that disk region. We use the column density equation adapted from Mangum & Shirley (2015), which presents \bar{N}_{tot} as measured from a specific i^{th} hyperfine emission component:

$$\bar{N}_{\text{tot}} = \left(\frac{3hQ\{T_{\text{ex}}\}}{8\pi^3(S_i\mu^2)} \right) \left(\frac{\exp(E_u/T_{\text{ex}})}{\exp(h\nu_i/(k_B T_{\text{ex}})) - 1} \right) \times \left(\frac{\int_k H_i dV}{T_{\text{ex}} - \mathcal{B}_{\text{cont}}} \right) \left(\frac{\tau R_i}{(1 - \exp(-\tau R_i))} \right), \quad (\text{C13})$$

where h is the Planck constant, k_B is the Boltzmann constant, and $Q\{T_{\text{ex}}\}$ is the value of the partition function at temperature T_{ex} (taken from the CDMS database, Endres et al. 2016). ν_i , $S_i\mu^2$, and E_u are the frequency, absolute line intensity, and upper level energy, respectively, of the i^{th} hyperfine component. R_i is the line intensity of the i^{th} component relative to the summed line intensities of all other same J-level transitions (the equation and an example calculation are in Appendix B). T_{ex} and $\mathcal{B}_{\text{cont}}$ are the Planck excitation temperature and continuum brightness temperature, respectively, calculated using the conversion procedures in Appendix B. Finally, $\int_k H_i dV$ is the integral across k velocity channels of *only* the i^{th} hyperfine component of emission in brightness temperature units. This quantity is converted from flux density units using the conversion procedure in Appendix B. Note that the column density equation in Mangum & Shirley (2015) explicitly includes a factor of the upper degeneracy level g_u . For our calculations, that factor of degeneracy is already included implicitly within the CDMS values for $S_i\mu^2$.

Since we are assuming an excitation temperature T_{ex} and total optical depth τ , Equation C13 reduces to the following:

$$\longrightarrow \bar{N}_{\text{tot}} = D_i\{T_{\text{ex}}, \tau\} \times \int_k H_i dV, \quad (\text{C14})$$

where $D_i\{T_{\text{ex}}, \tau\}$ is a term dependent on T_{ex} , τ , and the molecular line characteristics of *only* the i^{th} hyperfine component.

When the hyperfine components are blended, the quantity ($\int_k H_i dV$) is not known. We only know the total flux density integrated across all hyperfine components, which we convert to brightness temperature units ($\int_k H_{\text{tot}} dV$) using the brightness temperature conversion in Appendix B. Even so, we have enough information to set up a system of ($L+1$) equations with ($L+1$) unknowns:

$$\begin{aligned} \int_k H_{\text{tot}} dV &= \sum_{i=1}^L \int_k H_i dV, \\ \bar{N}_{\text{tot}} &= D_1\{T_{\text{ex}}, \tau\} \times \int_k H_1 dV, \\ \bar{N}_{\text{tot}} &= D_2\{T_{\text{ex}}, \tau\} \times \int_k H_2 dV, \\ &\vdots \\ \bar{N}_{\text{tot}} &= D_L\{T_{\text{ex}}, \tau\} \times \int_k H_L dV, \end{aligned} \quad (\text{C15})$$

where L is the total number of hyperfine components for this hyperfine line (i.e., $L=2$ for C₂H (N=3-2, J=7/2-5/2), $L=2$ for C₂H (N=3-2, J=5/2-3/2), and $L=6$ for HCN 3-2). Note that while we combined the C₂H (N=3-2, J=7/2-5/2) and C₂H (N=3-2, J=5/2-3/2) hyperfine spectra in Section 3.2 and Appendix B, we treat the lines separately for this general analysis and use the C₂H (N=3-2, J=5/2-3/2) line to check consistency with the C₂H (N=3-2, J=7/2-5/2) results.

The unknowns of this system of equations are ($\int_k H_i dV$) for each i^{th} hyperfine component and \bar{N}_{tot} . The latter equations can be subtracted from each other to eliminate \bar{N}_{tot} ; e.g. ($D_i\{T_{\text{ex}}, \tau\} \times \int_k H_i dV$) - ($D_j\{T_{\text{ex}}, \tau\} \times \int_k H_j dV$) = 0 for hyperfine components i and j . These equations can then be written in the form of $\mathbf{M}\mathbf{x} = \mathbf{b}$, where \mathbf{M} is the matrix (dimensions $L \times L$) of known coefficients:

$$\mathbf{M} = \begin{bmatrix} 1 & 1 & 1 & 1 & \dots & 1 & 1 \\ D_1 & -D_2 & 0 & 0 & \dots & 0 & 0 \\ 0 & D_2 & -D_3 & 0 & \dots & 0 & 0 \\ 0 & 0 & D_3 & -D_4 & \dots & 0 & 0 \\ \dots & \dots & \dots & \dots & \ddots & \vdots & \vdots \\ 0 & 0 & 0 & \dots & 0 & D_{L-1} & -D_L \end{bmatrix},$$

(where we have temporarily dropped the explicit $\{T_{\text{ex}}, \tau\}$ notation simply to reduce the width of the matrix text). \mathbf{x} is the vector (dimensions $L \times 1$) of unknown flux components:

$$\mathbf{x} = \begin{bmatrix} \int_k H_1 dV \\ \int_k H_2 dV \\ \vdots \\ \int_k H_L dV \end{bmatrix},$$

and \mathbf{b} is the vector (dimensions $L \times 1$) of equation solutions (which are mostly 0):

$$\mathbf{b} = \begin{bmatrix} \int_k H_{\text{tot}} dV \\ 0 \\ \vdots \\ 0 \end{bmatrix}.$$

We calculate \mathbf{M} and \mathbf{b} , and then we use standard linear algebra practices to solve for \mathbf{x} (e.g., `numpy.linalg.solve` function in Python). We then plug one of the solved hyperfine flux components from \mathbf{x} (e.g., the main hyperfine flux component) back into Equation C14 to recover $\overline{N}_{\text{tot}}$.

C.2. Literature Sample

We now describe the literature samples used to determine the 16th, median, and 84th percentiles of C₂H/HCN and DCN/HCN (Huang et al. 2017; Bergner et al. 2020) in Figure 10.

There were a total of seven disks with ALMA detections of both C₂H 3–2 and HCN 3–2 emission presented in Bergner et al. (2020). When estimating the disk-averaged column densities, Bergner et al. (2020) assumed optical depths for C₂H and HCN of ~ 1.1 and ~ 5.8 , respectively, and an excitation temperature of 30K. The 16th, median, and 84th percentiles of these estimates (2.4, 2.6, 4.7) are used in the C₂H/HCN panel of Figure 10.

There were a total of five disks with ALMA observations of the optically thin lines DCN 3–2 and H¹³CN (J=3–2), and one disk with ALMA observations of DCN 3–2 and HCN 3–2 (assumed to be optically thin within the emitting area), presented in Huang et al. (2017). These observations were used to estimate the DCN/HCN abundance ratios for all six disks as proxies for the overall D/H ratios. There were also DCN/HCN column density ratios for three additional disks presented in Bergner et al. (2020). Huang et al. (2017) considered excitation temperatures of 15K and 75K, while Bergner et al. (2020) assumed 30K. Here we use the 16th, median, and 84th percentiles across the combined 15K and 30K estimates (0.011, 0.018, 0.042) in the DCN/HCN panel of Figure 10. The column density ratios are insensitive to temperature changes at these excitation temperatures (Huang et al. 2017; Bergner et al. 2020).

D. CHANNEL MAPS

Channel maps of detected/tentatively detected emission toward FP Tau, J0432+1827, J1100-7619, J1545-3417, and Sz 69 are provided in the following sections.

D.1. Channel Maps for FP Tau

Figures 14 through 20 display channel maps of detected/tentatively detected emission toward FP Tau.

D.2. Channel Maps for J0432+1827

Figures 21 through 27 display channel maps of detected/tentatively detected emission toward J0432+1827.

D.3. Channel Maps for J1100-7619

Figures 28 through 34 display channel maps of detected/tentatively detected emission toward J1100-7619.

D.4. Channel Maps for J1545-3417

Figures 35 through 40 display channel maps of detected/tentatively detected emission toward J1545-3417.

D.5. Channel Maps for Sz 69

Figures 41 through 47 display channel maps of detected/tentatively detected emission toward Sz 69.

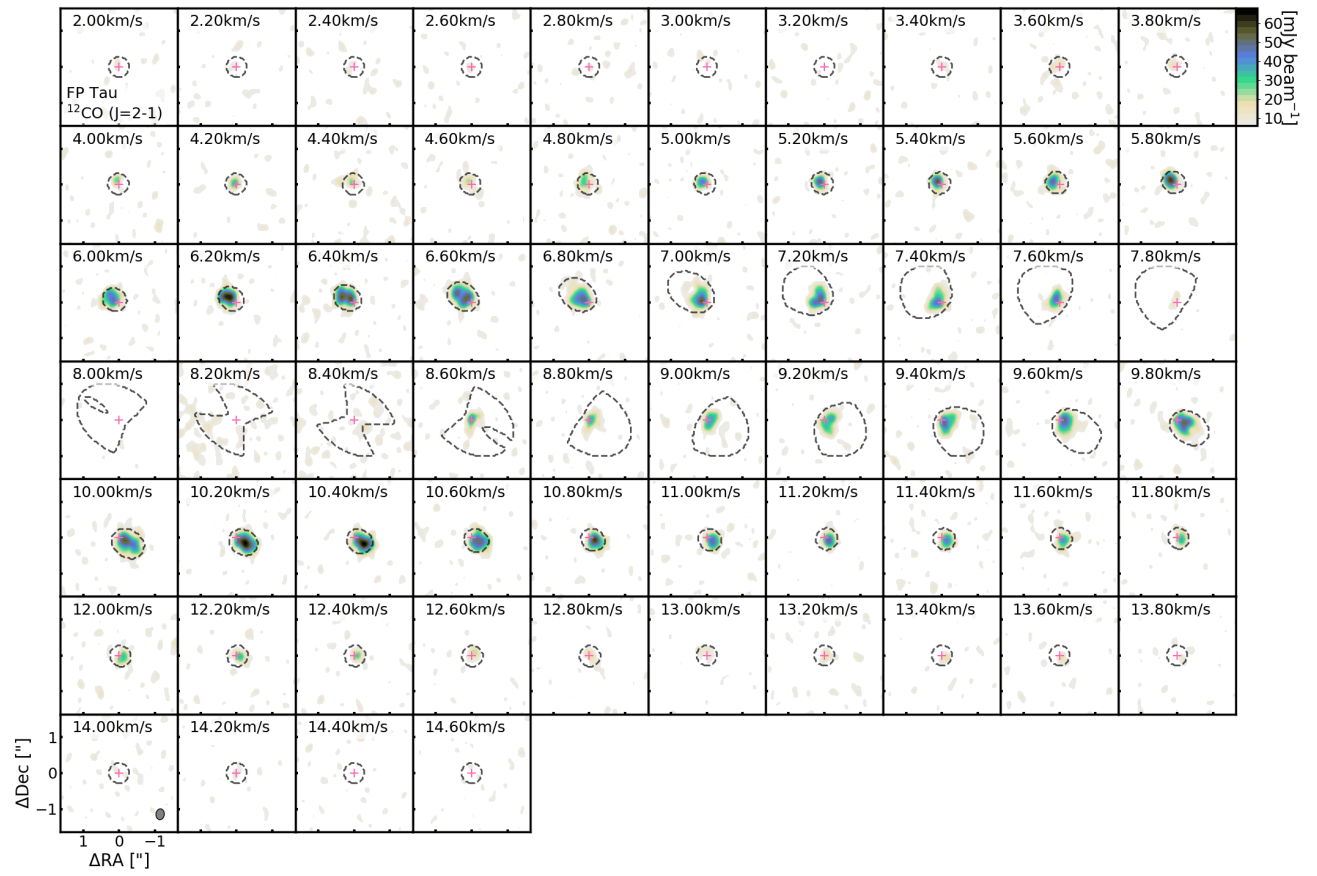


Figure 14. ^{12}CO toward FP Tau above 2σ .

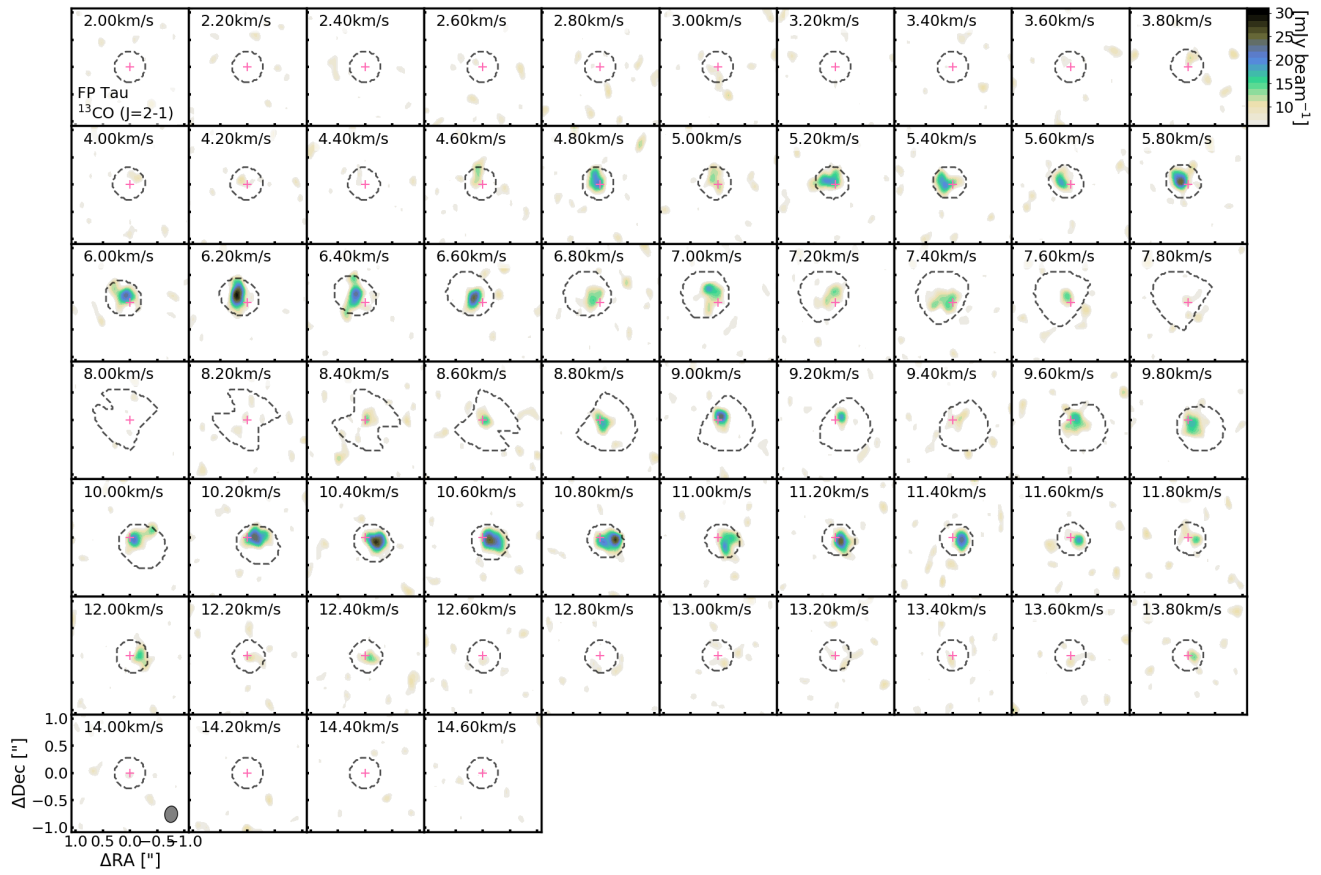


Figure 15. ^{13}CO toward FP Tau above 2σ .

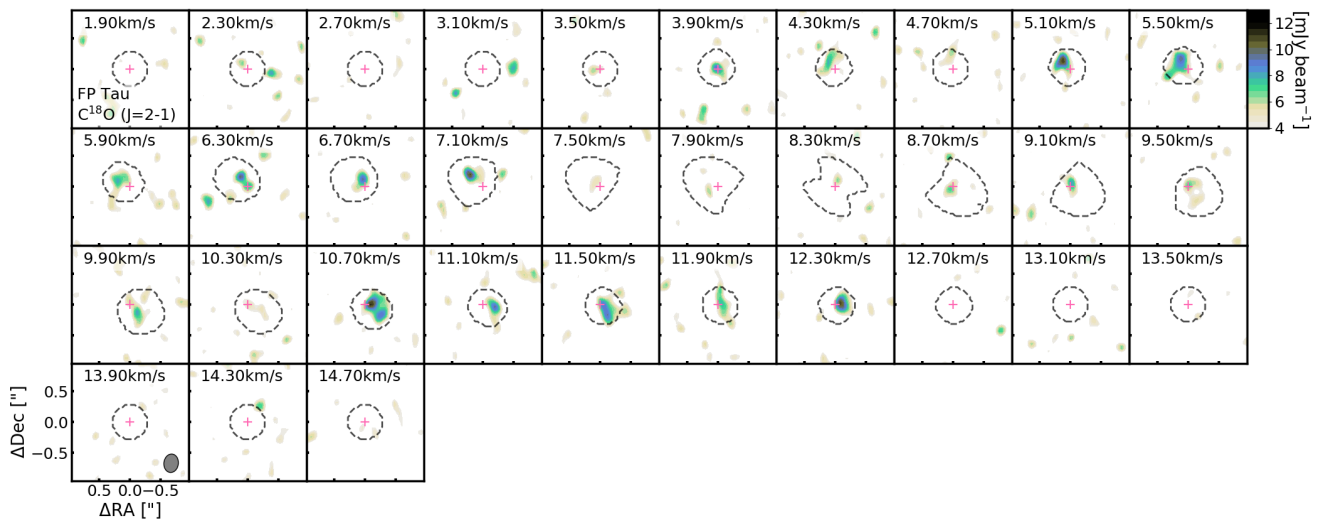


Figure 16. C^{18}O toward FP Tau above 2σ .

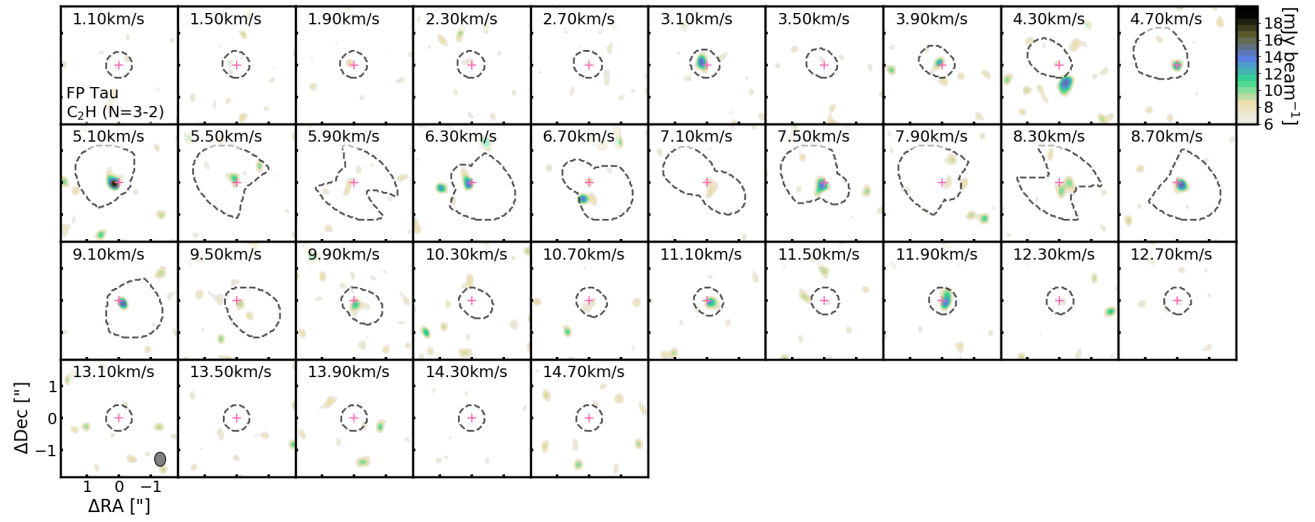


Figure 17. C_2H 3–2 toward FP Tau above 2σ .

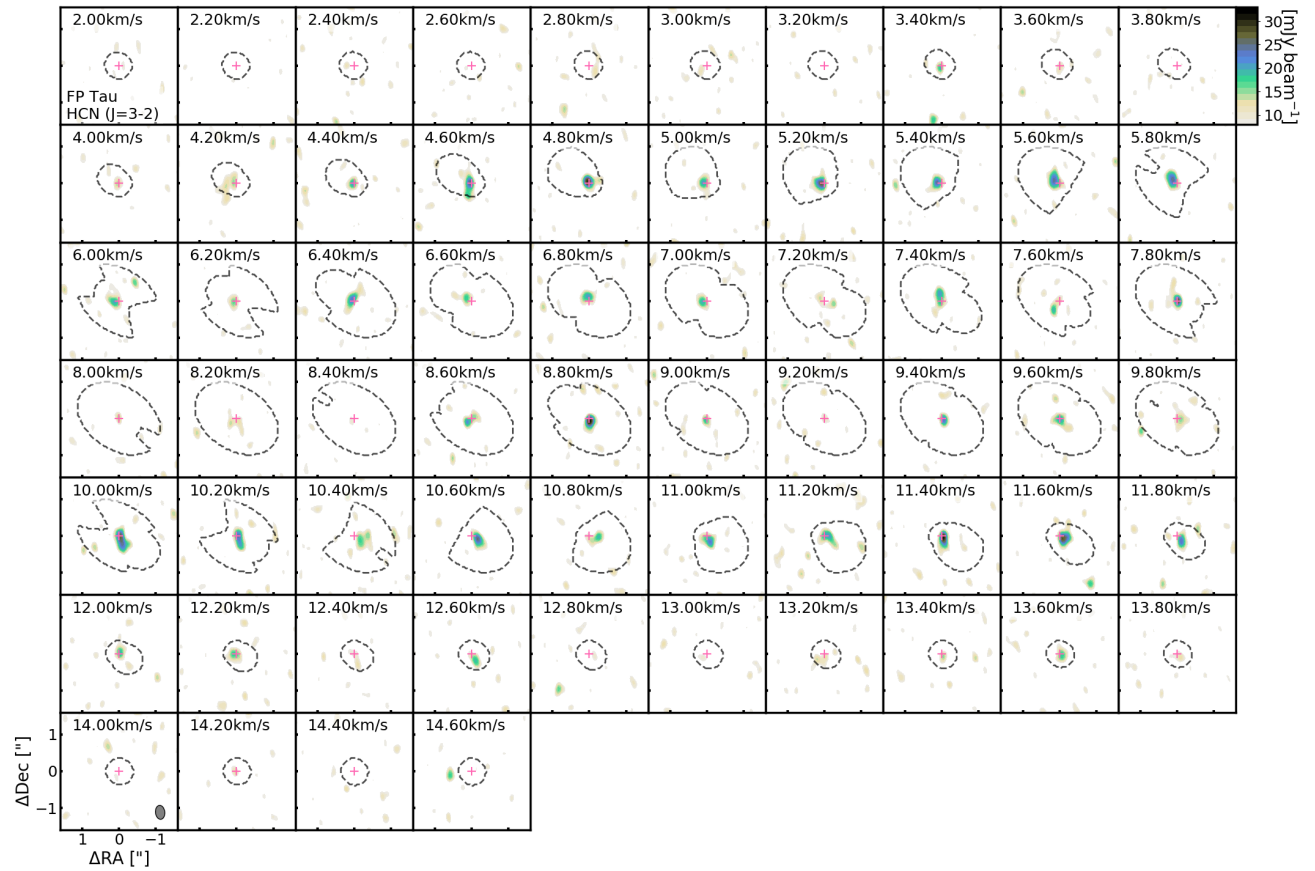


Figure 18. HCN 3–2 toward FP Tau above 2σ .

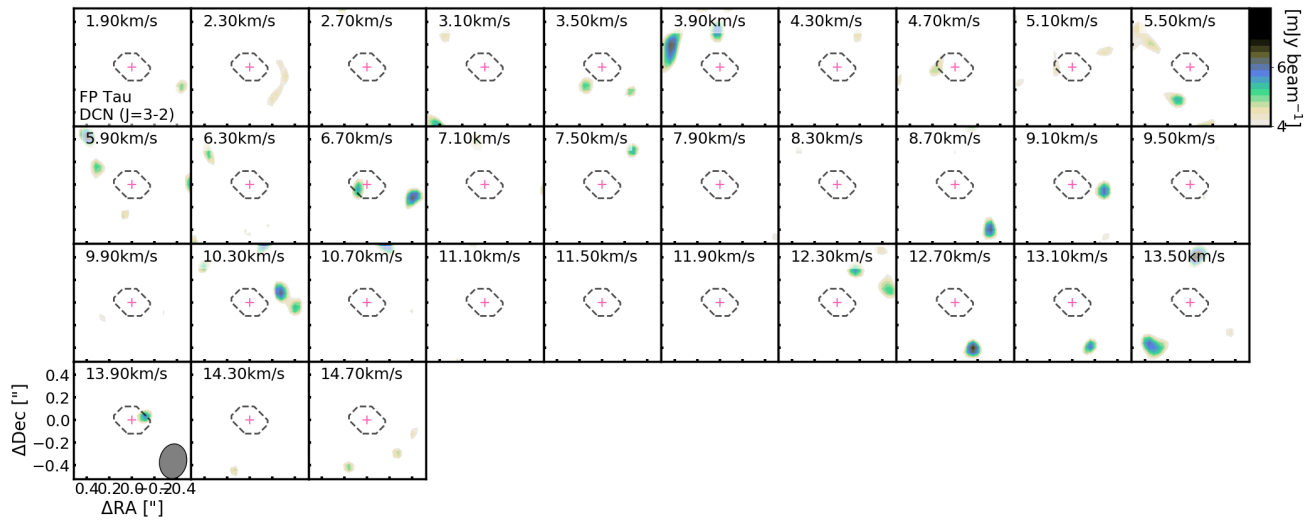


Figure 19. DCN 3–2 toward FP Tau above 2σ .

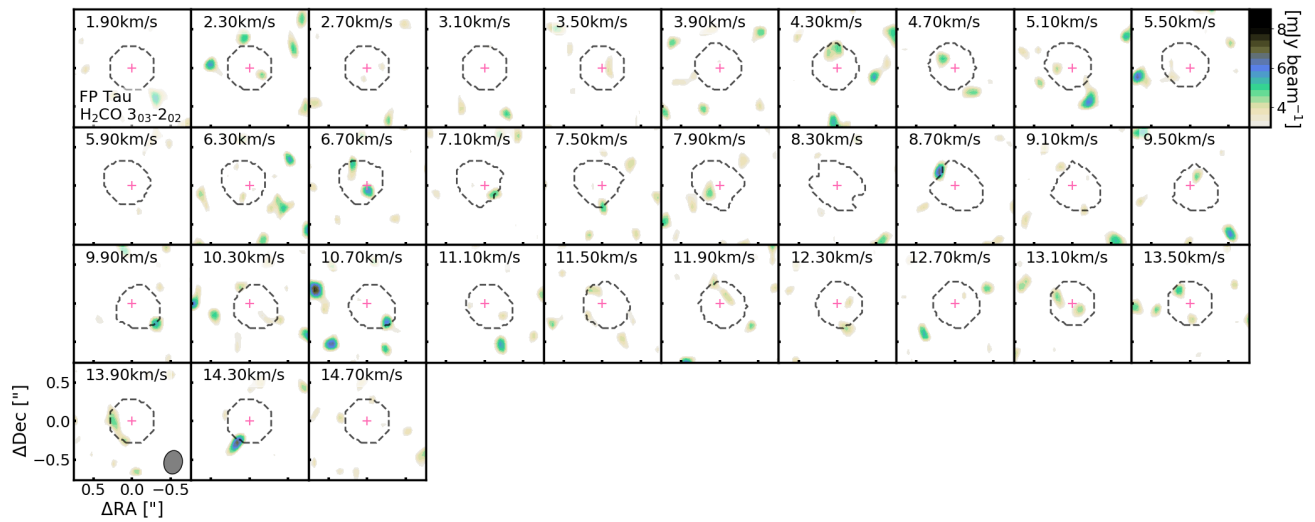


Figure 20. H_2CO 3–2 toward FP Tau above 2σ .

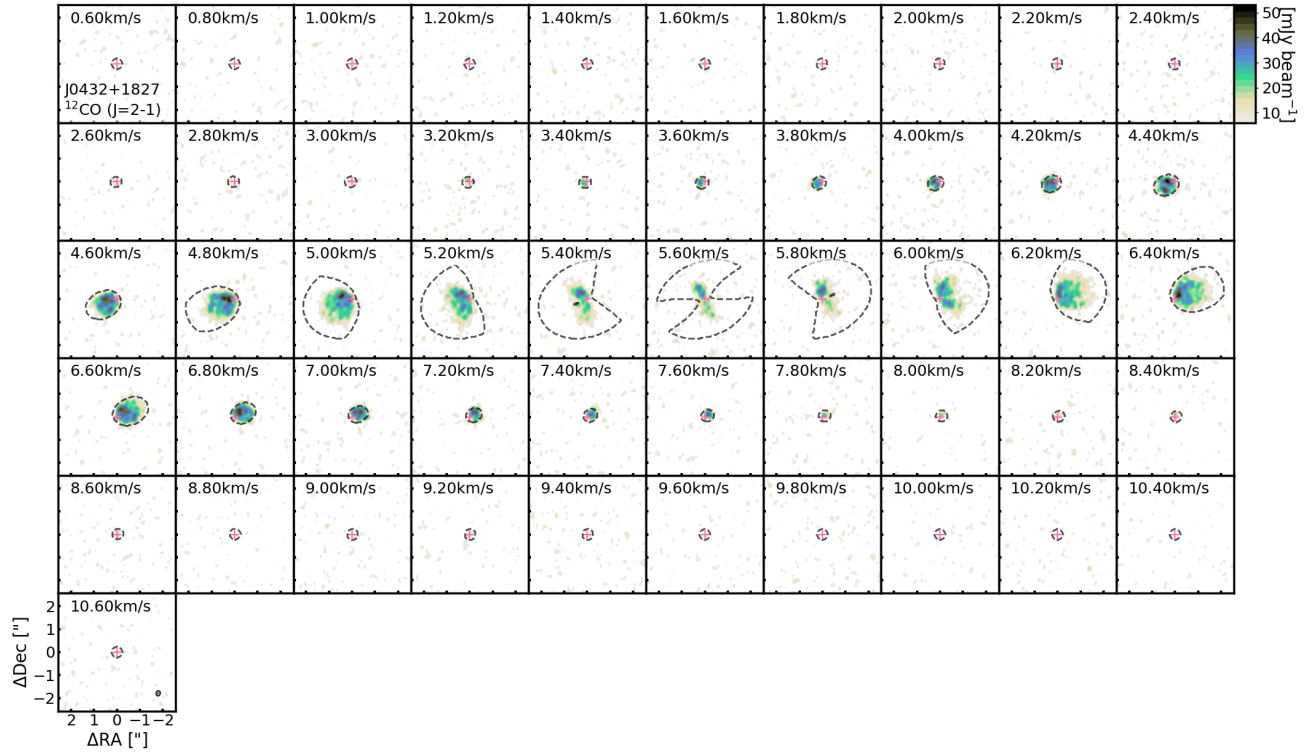


Figure 21. ^{12}CO toward J0432+1827 above 2σ .

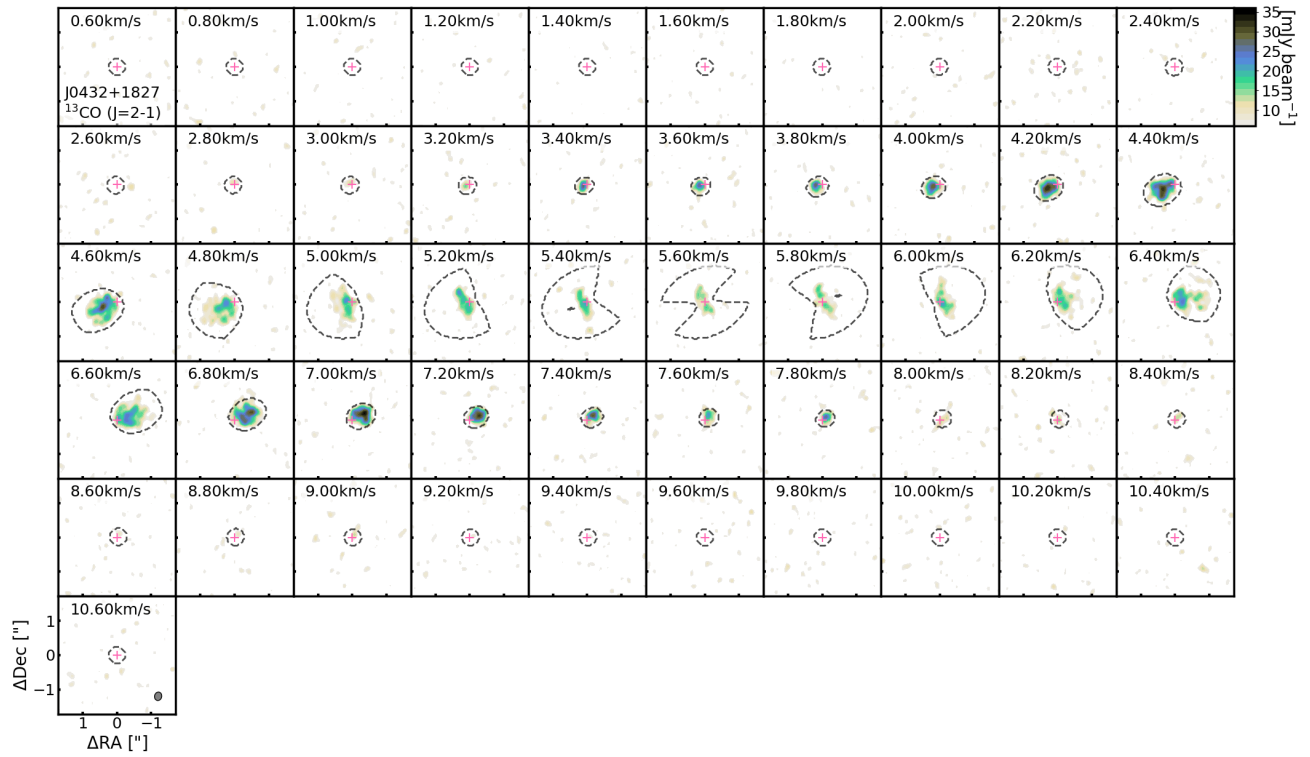


Figure 22. ^{13}CO toward J0432+1827 above 2σ .

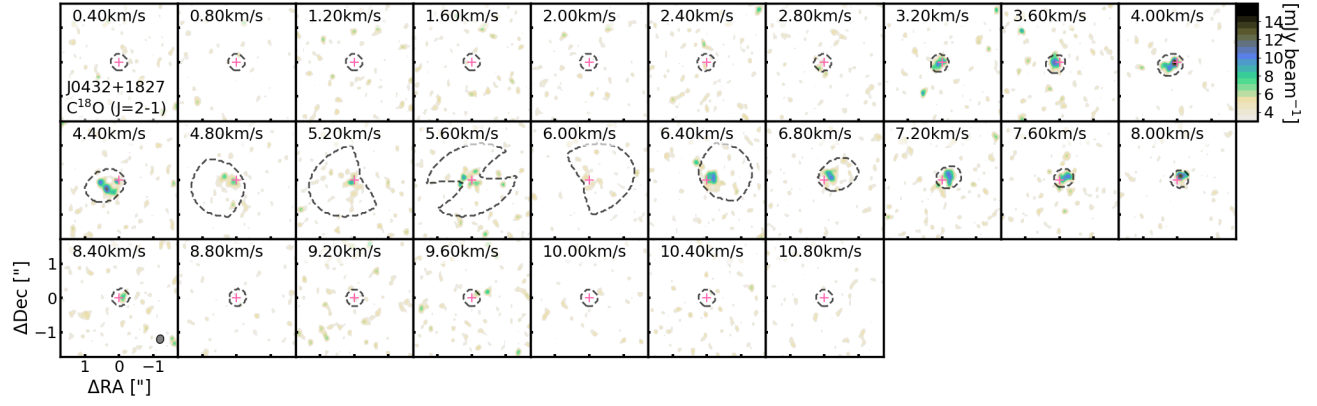


Figure 23. $C^{18}O$ toward J0432+1827 above 2σ .

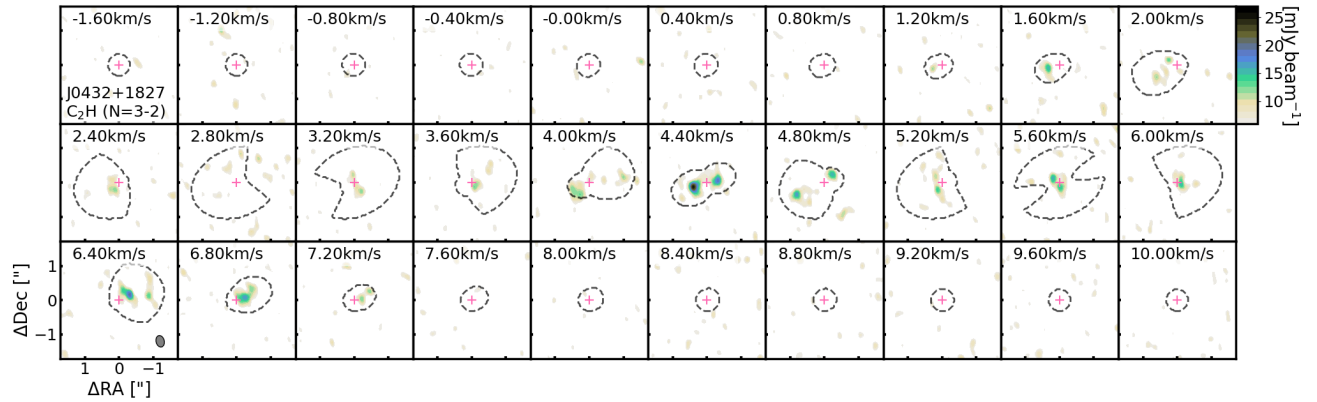


Figure 24. C_2H 3-2 toward J0432+1827 above 2σ .

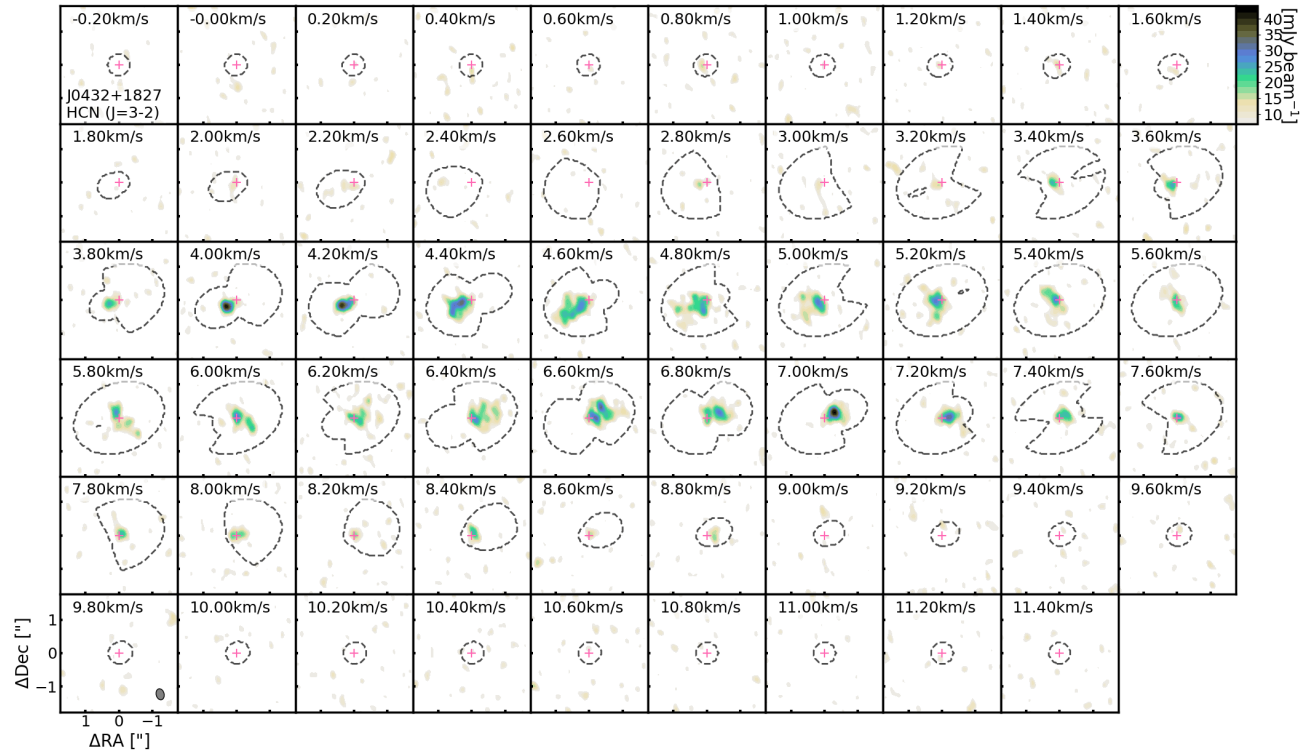


Figure 25. HCN 3–2 toward J0432+1827 above 2σ .

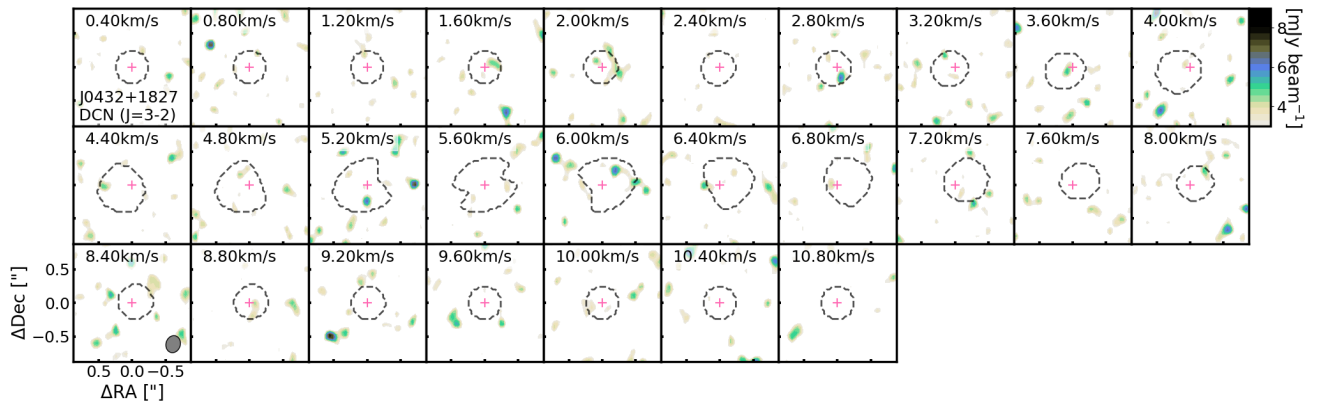


Figure 26. DCN 3–2 toward J0432+1827 above 2σ .

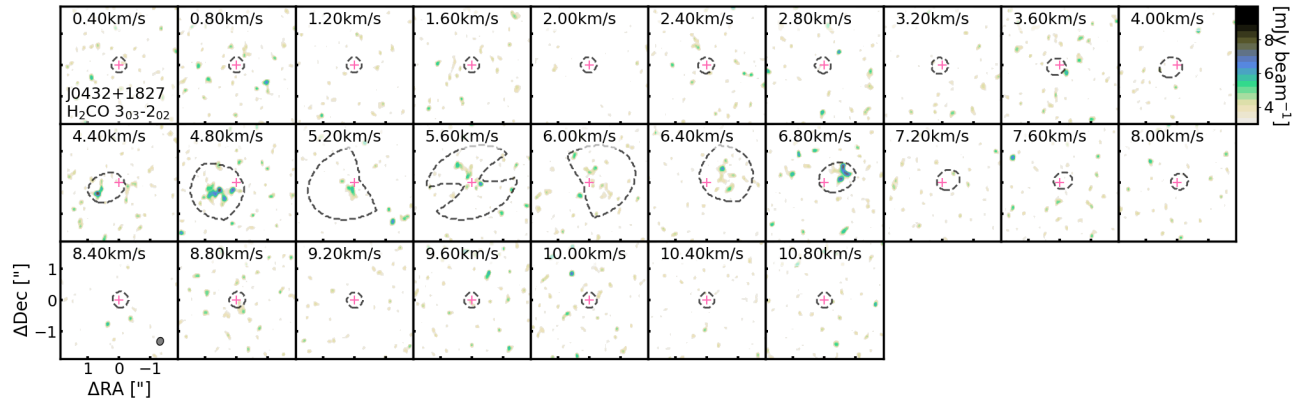


Figure 27. $\text{H}_2\text{CO } 3-2$ toward J0432+1827 above 2σ .

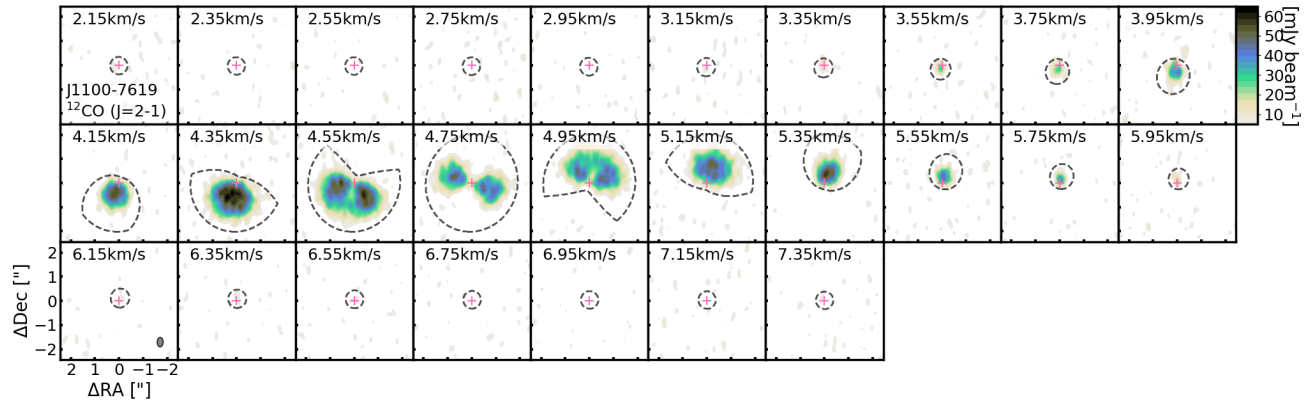


Figure 28. ^{12}CO toward J1100-7619 above 2σ .

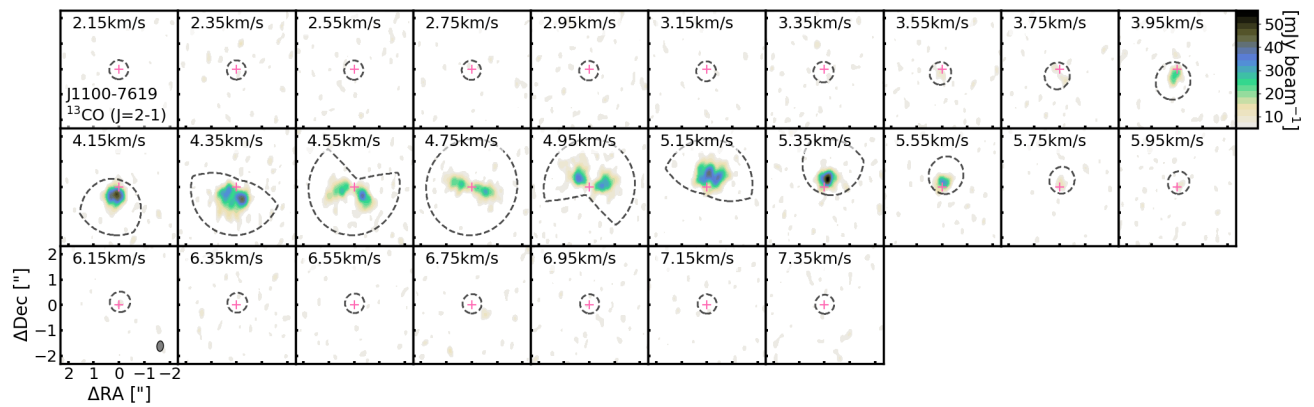


Figure 29. ^{13}CO toward J1100-7619 above 2σ .

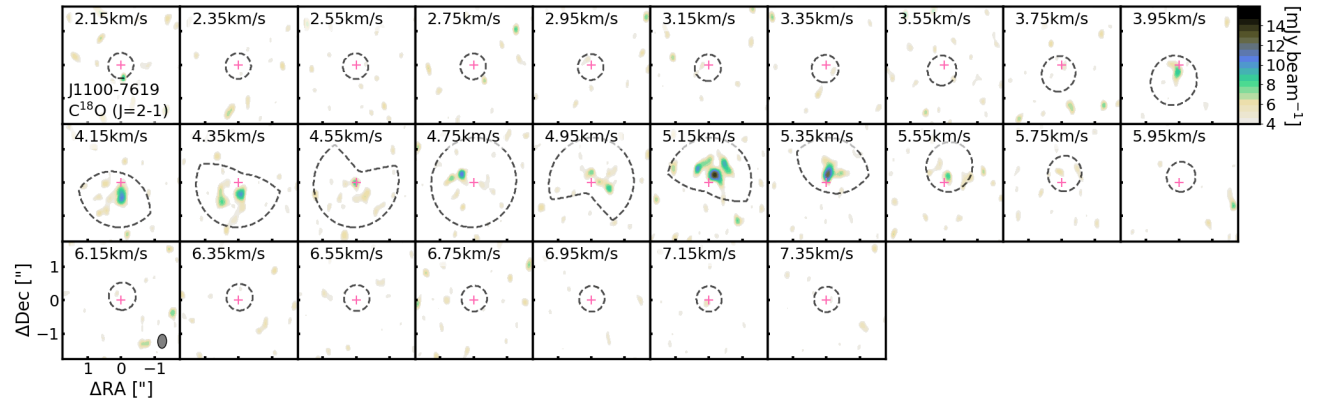


Figure 30. $C^{18}O$ toward J1100-7619 above 2σ .

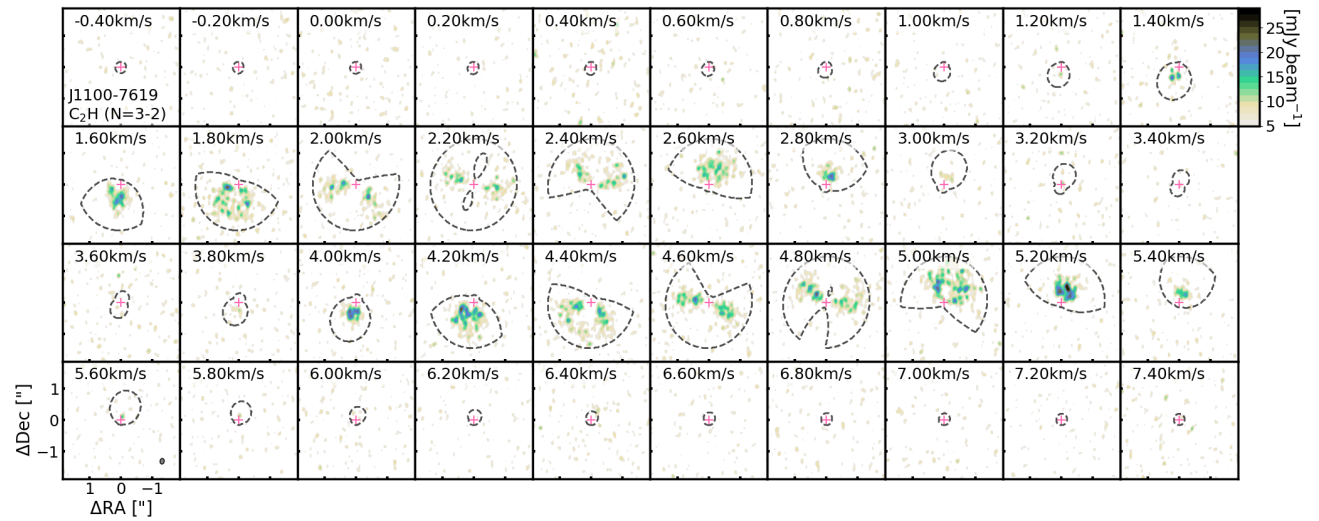


Figure 31. C_2H 3-2 toward J1100-7619 above 2σ .

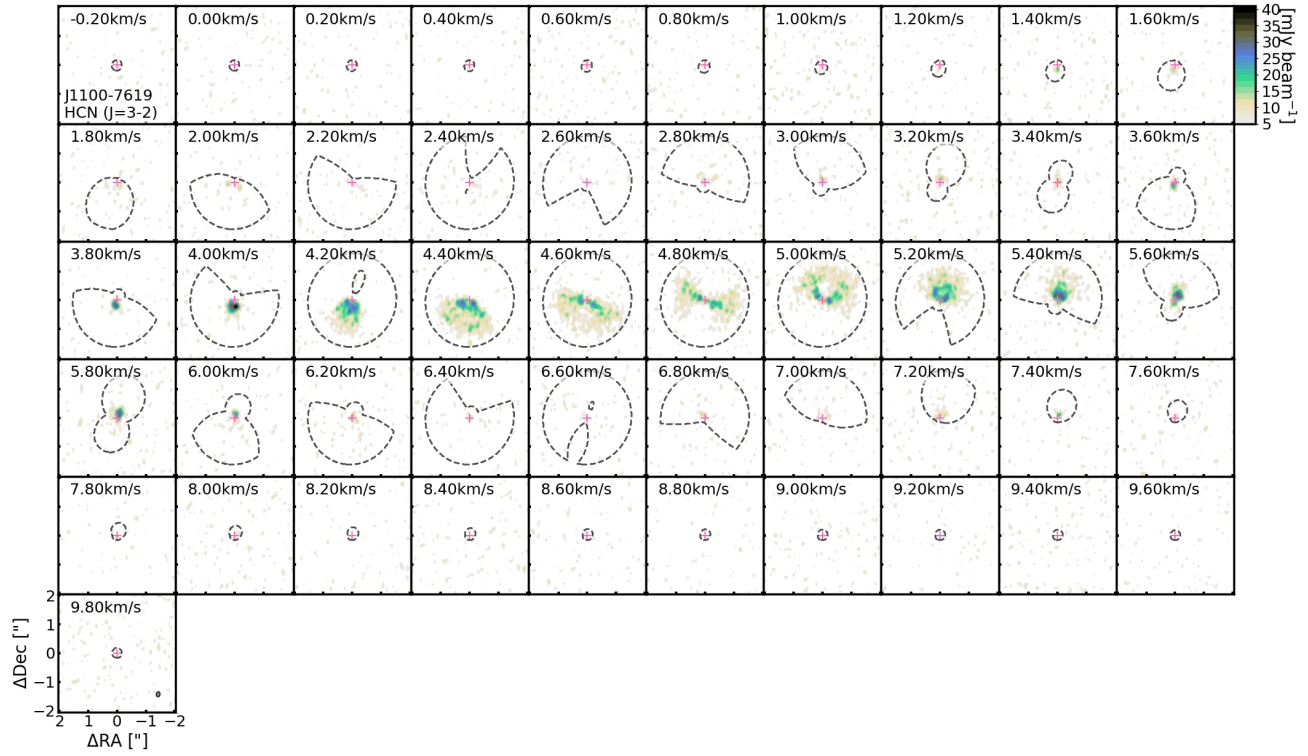


Figure 32. HCN 3–2 toward J1100-7619 above 2σ .

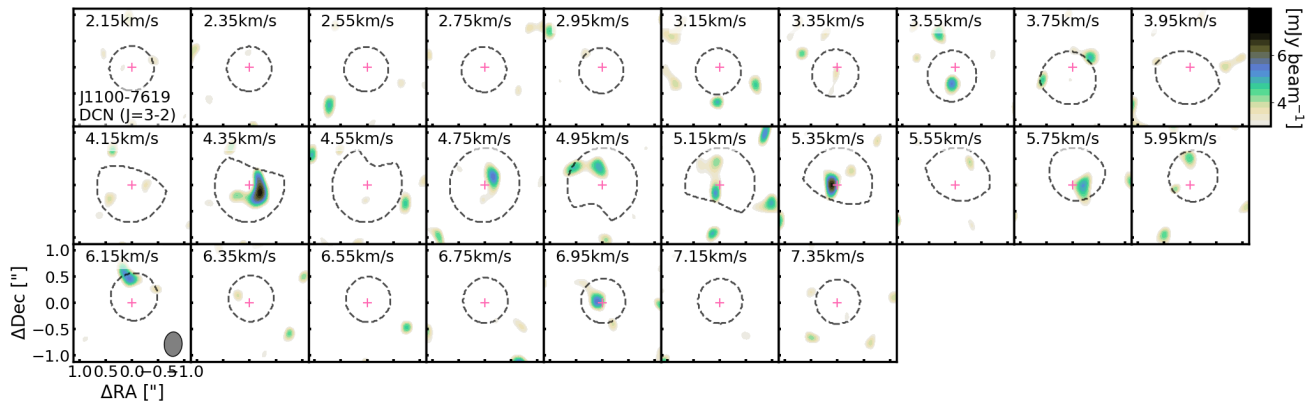


Figure 33. DCN 3–2 toward J1100-7619 above 2σ .

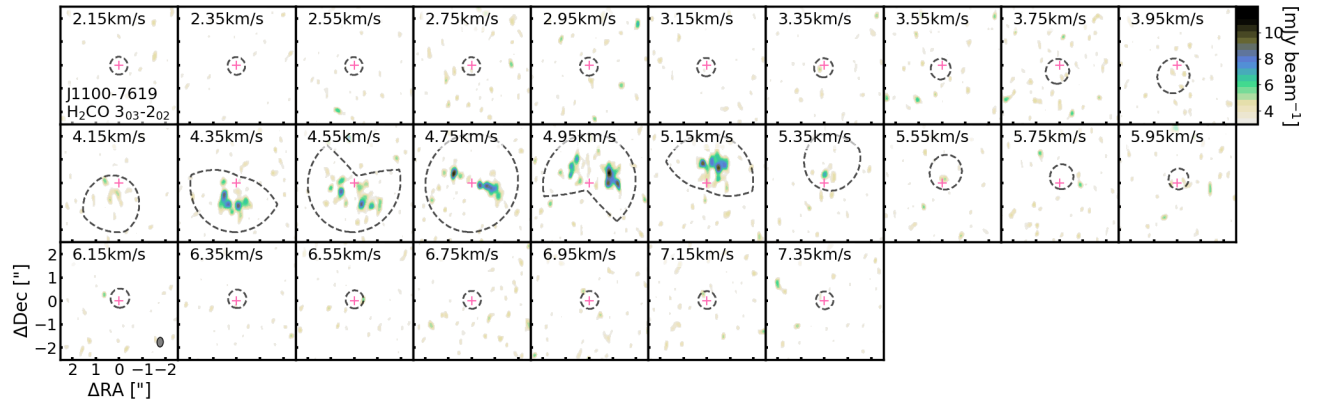


Figure 34. $\text{H}_2\text{CO } 3-2$ toward J1100-7619 above 2σ .

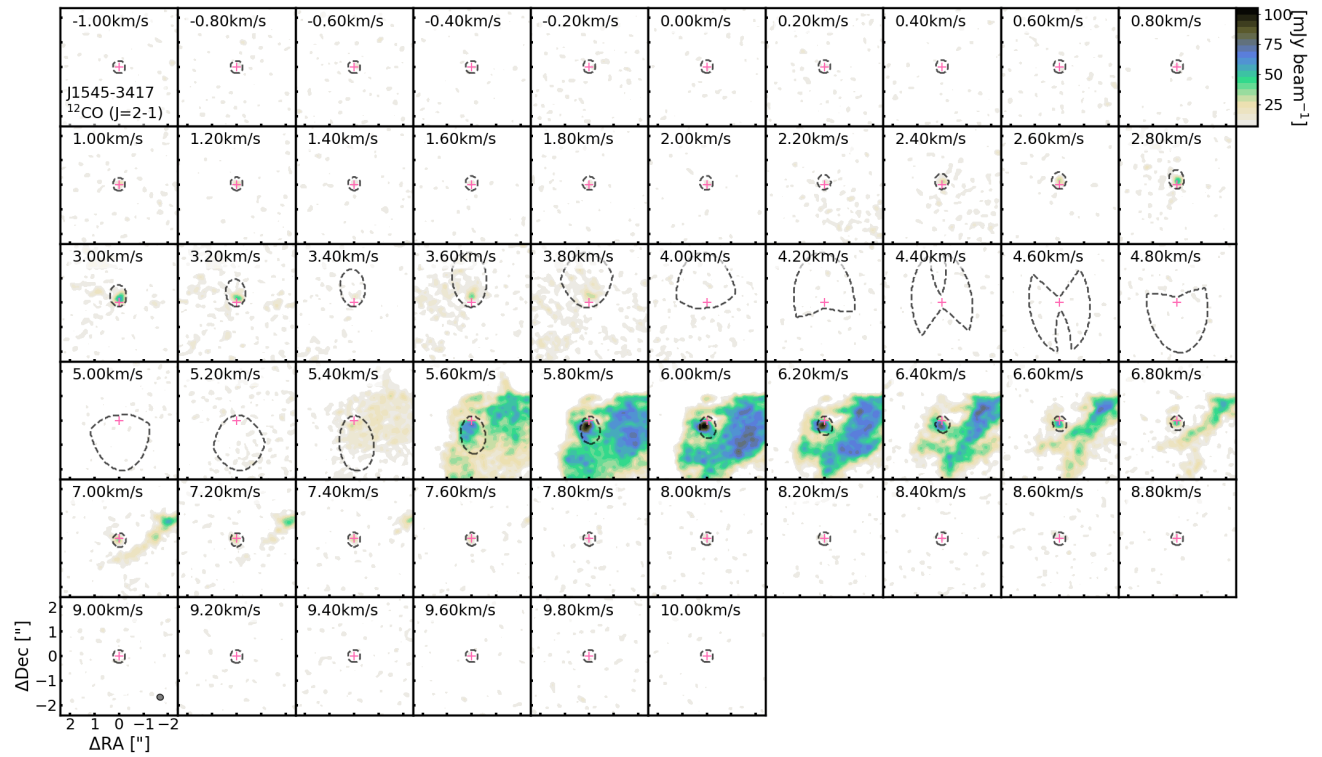


Figure 35. ^{12}CO toward J1545-3417 above 2σ .

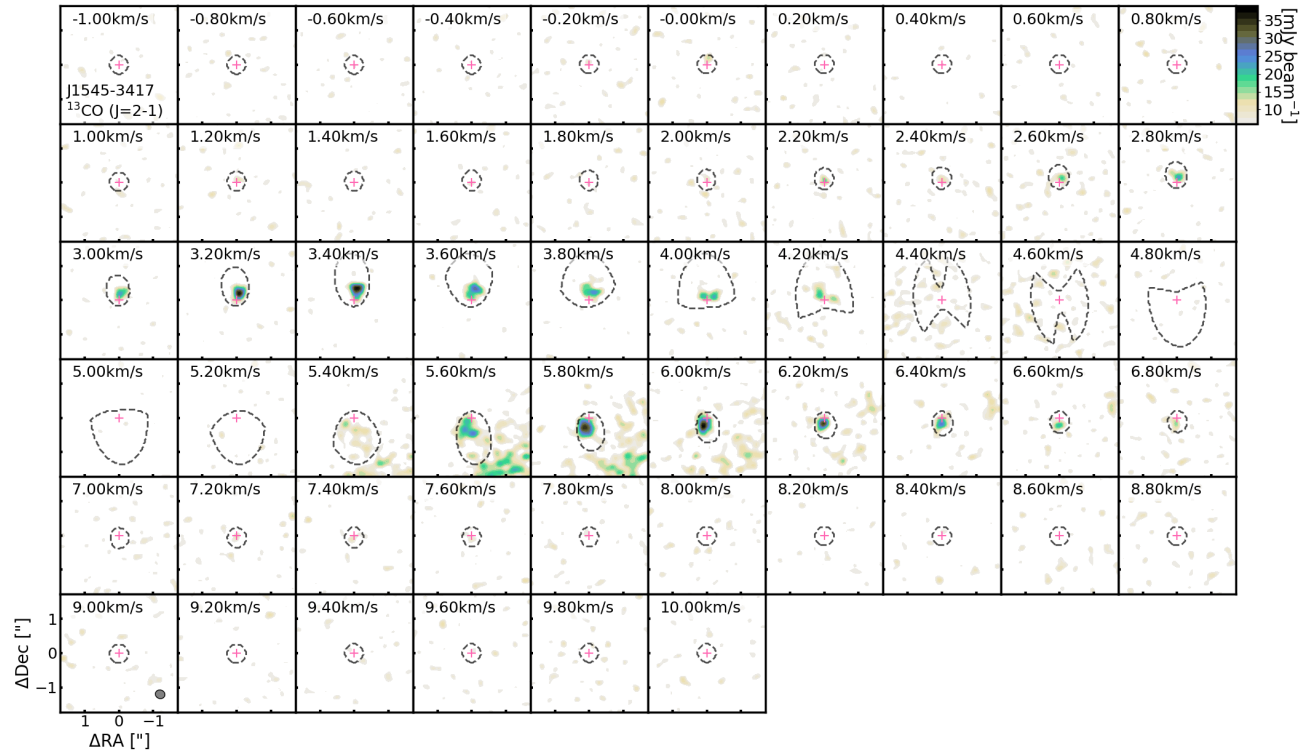


Figure 36. ^{13}CO toward J1545-3417 above 2σ .

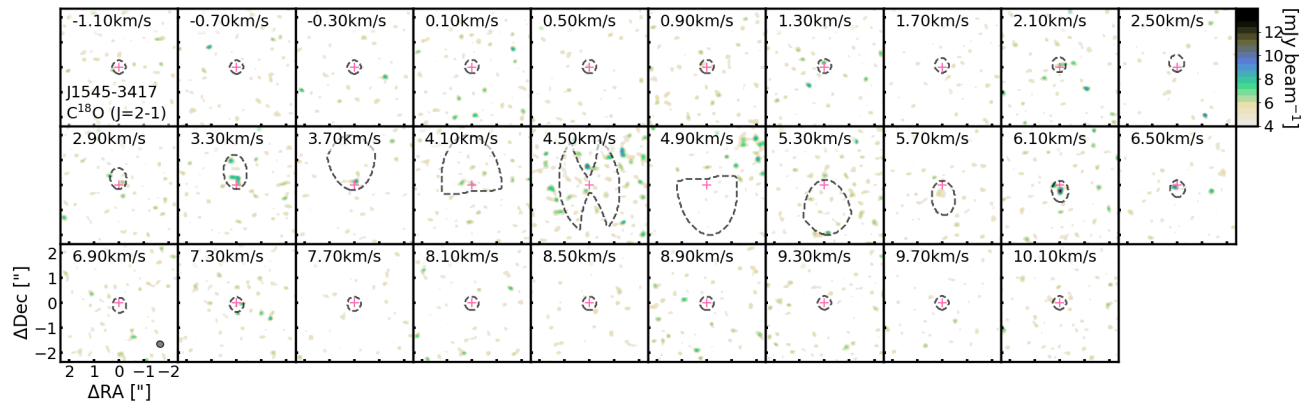


Figure 37. C^{18}O toward J1545-3417 above 2σ .

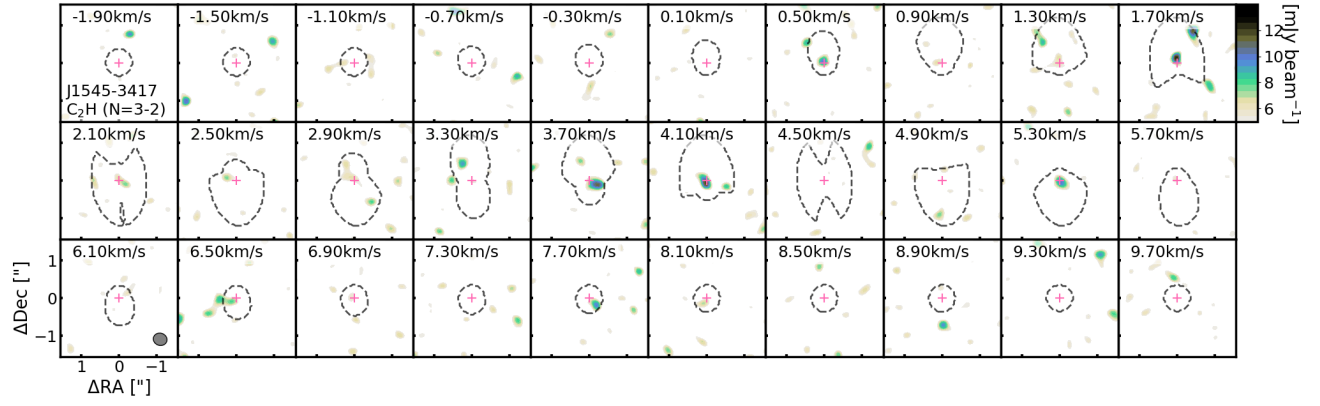


Figure 38. C₂H 3–2 toward J1545-3417 above 2 σ .

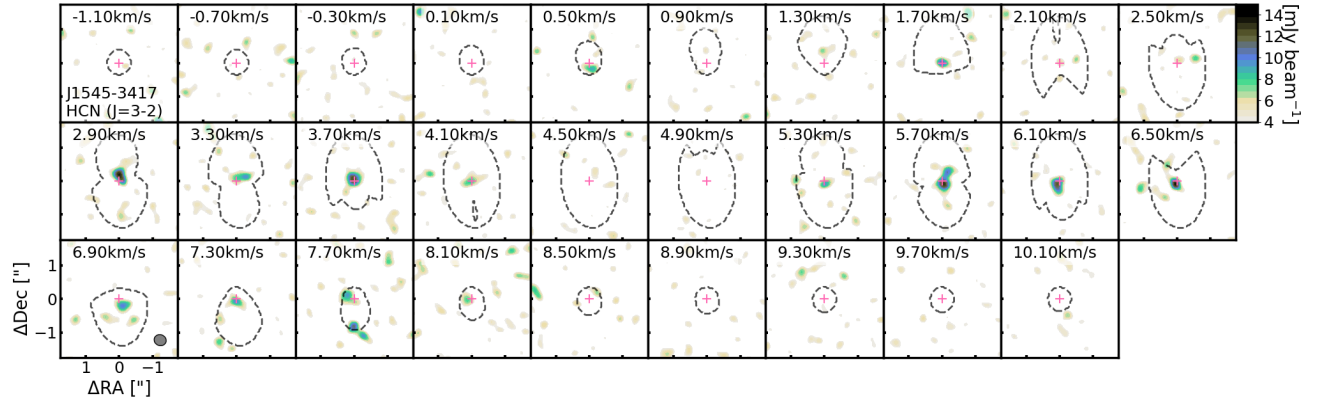


Figure 39. HCN 3–2 toward J1545-3417 above 2 σ .

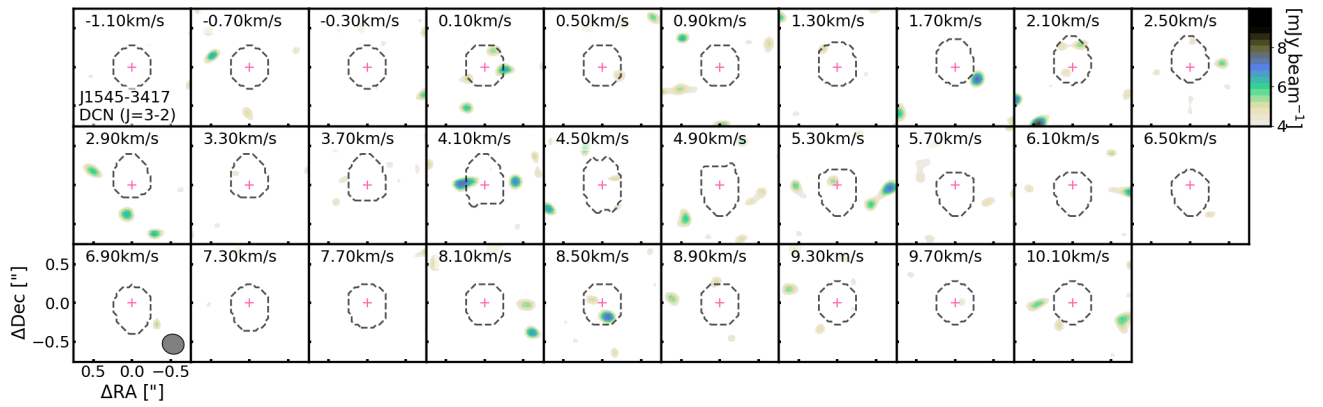


Figure 40. DCN 3–2 toward J1545-3417 above 2 σ .

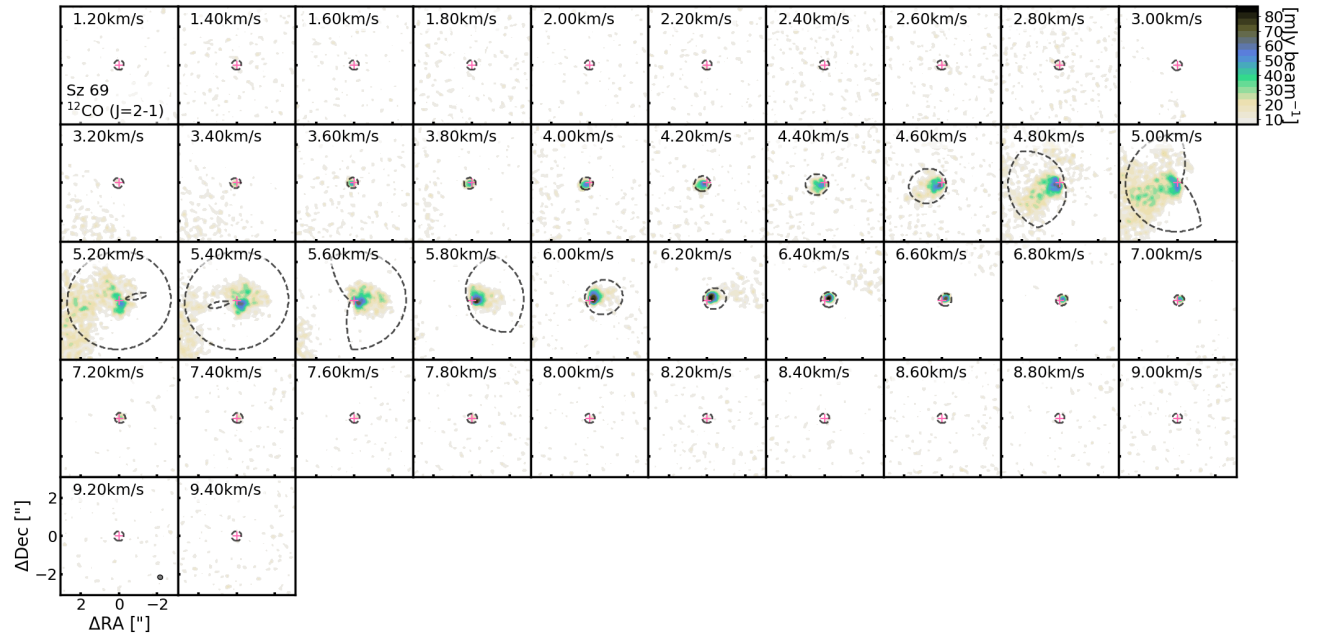


Figure 41. ^{12}CO toward Sz 69 above 2σ .

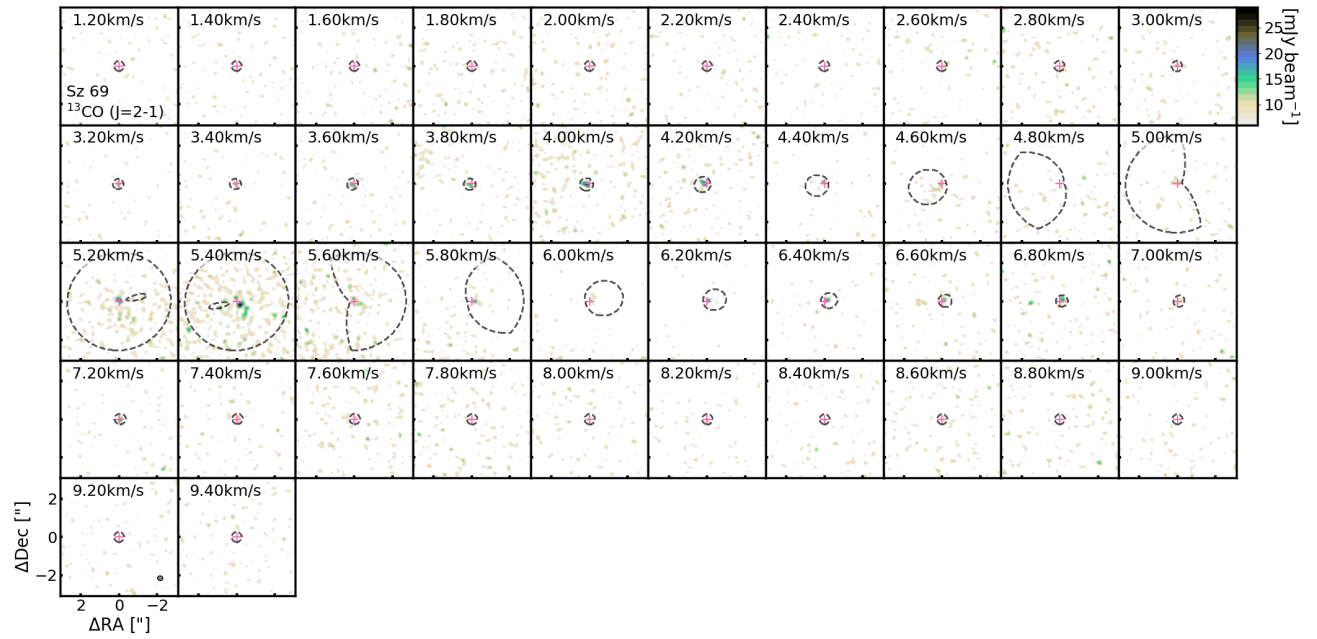


Figure 42. ^{13}CO toward Sz 69 above 2σ .

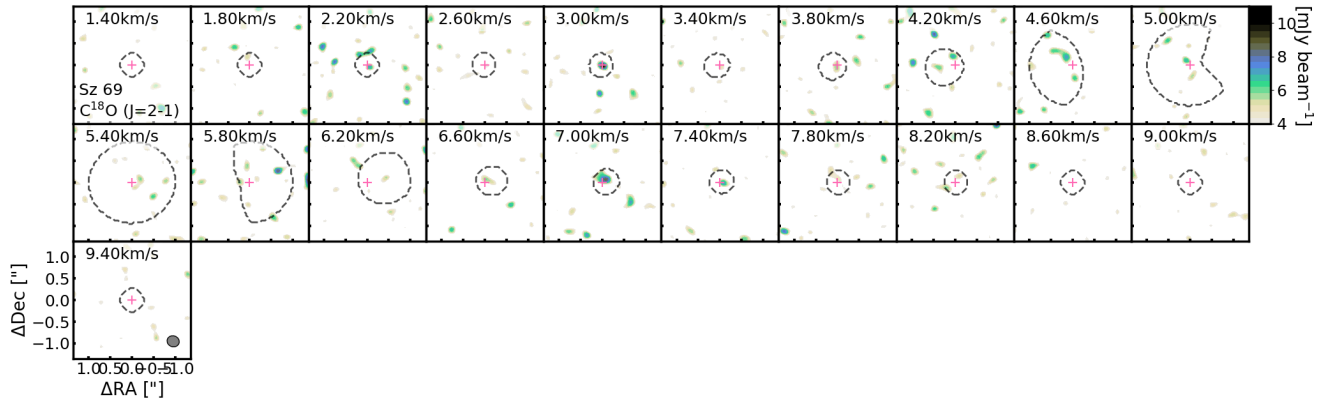


Figure 43. $C^{18}O$ toward Sz 69 above 2σ .

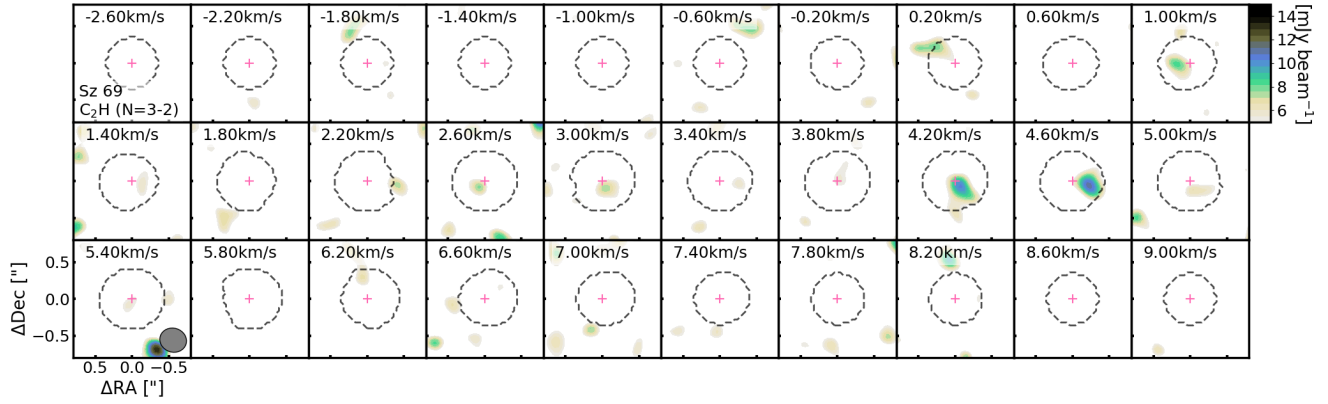


Figure 44. C_2H 3–2 toward Sz 69 above 2σ .

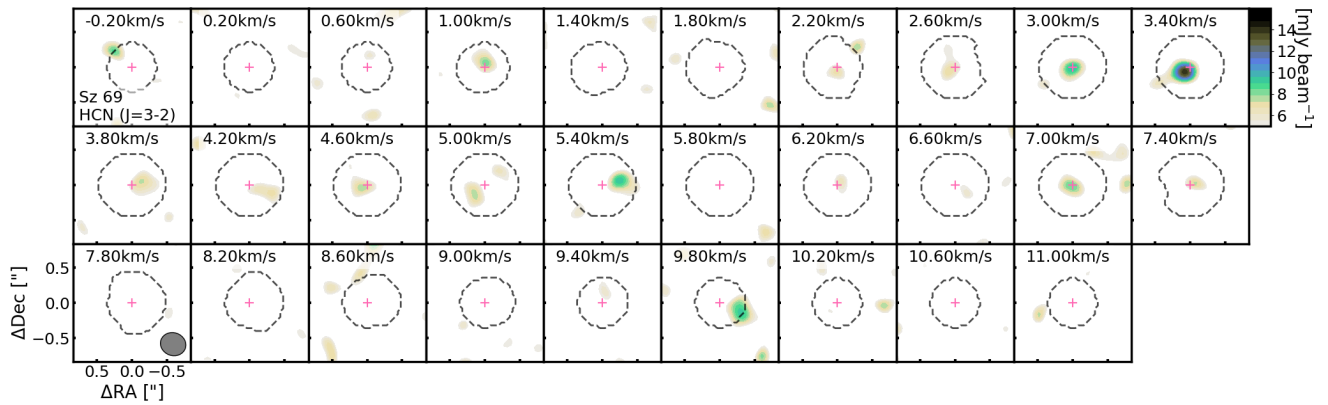


Figure 45. HCN 3–2 toward Sz 69 above 2σ .

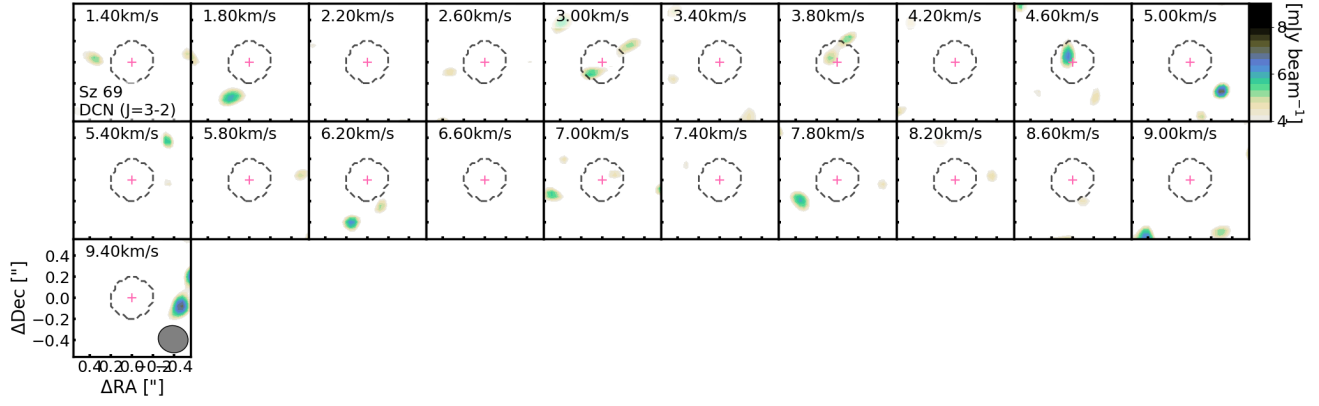


Figure 46. DCN 3–2 toward Sz 69 above 2σ .

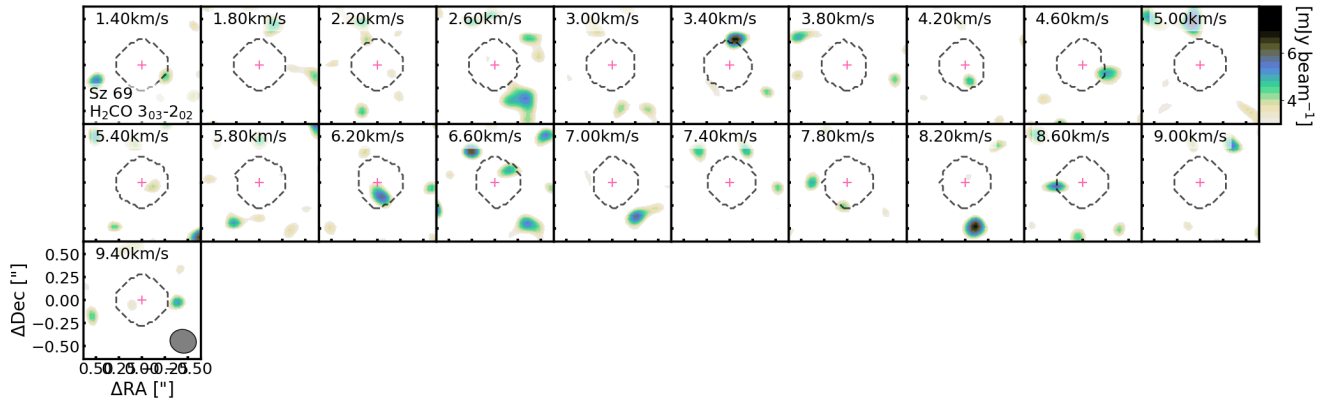


Figure 47. H_2CO 3–2 toward Sz 69 above 2σ .

E. CORRELATION COEFFICIENTS

Table 7 lists the Spearman correlation coefficients (r_{SCC}) and their associated p-values for the log-log flux data presented in Figure 6. The r_{SCC} value is a measure of how well the data can be described by a monotonic function. The corresponding p-value is an estimate of statistical significance; i.e., a lower p-value indicates a lower probability that an uncorrelated system would have a correlation $\geq |r_{\text{SCC}}|$. Pearson correlation coefficients (r_{PCC}) are included in Table 7 for completeness. The r_{PCC} value is a measure of how well the data can be described by a linear function. Note that the r_{PCC} value assumes the underlying datasets are Normally distributed.

Both correlation coefficients range from -1 to 1. Data that is perfectly positively correlated will have an r value of 1, while data that is perfectly negatively correlated will have an r value of -1. Completely uncorrelated data (i.e., pure scatter) will have an r value of 0. p-values range from 0 to 1. Since our datasets are small, we treat r_{SCC} values as significant only if their corresponding p-values are ≤ 0.01 .

F. INVESTIGATION OF OPTICAL DEPTH AS THE PRIMARY CONTRIBUTOR TO FLUX CORRELATIONS

The C_2H and HCN molecular line emission in this survey is still generally optically thick, which means that the emission we observe for these lines does not necessarily trace the underlying molecular abundances. It is possible that the observed emission is instead purely tracing the size of the emission distribution, which would lead to a fixed dependence of emission on the distribution size.

We investigate this possibility here to determine if the correlations in Section 4.3 are solely effects of optically thick emission. We do so by comparing the C_2H 3–2 and HCN 3–2 line fluxes to ^{13}CO 2–1 line fluxes for the M4-M5 disk sample. The ^{13}CO line is also expected to be optically thick. A few ALMA studies have investigated the temperature of CO isotopologue emitting layers for solar-type disks. Schwarz et al. (2016) derived an average ^{13}CO gas temperature of 20–40K across the Tw Hya disk, with values between 20–25K beyond ~ 30 AU. Pinte et al. (2018) found the maximum brightness temperatures for ^{13}CO in IM Lup to be ~ 20 K from 140–300AU. The TW Hya and IM Lup disks both host solar-type stars that are more massive than the host stars in our sample. We expect that these ^{13}CO emitting temperatures for solar-type disks are similar/upper limits to the ^{13}CO emitting temperatures in our own M4-M5 disk sample. We thus assume that the ^{13}CO emitting layer is comparable to the C_2H and HCN emitting layers in the M4-M5 disks.

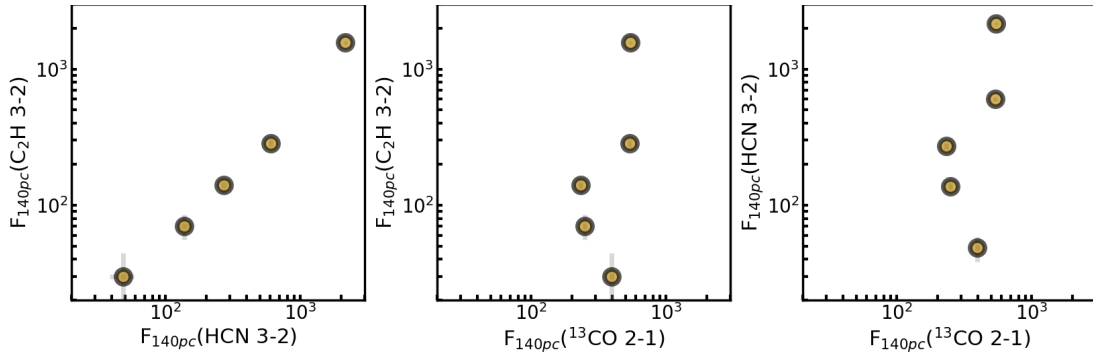
In the case where the C_2H 3–2, HCN 3–2, and ^{13}CO 2–1 lines are uncoupled, we would expect to see the same level of correlation between the three pairs of lines. Figure 48 plots

the total disk fluxes for all three lines against each other. These fluxes are the same fluxes presented in Table 5 and are measured within the bounds of the Keplerian masks (Table 6). We see again the clear correlation between the C_2H 3–2 and HCN 3–2 line fluxes. However, we see that neither C_2H 3–2 nor HCN 3–2 show the same variation with ^{13}CO 2–1. This is evidence against a shared dependence of the relative line fluxes on optical depth. We thus conclude that optically thick emission is not the primary reason for the C_2H 3–2 vs. HCN 3–2 correlation we find in Section 4.3.

Table 7. Correlation Coefficients for the Relative Disk Fluxes of M4-M5, Solar-Type, and Herbig Ae Disks.

| $\ln(F_{140\text{pc}}(x))$ | $\ln(F_{140\text{pc}}(y))$ | M4-M5 Disks | | | | Solar-Type + Herbig Ae Disks | | | | All Disks | | | |
|---------------------------------|------------------------------|-------------|------------------|------------------|----------------------|------------------------------|------------------|------------------|----------------------|-----------|------------------|------------------|----------------------|
| | | # | r_{PCC} | r_{SCC} | p-val _{SCC} | # | r_{PCC} | r_{SCC} | p-val _{SCC} | # | r_{PCC} | r_{SCC} | p-val _{SCC} |
| (1) | (2) | (3) | (4) | (5) | (6) | (7) | (8) | (9) | (10) | (11) | (12) | (13) | (14) |
| $\text{C}^{18}\text{O} (J=2-1)$ | $\text{C}_2\text{H} (N=3-2)$ | 5 | 0.544 | 0.500 | 3.910e-01 | 10 | 0.739 | 0.600 | 6.669e-02 | 15 | 0.818 | 0.814 | 2.194e-04 |
| | $\text{DCN} (J=3-2)$ | 1 | — | — | — | 9 | -0.028 | -0.033 | 9.322e-01 | 10 | 0.339 | 0.248 | 4.888e-01 |
| | $\text{HCN} (J=3-2)$ | 5 | 0.637 | 0.500 | 3.910e-01 | 6 | 0.790 | 0.543 | 2.657e-01 | 11 | 0.822 | 0.882 | 3.302e-04 |
| | H_2CO | 2 | — | — | — | 11 | 0.628 | 0.518 | 1.025e-01 | 13 | 0.756 | 0.687 | 9.509e-03 |
| $\text{HCN} (J=3-2)$ | $\text{C}_2\text{H} (N=3-2)$ | 5 | 0.993 | 1.000 | 1.404e-24 | 7 | 0.803 | 0.750 | 5.218e-02 | 12 | 0.970 | 0.923 | 1.862e-05 |
| | $\text{DCN} (J=3-2)$ | 1 | — | — | — | 7 | 0.508 | 0.571 | 1.802e-01 | 8 | 0.530 | 0.643 | 8.556e-02 |
| | H_2CO | 2 | — | — | — | 7 | 0.940 | 0.857 | 1.370e-02 | 9 | 0.917 | 0.917 | 5.066e-04 |
| $\text{C}_2\text{H} (N=3-2)$ | $\text{DCN} (J=3-2)$ | 1 | — | — | — | 10 | 0.565 | 0.588 | 7.388e-02 | 11 | 0.464 | 0.573 | 6.554e-02 |
| | H_2CO | 2 | — | — | — | 11 | 0.755 | 0.555 | 7.665e-02 | 13 | 0.769 | 0.665 | 1.317e-02 |
| H_2CO | $\text{DCN} (J=3-2)$ | 1 | — | — | — | 10 | 0.405 | 0.394 | 2.600e-01 | 11 | 0.509 | 0.509 | 1.097e-01 |

NOTE—The correlation coefficients describe the relationships between integrated fluxes, scaled to 140pc, for different molecular lines (columns 1 and 2) detected toward M4-M5, solar-type, and Herbig Ae disks, as depicted in Figure 6 and described in Section 4.3. Note that 1e+01 is shorthand for $1 \times 10^{+01}$. All solar-type and Herbig Ae disk data was compiled from the ALMA detections of Huang et al. (2017), Bergner et al. (2019), Bergner et al. (2020), and Pegues et al. (2020). All M4-M5 disk data is from this work. Here we present the Spearman correlation coefficients r_{SCC} and the Pearson correlation coefficients r_{PCC} . We also present the p-values (p-val) for the r_{SCC} values as a measure of statistical significance. Interpretations of the correlation coefficients and the p-values are described in the text of Appendix E.

**Figure 48.** Comparisons of the total $\text{C}_2\text{H} 3-2$ and $\text{HCN} 3-2$ line fluxes to the total $^{13}\text{CO} 2-1$ line fluxes (all scaled to 140pc) for the M4-M5 disk sample.

REFERENCES

- Alcalá, J. M., Manara, C. F., Natta, A., et al. 2017, *A&A*, 600, A20
- Andrews, S. M. 2020, *ARA&A*, 58, 483
- Andrews, S. M., Rosenfeld, K. A., Kraus, A. L., & Wilner, D. J. 2013, *ApJ*, 771, 129
- Andrews, S. M., Terrell, M., Tripathi, A., et al. 2018, *ApJ*, 865, 157
- Andrews, S. M., & Williams, J. P. 2007, *ApJ*, 659, 705
- Ansdell, M., Williams, J. P., Manara, C. F., et al. 2017, *AJ*, 153, 240
- Ansdell, M., Williams, J. P., van der Marel, N., et al. 2016, *ApJ*, 828, 46
- Ansdell, M., Williams, J. P., Trapman, L., et al. 2018, *ApJ*, 859, 21
- Astropy Collaboration, Robitaille, T. P., Tollerud, E. J., et al. 2013, *A&A*, 558, A33
- Astropy Collaboration, Price-Whelan, A. M., Sipőcz, B. M., et al. 2018, *AJ*, 156, 123
- Atkinson, R., Baulch, D. L., Cox, R. A., et al. 2006, *Atmospheric Chemistry and Physics*, 6, 3625.
<https://www.atmos-chem-phys.net/6/3625/2006/>
- Bergin, E. A., Du, F., Cleeves, L. I., et al. 2016, *ApJ*, 831, 101
- Bergner, J. B., Guzmán, V. G., Öberg, K. I., Loomis, R. A., & Pegues, J. 2018, *ApJ*, 857, 69
- Bergner, J. B., Öberg, K. I., Bergin, E. A., et al. 2019, *ApJ*, 876, 25
—, 2020, *ApJ*, 898, 97
- Bulger, J., Patience, J., Ward-Duong, K., et al. 2014, *A&A*, 570, A29
- Carney, M. T., Hogerheijde, M. R., Loomis, R. A., et al. 2017, *A&A*, 605, A21
- Cieza, L., Williams, J., Kourkchi, E., et al. 2015, *MNRAS*, 454, 1909
- Cleeves, L. I., Öberg, K. I., Wilner, D. J., et al. 2018, *ApJ*, 865, 155
- Condon, J. J., & Ransom, S. M. 2016, *Essential Radio Astronomy*
- Dressing, C. D., & Charbonneau, D. 2015, *ApJ*, 807, 45
- Du, F., Bergin, E. A., & Hogerheijde, M. R. 2015, *ApJL*, 807, L32
- Endres, C. P., Schlemmer, S., Schilke, P., Stutzki, J., & Müller, H. S. P. 2016, *Journal of Molecular Spectroscopy*, 327, 95
- Estalella, R. 2017, *PASP*, 129, 025003
- Féraud, G., Bertin, M., Romanzin, C., et al. 2019, *ACS Earth and Space Chemistry*, 3, 1135
- Fockenberg, C., & Preses, J. M. 2002, *The Journal of Physical Chemistry A*, 106, 2924. <http://dx.doi.org/10.1021/jp0141880>
- Foreman-Mackey, D., Hogg, D. W., Lang, D., & Goodman, J. 2013, *PASP*, 125, 306
- Fuchs, G. W., Cuppen, H. M., Ioppolo, S., et al. 2009, *A&A*, 505, 629
- Gaia Collaboration, Prusti, T., de Bruijne, J. H. J., et al. 2016, *A&A*, 595, A1
- Gaia Collaboration, Brown, A. G. A., Vallenari, A., et al. 2018, *A&A*, 616, A1
- Greenwood, A. J., Kamp, I., Waters, L. B. F. M., et al. 2017, *A&A*, 601, A44
- Harvey, P. M., Henning, T., Liu, Y., et al. 2012, *ApJ*, 755, 67
- Hendler, N. P., Mulders, G. D., Pascucci, I., et al. 2017, *ApJ*, 841, 116
- Henry, T. J., Jao, W.-C., Subasavage, J. P., et al. 2006, *AJ*, 132, 2360
- Henry, T. J., Jao, W.-C., Winters, J. G., et al. 2016, in *American Astronomical Society Meeting Abstracts*, Vol. 227, *American Astronomical Society Meeting Abstracts #227*, 142.01
- Hidaka, H., Watanabe, N., Shiraki, T., Nagaoka, A., & Kouchi, A. 2004, *ApJ*, 614, 1124
- Hily-Blant, P., Bonal, L., Faure, A., & Quirico, E. 2013, *Icarus*, 223, 582
- Hiraoka, K., Ohashi, N., Kihara, Y., et al. 1994, *Chemical Physics Letters*, 229, 408. <http://www.sciencedirect.com/science/article/pii/0009261494010668>
- Hiraoka, K., Sato, T., Sato, S., et al. 2002, *ApJ*, 577, 265
- Huang, J., Öberg, K. I., Qi, C., et al. 2017, *ApJ*, 835, 231
- Hunter, J. D. 2007, *Computing In Science & Engineering*, 9, 90
- Jones, E., Oliphant, T., Peterson, P., et al. 2001–, *SciPy: Open source scientific tools for Python*, . <http://www.scipy.org/jpegues>. 2019, *jpegues/kepmask: First release of kepmask, vv1.0.0*, Zenodo, doi:10.5281/zenodo.3382082.
<https://doi.org/10.5281/zenodo.3382082>
- Long, F., Herczeg, G. J., Pascucci, I., et al. 2017, *ApJ*, 844, 99
- Loomis, R. A., Cleeves, L. I., Öberg, K. I., Guzman, V. V., & Andrews, S. M. 2015, *ApJL*, 809, L25
- Luhman, K. L., Allen, P. R., Espaillat, C., Hartmann, L., & Calvet, N. 2010, *ApJS*, 186, 111
- Manara, C. F., Testi, L., Herczeg, G. J., et al. 2017, *A&A*, 604, A127
- Mangum, J. G., & Shirley, Y. L. 2015, *PASP*, 127, 266
- Miotello, A., Facchini, S., van Dishoeck, E. F., et al. 2019, *A&A*, 631, A69
- Mulders, G. D., Pascucci, I., & Apai, D. 2015, *ApJ*, 814, 130
- Öberg, K. I., Murray-Clay, R., & Bergin, E. A. 2011a, *ApJL*, 743, L16
- Öberg, K. I., Qi, C., Fogel, J. K. J., et al. 2010, *ApJ*, 720, 480
—, 2011b, *ApJ*, 734, 98
- Öberg, K. I., Guzmán, V. V., Merchantz, C. J., et al. 2017, *ApJ*, 839, 43
- Oliphant, T. 2006–, *NumPy: A guide to NumPy, USA: Trelgol Publishing*, . <http://www.numpy.org/>
- Pascucci, I., Apai, D., Luhman, K., et al. 2009, *ApJ*, 696, 143
- Pascucci, I., Herczeg, G., Carr, J. S., & Bruderer, S. 2013, *ApJ*, 779, 178
- Pascucci, I., Testi, L., Herczeg, G. J., et al. 2016, *ApJ*, 831, 125

- Pegues, J., Öberg, K. I., Bergner, J. B., et al. 2020, *The Astrophysical Journal*, 890, 142.
<https://doi.org/10.3847/2F1538-4357%2F2Fab64d9>
- Pegues, J., Czekala, I., Andrews, S. M., et al. 2021, *ApJ*, 908, 42
- Pety, J. 2018, in *Submillimetre Single-dish Data Reduction and Array Combination Techniques*, 11
- Pinte, C., Ménard, F., Duchêne, G., et al. 2018, *A&A*, 609, A47
- Pontoppidan, K. M., Salyk, C., Blake, G. A., et al. 2010, *ApJ*, 720, 887
- Reboussin, L., Guilloteau, S., Simon, M., et al. 2015, *A&A*, 578, A31
- Remijan, A., Seifert, N. A., & McGuire, B. A. 2016, in *71st International Symposium on Molecular Spectroscopy*, FB11
- Ricci, L., Testi, L., Natta, A., et al. 2014, *ApJ*, 791, 20
- Rosenfeld, K. A., Andrews, S. M., Hughes, A. M., Wilner, D. J., & Qi, C. 2013, *ApJ*, 774, 16
- Salinas, V. N., Hogerheijde, M. R., Mathews, G. S., et al. 2017, *A&A*, 606, A125
- Schwarz, K. R., Bergin, E. A., Cleeves, L. I., et al. 2016, *ApJ*, 823, 91
- van der Plas, G., Ménard, F., Ward-Duong, K., et al. 2016, *ApJ*, 819, 102
- van Terwisga, S. E., van Dishoeck, E. F., Cazzoletti, P., et al. 2019, *A&A*, 623, A150
- Walsh, C., Millar, T. J., Nomura, H., et al. 2014, *A&A*, 563, A33
- Walsh, C., Nomura, H., & van Dishoeck, E. 2015, *A&A*, 582, A88
- Ward-Duong, K., Patience, J., Bulger, J., et al. 2018, *AJ*, 155, 54
- Watanabe, N., & Kouchi, A. 2002, *ApJL*, 571, L173
- Watanabe, N., Nagaoka, A., Shiraki, T., & Kouchi, A. 2004, *ApJ*, 616, 638
- Yen, H.-W., Koch, P. M., Liu, H. B., et al. 2016, *ApJ*, 832, 204
- Yen, H.-W., Koch, P. M., Manara, C. F., Miotello, A., & Testi, L. 2018, *A&A*, 616, A100